DISSERTATION

NONLINEAR DYNAMICS OF PLANT PIGMENTATION

Submitted by

Wei-Yu Hsu

Department of Mathematics

In partial fulfillment of the requirements

For the Degree of Doctor of Philosophy

Colorado State University

Fort Collins, Colorado

Summer 2022

Doctoral Committee:

Advisor: Patrick Shipman

Jennifer Mueller
Richard Bradley
Richard Finke

ABSTRACT

NONLINEAR DYNAMICS OF PLANT PIGMENTATION

Red, blue, and purple colors in plants are primarily due to plant pigments called anthocyanins. In a plant cell, an equilibrium is established between anionic and cationic forms of anthocyanins as well electrically neutral colorless forms called hemiketals. In typical cellular pH ranges, the colorless hemiketal would be expected to be the dominant form. Why then, do plants, in fact, display colors? We propose that this is part due to self association and intermolecular association of the colored forms of anthocyanins. We develop a series of models for the interconversion of the colorless and colored forms of anthocyanins, including zwitterionic species and extend these models to include association of the colored species. Analysis of these models leads us to suggest and implement experiments in which the total concentration changes over time, either slowly or quickly compared to the kinetics. Coupling these models to a system of partial differential equations for in vivo anthocyanin synthesis (a modification of the Gierer-Meinhardt activator-inhibitor model), we simulate and analyze a variety of colorful spotted patterns in plant flowers. These studies are aided by a linear stability analysis and nonlinear analysis of the modified Gierer-Meinhardt model. The extended model that we propose is a first model to analyze the effects of association in pattern formation. Association may occur with various geometries which have an effect on the absorbance spectrum. Based on the Beer–Lambert law and our evaporative experiments, we develop methods of deconvoluting absorbance spectra of anthocyanin solutions into absorbance spectra of monomers, dimers and trimers, thus providing clues into the geometry of the smallest associated particles. Finally, we propose a novel geometric method of probing association by observing the changing shape of evaporating solution droplets. The associated mathematical model involves solving the highly nonlinear mean-curvature equation with nonconstant mean curvature (surface tension), and we present new solutions making use of the hodograph transform.

ACKNOWLEDGEMENTS

I would like to thank my advisor Dr. Patrick Shipman for continuous support of my study and research, without whom the journey of studying in Colorado State University would be less exhilarating and enjoyable. I also thank Dr. Jennifer Mueller for the numerous courses I took with her and for being on my committee. I would like to thank my committee for their insights and problems on which to work as well as for commenting on the draft of the work. I would like to thank Dr. Stephen Thompson for his patience, enthusiasm, and knowledge that introduced me to a world full of colors. Finally, I would like to thank my family for the unconditional support and love. I would not have succeeded without them. This work was supported by Grant DMS-1814941 awarded by the U.S. National Science Foundation.

DEDICATION

I would like to dedicate this thesis to my family.

TABLE OF CONTENTS

LIST OF FIGURES

Chapter 1

Introduction

The colorful world of the plant kingdom is composed of cell pigments including anthocyanins [1], betacyanins, carotenoids, and cholorophyll. Anthocyanins are responsible for the blue, purple, and red colors in flowers and fruits. The colors and color patterns in flowers have not only ornamental value. Anthocyanins are biologically active chemicals that play diverse and crucial roles in plant cell biology and ecology [2]. They influence pollinators to successfully pollinate and impact the next generations. Anthocyanins and the other pigment compounds such as chlorophyll and carotenoids are photoprotectants [3–5] since they respond for the optical-chemical pathways of energy transduction in plant cells. Anthocyanins also play a role in plant cell defense mechanisms [6].

Anthocyanins contribute to many human uses for plants. They are powerful antioxidants, as well as antihypertensive, antitumor, antidiabetic, and antifungal agents [7–10]. Increasingly, researchers recognize anthocyanins as potential players in the defense against neurological disorders such as Alzheimer's disease by helping to unravel abnormal protein complexes [11]. They influence the taste of red wines [12], and the consumer choice of flowers, fluits, and beverages [13–15]. Therefore, manufacturers of food and beverages have great interest in anthocyanins. Incorporation of anthocyanins into solar cells has increased their sensitivity [16].

If cells are exposed to acids and bases, then anthocyanins change their structures and colors, which means the pH values play a crucial role of presenting different colors. Anthocyanins are stored in plant cell storage compartments called vacuoles. The pH values of vacuoles range from 4 to 6. pH values of 8 or larger are typically necessary for blue forms of anthocyanins. It is no wonder then, that blue roses have eluded horticulturists! In this thesis, we suggest that association is a key to understanding how there can there be any blue flowers.

The chemical structure of anthocyanins can help us to study the variation in color. The flavylium cation is the parent structure for an anthocyanin molecule, and its three rings form a chromophore,

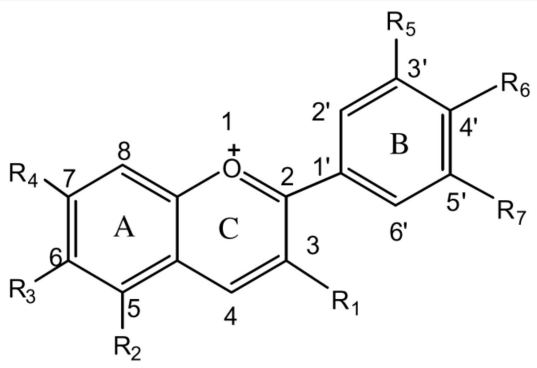

Figure 1.1: The flavylium cation.

which is responsible for its color; see Figure 1.1. There are 20 known types of anthocyanidin molecule, such as malvidin and pelargonidin, whose structures are shown in Figure 1.2. The types of anthocyanidin are distinguished by the choices of $-H$, $-OH$, or $-OH_3$ groups at the positions R_i. Although anthocyanidins are insoluble in water, anthocyanins are water-soluble. At the positions marked $1-8$ and $1'-6'$, there can be the addition sugars (glycosyl units) that turn an anthocyanidin into one of the more than 900 known types of anthocyanin. By adding acyl units to the sugars, there may be further modifications of anthocyanins. Because these additions and modifications denote electrons to the chromophore and change the geometry of the molecule, they influence the anthocyanin color.

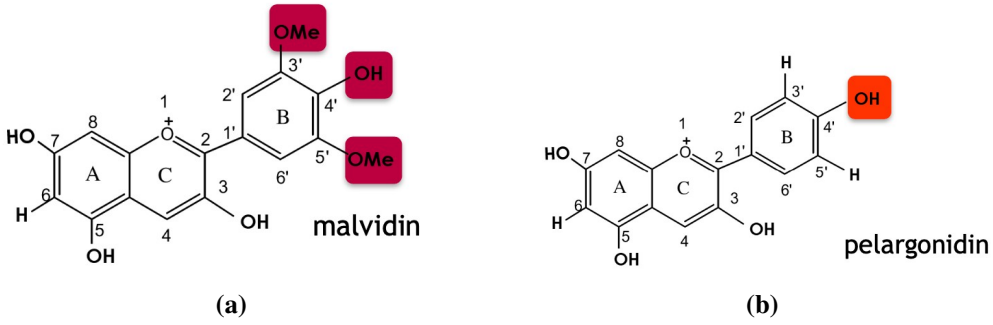

(a) **(b)**

Figure 1.2: Two well-known anthocyanidins, (a) malvidin, and (b) pelargonin

For any given anthocyanin, we are interested in the string of fast and slow reactions between what we will call species; see Figure 1.3. Fast acid-base reactions transform the blue anion A^-

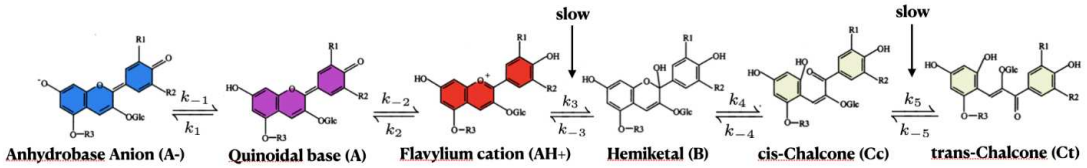

Figure 1.3: pH-dependent anthocyanins structural changes. These species are the majority monomer that we will discuss in the following Chapters. Denote the blue anion by A^-, the purple quinoidal base by A, the red flavylium cation by AH^+, the colorless hemiketal by B, the light yellow cis-chalcone by C, and the light yellow-green trans-chalcone C^-.

into the purple quinoidal base A and turn A into the red flavylium cation AH^+. Slow hydration of the red flavylium cation AH^+ forms the colorless hemiketal B. From B, tautomerization produces the light yellow cis-chalcone C_{cis}. Slow isomerization changes C_{cis} into the light yellow-green trans-chalcone C_{trans}.

These reversible reactions are pH dependent. Thus, different species will dominate at different pH values. The lower pH values move the reactions to the right in the scheme of Figure 1.3. We will discuss the dominant species thoroughly in Chapter 2.

The structures shown in Figure 1.2 and Figure 1.3 are single anthocyanin molecules, which are called monomers. Previous studies have shown that anthocyanins undergo both intramolecular associations (association with each other to form dimers, trimers, and larger j-mers) [17–20] and intermolecular associations (association with other molecules) [21–23]. The microscopic im-

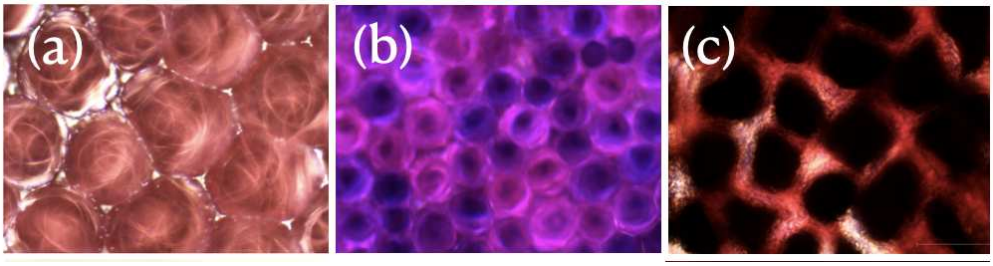

Figure 1.4: Optical microscope images of pigmented plant cells and anthocyanin complexes. (a) Anthocyanins associated with microtubules in geranium cells. (b,c) Various phases of anthocyanin complexes are present in these cells of (b) purple petunia and (c) blueberry. Samples were prepared and imaged by Dr. Stephen Thompson.

ages of cells in the outmost layer of flower petals (the epidermis) in Figure 1.4 (a- c) reveal that

anthocyanins are not merely present in solution in plant cells, but associate to form complexes with other molecules (microtubules dyed red by association with anthocyanins in panel (a)) or with themselves to form particles (panels (b,c)). These images were produced by Dr. Stephen Thompson, our collaborator in the study of anthocyanins.

Anthocyanin intramolecular association occurs through several types of chemical bonding. The hydrophobic chromophore, composed of what we call A, B, or C rings, has delocalized electrons which are involved in $H-H$ bonding and they will form H associates. These delocalized electrons form what are called $\pi - \pi$ dispersion forces to operate in stacking modes. The other associates are called J associates. They come from electrostatic hydrogen bonding (primarily -OH groups in the B ring and glycosides) and produce end-to-end and offset associates. See Figure 1.5 [24]. The important factors in the association of different anthocyanin species are bonding types, strength, and geometry. For instance, A is a neutral quinoid with reduced solubility, so it reduced ability to associate. A^- has negative charge and willing to ion-pair with cations. Furthermore, A^{2-} has enhanced solubility, and therefore enhanced ability to associate. It is also known that A can associate with AH^+. For a detailed discussion of these association scheme, see Section 2.4. AH^+ has a positive charge and will ion-pair with negatively charged ions, which are so-called anions. The addition of anions to AH^+ will form zwitterionic molecules $(AH^+)^-$, which have negative and positive parts that allow for alternating stacking. We will discuss a reaction scheme including zwitterionic species in Section 2.2. Phase transitions occur in the vacuolar environment are impacted by concentrations, solubility factors, the hydrophobic/hydrophilic balance, and B-ring substitution. Therefore, the vacuole influences anthocyanin function.

Many flowers exhibit patterns of color, which are comprised of a variation in anthocyanin concentration. A wide variety of patterns is observed in nature [25, 26]. Pigmentation patterns on flower petals provide visual cues in the insect pollination and reproduction [27–30]. Recent work in monkeyflowers, see [31], characterizes an R2R3-MYB activator, which activates its own production as well as that of a repressor molecule, and an R3-MYB repressor, which inhibits activator production and diffuses to nearby cells more quickly than the activator. We use the

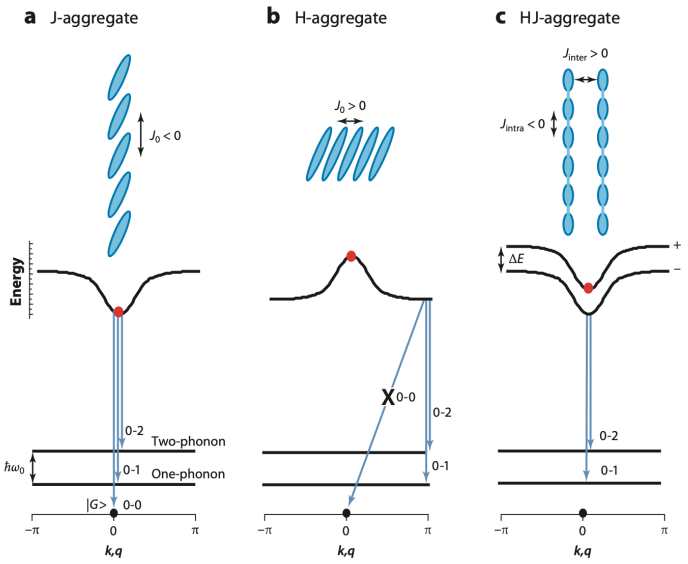

Figure 1.5: Schematic diagrams of $J-$ and $H-$aggregates together with energy profiles. This images is taken from Ref. [24]. The sign of the nearest-neighbor coupling J_0 is determined by the through-space Coulombic coupling. (a)Head-to-tail orientations lead to $J_0 < 0$ and $J-$association. (b)Side-by-side orientations led to $J_0 > 0$ and $H-$association. (c)In polymer $HJ-$associates, Coulombic interchain coupling is positive ($J_{inter} > 0$), whereas the effective intrachain coupling between adjacent repeat units is negative ($J_{intra} < 0$) owing to through-bond interactions in 1D direct band-gap semiconductors.

corresponding activator-inhibitor mathematical model, and the sigmoidal biological transcriptional behavior of production of monomer to simulate patterns in Section 2.6.

The most important concept of this dissertation is that of anthocyanin association, including intermolecular association and self association. These associations influence the colors and patterns in flowers, which impacts interactions with pollinators as well as energy transduction pathways in cells. Chapter 2 of this dissertation presents models for anthocyanin association and pattern formation.

Absorbance spectra of anthocyanin solutions measure the amount of light absorbed as a function of wavelength. the absorbance spectrum of an anthocyanin solution is a combination of the individual absorbance spectra of the anthocyanin monomer, dimer, trimer, and larger Nmers. We are interested in deconvoluting the absorbance spectrum of an anthocyanin solution to determine the absorptivity of monomers, dimers, and trimers since the shift of peak of the absorptivity helps us to understand the geometry of association. A model of anthocyanin self association given in

Chapter 2 informs a new method of deconvolution that we present in Chapter 4. This model predicts that, at low total anthocyanin concentrations in solution, anthocyanins will exist primarily as monomers, dimers, and trimers and predicts the relative concentrations of these Nmers. In order to determine the absorptivities of monomers, dimers, and trimers, we combine experimental data that gives the absorbance spectra at a range of low concentrations with our model. We show that, for this method to work despite noise in the experimental data and the competition with larger Nmers at higher concentrations, we need a sufficient number of experimental measurements of absorbance spectra at very low concentrations (on the order of 10^{-5} M). Accurately measuring concentrations that are this low is difficult experimentally. This leads us to propose an approach to measuring low concentrations by measuring the contact angle of droplets of anthocyanin solution with a surface, as this contact angle depends on anthocyanin concentration. The reason that the contact angle depends on anthocyanin concentration is that anthocyanins act as surfactants that change the surface tension of the liquid droplet. Also, the surface tension is proportional to the mean curvature. Hence, understanding the geometry of the droplet helps us to figure out the concentration of the solution. This could be a way to approach measurement of low concentrations. Although we do not fully realize this method for measuring low concentrations in this dissertation, in Chapter 3 we make progress towards this approach by proposing a method to solving the mean-curvature equation.

This dissertation report is organized as follows: Chapter 2 introduces a series of models for anthocyanin reaction schemes, association, and spatial pattern formation. Starting with an analysis of the steady-state as a function of pH in a 'basic scheme' introduced in Section 2.1, we extend this analysis to include intermolecular association in Section 2.3 and self association in Section 2.4. In Section 2.2, we include a zwitterionic species in the scheme. Section 2.5 concerns the dynamics of the concentrations of anthocyanin species as the total concentration of the solution changes in *evaporative experiments*. Section 2.6 concerns spatial patterns of anthocyanins. We perform linear stability analysis of a modified Gierer-Meinhardt model which has been proposed to model an activator-inhibitor system involved in anthocyanin production. Our numerical simulations close

to a Turing bifurcation threshold determined by the linear stability analysis show well-ordered patterns of rolls, squares, and hexagons. Nonlinear analysis of the modified Gierer-Meinhardt model close to this bifurcation threshold results in differential equations for amplitudes of finite numbers of Fourier modes involved in these patterns and allows for a study of the competition between patterns of rolls and up- and down-hexagons. In this section, we also extend the Gierer-Meinhardt model to allow the activator to activate anthocyanin production to include anthocyanin synthesis as well as self association.

Chapter 3 introduces a novel geometric method to probe anthocyanin association. We motivate a study of the mean-curvature equation by describing how anthocyanins in solution modify the surface tension of a liquid droplet. This section includes a new mathematical approach, using the hodograph transform, to solving the mean curvature equation. We apply this approach to find conformal parameterizations of surfaces of revolution with mean curvature that is a function of radius alone. Section 3 introduces a novel geometric method to probe anthocyanin association. This approach is suggested by an analysis of the Cross-Newell phase-diffusion equation by N. Ercolani, R. Indik, A. C. Newell, T. Passot [32].

Chapter 4 concerns methods of deconvoluting absorbance spectra of anthocyanin solutions. Prof. Thompson has collected thousands of absorbance spectra of anthocyanins in solution. These solutions are at varying concentrations and pH values. Therefore, they are mixtures of various anthocyanin species and contain anthocyanin monomers, dimers, trimers, and larger aggregates. The goal is to deconvolute the spectra into the absorbance spectra of the various species and $n$mers. Our unique approach to deconvolution utilizes data sets collected at various concentrations, and combines the models presented in Chapter 2 with a Bayesian statistical methods to give probability distributions for the absorbance spectra. The Beer–Lambert law states the absorbance expression is $Abs = \ell \sum_j s_j c_j$, where ℓ is the optical path length in cm, s_j are absorptivity of different species, and c_j are the concentrations of different species. Applying the Bayesian method, we can find a probability density $\sigma(\mathbf{m} \mid \mathbf{d})$ that describes the probability of the vector $\mathbf{m}$ of parameter values such as absorptivity s_j given the data $\mathbf{d}$, which are experimental absorbance spectra.

Chapter 2

Anthocyanin reaction schemes, association, and spatial patterns

Studying anthocyanins is an important project not only in bio-chemical researches, but also in the industrial application area. Anthocyanins are so intriguing because they will affect the ornamental value of flowers, provide visual cues to pollinators and seed distributors, and then promote pollination success, and an anthocyanin is also a source of non-toxic food dyes. In previous work, Sadlowski [19] formed the chemical reactions including anhydrobase anion $(A-)$, flavylium cation (AH^+), quinoidal anhydrobase (A), and carbinol pseudobase (B). Based on these reactions, we obtain the concentrations of different structural transformations in several situations.

In this chapter, we develop a series of models for anthocyanin reaction schemes, association, and spatial pattern formation. We start with an analysis of the steady-state as a function of pH in a 'basic scheme' introduced in Section 2.1. We extend this analysis to include intermolecular association in Section 2.3 and self association in Section 2.4. In Section 2.2, we include a zwitterionic species in the scheme. Section 2.5 concerns the dynamics of the concentrations of anthocyanin species as the total concentration of the solution changes in *evaporative experiments*. Section 2.6 concerns spatial patterns of anthocyanins. We first perform a linear stability analysis and nonlinear analysis of an activator-inhibitor system recently introduced by Ding and colleagues [31] that models diffusion synthesis, and degradation of an activator for anthocyanin production and a molecule that inhibits the synthesis of the activator. These analyses combined with numerical simulations lead us to predictions on parameter values that produce more well-ordered patterns than those found by Ding and colleagues and allow us to predict parameter values for the formation of stripe, hexagon, and square patterns. We extend the model of Ding and colleagues to include anthocyanin synthesis as well as self association. We propose that the activator also activates the anthocyanin in the cytoplasm production through the sigmoidal relationship.

2.1 The basic monomer reaction scheme

We start with the basic scheme including the species A^- (the blue anion), A (the purple quinoidal base), AH^+ (the red flavylium cation), B (the colorless hemiketal), C (the light yellow cis-chalcone), and C^- (the light yellow-green trans-chalcone), and without association. The chemical reaction scheme is the following:

$$\begin{aligned} A^- + H^+ &\underset{k_1}{\overset{k_{-1}}{\rightleftharpoons}} A \\ A + H^+ &\underset{k_2}{\overset{k_{-2}}{\rightleftharpoons}} AH^+, \qquad B \underset{k_{-6}}{\overset{k_6}{\rightleftharpoons}} B^- + H^+ \\ AH^+ &\underset{k_{-3}}{\overset{k_3}{\rightleftharpoons}} B + H^+ \\ B &\underset{k_{-4}}{\overset{k_4}{\rightleftharpoons}} C \underset{k_{-5}}{\overset{k_5}{\rightleftharpoons}} C^- + H^+ \end{aligned} \tag{2.1}$$

The law of mass action transforms their kinetic equations into the following system of ordinary differential equations:

$$\frac{d}{dt}[A^-] = \{-k_{-1}[A^-][H^+] + k_1[A]\} \tag{2.2}$$

$$\frac{d}{dt}[A] = -\{-k_{-1}[A^-][H^+] + k_1[A]\} + \{-k_{-2}[A][H^+] + k_2[AH^+]\} \tag{2.3}$$

$$\frac{d}{dt}[AH^+] = -\{-k_{-2}[A][H^+] + k_2[AH^+]\} + \{-k_3[AH^+] + k_{-3}[B][H^+]\} \tag{2.4}$$

$$\frac{d}{dt}[B] = -\{-k_3[AH^+] + k_{-3}[B][H^+]\} + \{-k_4[B] + k_{-4}[C]\} + \{-k_6[B] + k_{-6}[B^-][H^+]\} \tag{2.5}$$

$$\frac{d}{dt}[B^-] = -\{-k_6[B] + k_{-6}[B^-][H^+]\} \tag{2.6}$$

$$\frac{d}{dt}[C] = -\{-k_4[B] + k_{-4}[C]\} + \{-k_5[C] + k_{-5}[C^-][H^+]\} \tag{2.7}$$

$$\frac{d}{dt}[C^-] = -\{-k_5[C] + k_{-5}[C^-][H^+]\} \tag{2.8}$$

The equilibrium constants for the anthocyanin malvidin $3-$glucuronide, found in references [19] and [33], are

$$K_1 = \frac{k_1}{k_{-1}} = 10^{-6.37}, \;\; K_2 = \frac{k_2}{k_{-2}} = 10^{-4}, \;\; K_3 = \frac{k_3}{k_{-3}} = 10^{-1.92}, \tag{2.9}$$

$$K_4 = \frac{k_4}{k_{-4}} = 10^{-0.98}, \;\; K_5 = \frac{k_5}{k_{-5}} = 10^{-6.75}, \;\; K_6 = \frac{k_6}{k_{-6}} = 10^{-7.86}. \tag{2.10}$$

These are the equilibrium constants, not the reaction constants.

To find the steady-state concentrations, we set all time derivatives to zero ($\frac{d}{dt}[\bullet] = 0$) and represent all the concentrations in terms of $[A]$:

$$[A^-] = \frac{K_1}{[H^+]} \times [A] \tag{2.11}$$

$$[A] = [A] \tag{2.12}$$

$$[AH^+] = \frac{[H^+]}{K_2} \times [A] \tag{2.13}$$

$$[B] = \frac{K_3}{K_2} \times [A] \tag{2.14}$$

$$[B^-] = \frac{K_6 \times K_3}{[H^+] \times K_2} \times [A] \tag{2.15}$$

$$[C] = \frac{K_4 \times K_3}{K2} \times [A] \tag{2.16}$$

$$[C^-] = \frac{K_5 \times K_4 \times K_3}{K_2 \times [H^+]} \times [A] \tag{2.17}$$

The total anthocyanin concentration is a conserved quality for the system Eq. 2.2- Eq. 2.8.

$$[T] = [A^-] + [A] + [AH^+] + [B] + [B^-] + [C] + [C^-]. \tag{2.18}$$

In terms of the equilibrium solutions Eq. 2.11 - Eq. 2.17, $[T] = K_T([H^+])[A]$, where

$$K_T([H^+]) = (\frac{K_1}{[H^+]} + 1 + \frac{[H^+]}{K_2} + \frac{K_3}{K_2} + \frac{K_6 \times K_3}{[H^+] \times K_2} + \frac{K_4 \times K_3}{K2} + \frac{K_5 \times K_4 \times K_3}{K_2 \times [H^+]})$$

The equilibrium solutions Eq. 2.11 - Eq. 2.17 can therefore be written as substitution

$$[A] = \frac{[T]}{K_T([H^+])}$$

into those equations. The resulting equilibrium solutions as functions of pH$= -\log_{10}[H^+]$ are shown in Figure 2.1.

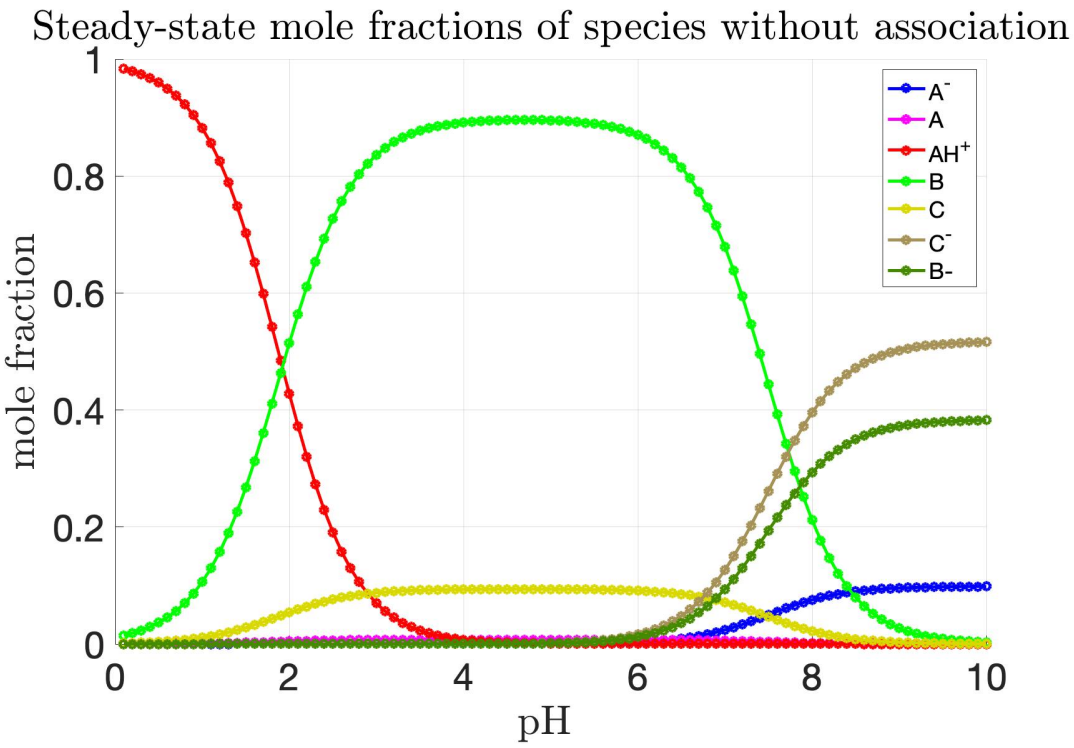

Figure 2.1: Steady-state mole fractions of species without association.

The results demonstate that the basic monomer scheme implies the colorless hemiketal B dominates in the pH range 3-6, which includes the pH range of typical plant vacuoles. This means

there should not be color in flowers. How can the colored anthocyanin species be observed in plant cells? In the following subsections, we will propose several possible answers to this question.

2.2 Zwitterions and a square scheme

One possible reason for the existence of colored species is that there are zwitterions. A *zwitterion* is a molecule which has a functional group with a positive charge as well as a functional group having a negative charge, with an overall charge of zero. Since AH^+ has a positive charge and will ion-pair with negatively charged ions, AH^+ will form zwitterionic molecules $(AH^+)^-$ by adding a negative charge. Hence, we will add a diagonal line ($\mathrm{A} \underset{\mathrm{m_-}}{\overset{\mathrm{m_+}}{\rightleftharpoons}} ((\mathrm{AH}^+))^-$) to our scheme.

A diagram for this scheme is as follows:

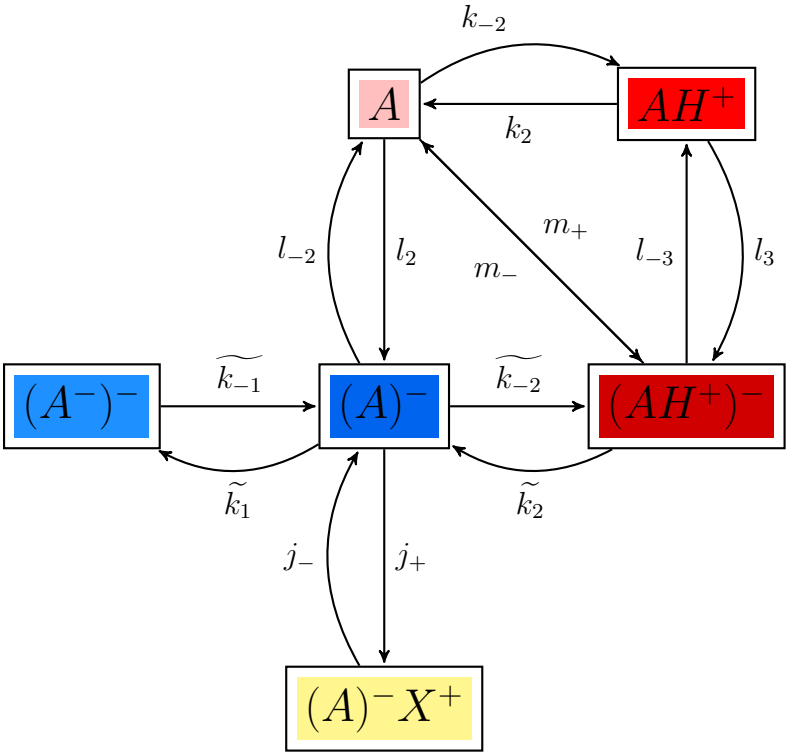

Figure 2.2: Square scheme

The following is the full schemes, and we also make some informal guess of the equilibrium constants because those numbers are unknown.

$$\begin{aligned}
\mathrm{A} + \mathrm{H}^+ \underset{\mathrm{k}_2}{\overset{\mathrm{k}_{-2}}{\rightleftharpoons}} \mathrm{AH}^+, &\qquad K_2 = \frac{k_2}{k_{-2}} = 10^{-4},\\
\mathrm{A} \underset{\mathrm{l}_{-2}}{\overset{\mathrm{l}_2}{\rightleftharpoons}} (\mathrm{A})^- + \mathrm{H}^+, &\qquad L_2 = \frac{l_2}{l_{-2}} = 10^{-3.25},\\
\mathrm{AH}^+ \underset{\mathrm{l}_{-3}}{\overset{\mathrm{l}_3}{\rightleftharpoons}} (\mathrm{AH}^+)^- + \mathrm{H}^+, &\qquad L_3 = \frac{l_3}{l_{-3}} = 10^{-3.25},\\
((\mathrm{A})^-)^- + \mathrm{H}^+ \underset{\widetilde{\mathrm{k}_1}}{\overset{\widetilde{\mathrm{k}_{-1}}}{\rightleftharpoons}} (\mathrm{A})^-, &\qquad \widetilde{K_1} = \frac{\widetilde{k_1}}{\widetilde{k_{-1}}} = 10^{-6.37},\ \text{(guess)}\\
(\mathrm{A})^- + \mathrm{H}^+ \underset{\widetilde{\mathrm{k}_2}}{\overset{\widetilde{\mathrm{k}_{-2}}}{\rightleftharpoons}} ((\mathrm{AH}^+))^-, &\qquad \widetilde{K_2} = \frac{\widetilde{k_2}}{\widetilde{k_{-2}}} = 10^{-4},\ \text{(guess)}\\
\mathrm{A} \underset{\mathrm{m}_-}{\overset{\mathrm{m}_+}{\rightleftharpoons}} ((\mathrm{AH}^+))^-, &\qquad M_3 = \frac{m_+}{m_-} = 10^{-4},\ \text{(guess)}\\
(\mathrm{A})^- + \mathrm{X} \underset{\mathrm{j}_-}{\overset{\mathrm{j}_+}{\rightleftharpoons}} (\mathrm{A})^-\mathrm{X}^+, &\qquad J = \frac{j_+}{j_-}
\end{aligned}$$

From these schemes, we can write the rates of change of the concentrations as below.

$$\begin{aligned}
\frac{d}{dt}[A] =& - k_{-2}[A][H^+] + k_2[AH^+] - l_2[A] + l_{-2}[(A)^-][H^+]\\
&- m_+[A] + m_+[(AH^+)^-]\\
\frac{d}{dt}[AH^+] =& k_{-2}[A][H^+] - k_2[AH^+] - l_3[AH^+] + l_{-3}[(AH^+)^-][H^+]\\
\frac{d}{dt}[(A)^-] =& l_2[A] - l_{-2}[(A)^-][H^+] - \widetilde{k_{-2}}[(A)^-][H^+] + \widetilde{k_2}[(AH^+)^-]\\
&- j_+[(A)^-][X] + j_-[(A)^-X^+] + \widetilde{k_{-1}}[(A^-)^-][H^+] - \widetilde{k_1}[(A)^-]\\
\frac{d}{dt}[(AH^+)^-] =& l_3[AH^+] - l_{-3}[(AH^+)^-][H^+] + \widetilde{k_{-2}}[(A)^-][H^+] - \widetilde{k_2}[(AH^+)^-]\\
&+ m_+[A] - m_+[(AH^+)^-]\\
\frac{d}{dt}[(A^-)^-] =& - \widetilde{k_{-1}}[(A^-)^-][H^+] + \widetilde{k_1}[(A)^-]\\
\frac{d}{dt}[(A)^-X^+] =& j_+[(A)^-][X] - j_-[(A)^-X^+].
\end{aligned}$$

Because all the concentrations can be represented in terms of $[A]$, $[AH^+]$, $[(AH^+)^-]$, the steady-state concentrations can be solved by finding their null space. Therefore, the concentrations for $[A]$, $[AH^+]$, $[(AH^+)^-]$, and $[(A)^-]$ are represented as

$$\begin{bmatrix} [A] \\ [AH^+] \\ [(AH^+)^-] \\ [(A)^-] \end{bmatrix} = \mu(k_{-2}[H^+])(l_{-2}[H^+])(l_{-3}[H^+]) \left(\begin{bmatrix} \frac{K_2}{[H^+]} + \frac{K_2}{[H^+]}\frac{\widetilde{k_{-2}}}{l_{-2}} + \frac{K_2}{[H^+]}\frac{\widetilde{k_2}}{l_{-3}[H^+]} + \frac{L_3}{[H^+]}\frac{\widetilde{K_2}}{[H^+]}\frac{\widetilde{k_{-2}}}{k_{-2}} \\ 1 + \frac{\widetilde{k_{-2}}}{l_{-2}} + \frac{\widetilde{k_2}}{l_{-3}[H^+]} + \frac{L_2}{[H^+]}\frac{\widetilde{k_{-2}}}{k_{-2}} \\ \frac{L_3}{[H^+]} + \frac{L_3}{[H^+]}\frac{\widetilde{k_{-2}}}{l_{-2}} + \frac{L_2}{[H^+]}\frac{K_2}{[H^+]}\frac{[H^+]}{\widetilde{K_2}}\frac{\widetilde{k_2}}{l_{-3}[H^+]} + \frac{L_2}{[H^+]}\frac{L_3}{[H^+]}\frac{\widetilde{k_{-2}}}{k_{-2}} \\ \frac{L_3}{[H^+]}\frac{\widetilde{K_2}}{[H^+]}\frac{\widetilde{k_{-2}}}{l_{-2}} + \frac{K_2}{[H^+]}\frac{L_2}{[H^+]} + \frac{L_2}{[H^+]}\frac{K_2}{[H^+]}\frac{\widetilde{k_2}}{l_{-3}[H^+]} + \frac{L_2}{[H^+]}\frac{L_3}{[H^+]}\frac{\widetilde{K_2}}{[H^+]}\frac{\widetilde{k_{-2}}}{k_{-2}} \end{bmatrix} \right. \tag{2.19}$$

$$\left. + \frac{m_-}{l_{-3}[H^+]} \begin{bmatrix} \frac{K_2}{[H^+]} + \frac{K_2}{[H^+]}\frac{\widetilde{k_{-2}}}{l_{-2}} + \frac{L_3}{[H^+]}\frac{\widetilde{K_2}}{[H^+]}\frac{\frac{\widetilde{k_{-2}}}{k_{-2}}}{\frac{\widetilde{k_2}}{l_{-3}[H^+]}} + \frac{L_3}{[H^+]}\frac{\widetilde{K_2}}{[H^+]}\frac{\frac{\widetilde{k_{-2}}}{k_{-2}}}{\frac{\widetilde{k_2}}{l_{-3}[H^+]}}\frac{\widetilde{k_{-2}}}{l_{-2}} \\ 1 + \frac{\widetilde{k_{-2}}}{l_{-2}} + M_3\frac{\widetilde{K_2}}{[H^+]}\frac{\frac{\widetilde{k_{-2}}}{k_{-2}}}{\frac{\widetilde{k_2}}{l_{-3}[H^+]}} + M_3\frac{\widetilde{K_2}}{[H^+]}\frac{\frac{\widetilde{k_{-2}}}{k_{-2}}}{\frac{\widetilde{k_2}}{l_{-3}[H^+]}}\frac{\widetilde{k_{-2}}}{l_{-2}} \\ \frac{K_2}{[H^+]}M_3 + \frac{K_2}{[H^+]}M_3\frac{\widetilde{k_{-2}}}{l_{-2}} + M_3\frac{L_3}{[H^+]}\frac{\widetilde{K_2}}{[H^+]}\frac{\frac{\widetilde{k_{-2}}}{k_{-2}}}{\frac{\widetilde{k_2}}{l_{-3}[H^+]}} + M_3\frac{L_3}{[H^+]}\frac{\widetilde{K_2}}{[H^+]}\frac{\frac{\widetilde{k_{-2}}}{k_{-2}}}{\frac{\widetilde{k_2}}{l_{-3}[H^+]}}\frac{\widetilde{k_{-2}}}{l_{-2}} \\ \frac{K_2}{[H^+]}M_3\frac{\widetilde{K_2}}{[H^+]}\frac{\widetilde{k_{-2}}}{l_{-2}} + \frac{L_2}{[H^+]}\frac{K_2}{[H^+]} + M_3\frac{L_3}{[H^+]}\frac{\widetilde{K_2}}{[H^+]}\frac{\frac{\widetilde{k_{-2}}}{k_{-2}}}{\frac{\widetilde{k_2}}{l_{-3}[H^+]}}\frac{\widetilde{K_2}}{[H^+]}\frac{\widetilde{k_{-2}}}{l_{-2}} + \frac{L_2}{[H^+]}\frac{L_3}{[H^+]}\frac{\widetilde{K_2}}{[H^+]}\frac{\frac{\widetilde{k_{-2}}}{k_{-2}}}{\frac{\widetilde{k_2}}{l_{-3}[H^+]}} \end{bmatrix} \right),$$

where μ is a constant depending on the total concentration, and the steady-state concentrations for $[(A^-)^-]$ and $[(A)^-X^+]$ are

$$[(A^-)^-] = \frac{\widetilde{K_1}}{[H^+]}[(A)^-], \tag{2.20}$$
$$[(A)^-X^+] = J[X^+][(A)^-].$$

Using the total concentration relation, which is similar to Eq. 2.18, we have

$$\begin{aligned} T &= [A] + [AH^+] + [(AH^+)^-] + [(A)^-] + [(A^-)^-] + [(A)^-X^+] \\ &= [A] + [AH^+] + [(AH^+)^-] + [(A)^-](1 + \frac{\widetilde{K_1}}{[H^+]} + J[X^+]). \end{aligned}$$

Here, we can pick a suitable constant μ in Eq. 2.19 to fit the total concentration restriction. However, in order to compute individual concentrations, we need to know the following parameters.

$$K_2 = \frac{k_2}{k_{-2}},\ L_2 = \frac{l_2}{l_{-2}},\ L_3 = \frac{l_3}{l_{-3}},\ M_3 = \frac{m_+}{m_-},\ \widetilde{K_1} = \frac{\widetilde{k_1}}{\widetilde{k_{-1}}},\ \widetilde{K_2} = \frac{\widetilde{k_2}}{\widetilde{k_{-2}}} \tag{2.21}$$

$$KL_{-2} = \frac{\widetilde{k_{-2}}}{l_{-2}},\ KL_{23} = \frac{\widetilde{k_2}}{l_{-3}},\ tKK_{-2} = \frac{\widetilde{k_{-2}}}{k_{-2}},\ ML_3 = \frac{m_-}{l_{-3}},\ JX = J[X^+]. \tag{2.22}$$

In Figure 2.3a, we choose

$$K_2 = 10^{-4},\ L_2 = 10^{-3.25},\ L_3 = 10^{-3.25},\ M_3 = 10^{-4},\ \widetilde{K_1} = 10^{-6.87},\ \widetilde{K_2} = 10^{-4}$$
$$KL_{-2} = 1,\ KL_{23} = 1,\ tKK_{-2} = 1,\ ML_3 = 1,\ JX = 0.3$$

and if we take log of each concentration, we can have a pH-logci diagram such as Figure 2.3b. Now, we are interested in which parameters in Eq. 2.21 and Eq. 2.22 influence our results the most. If we write the original concentrations as a vector

$$\overrightarrow{ori} = ([A]\ [AH^+]\ [(AH^+)^-]\ [(A]^-]\ [(A^-)^-]\ [(A)^-X^+])^T,$$

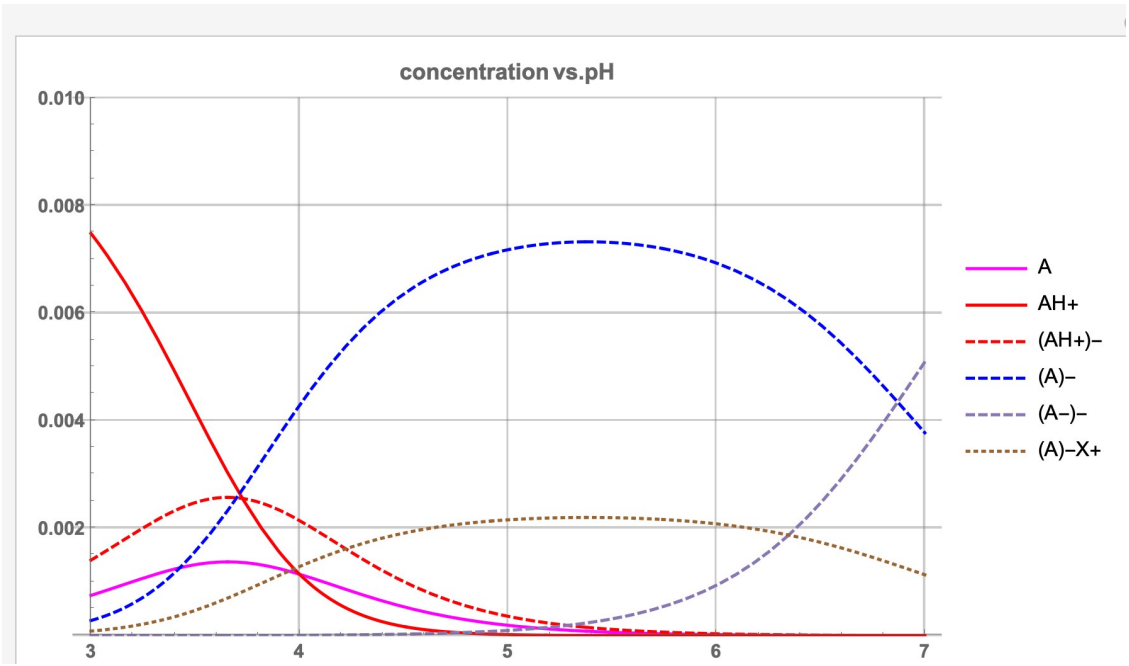

(a) Concentrations v.s. pH.

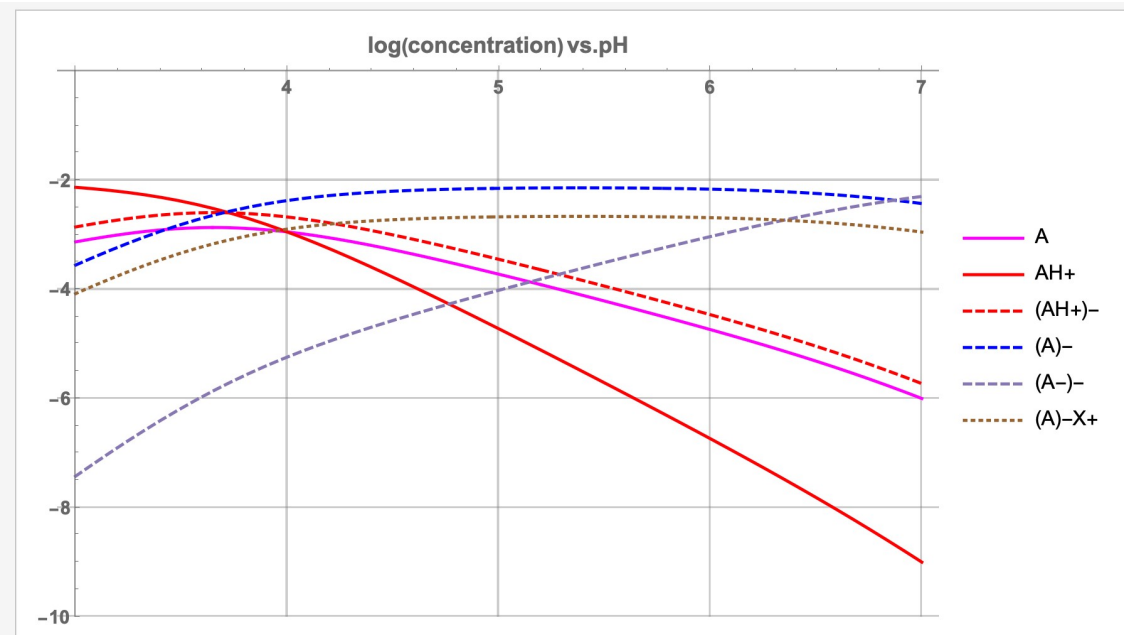

(b) Log Concentrations v.s. pH.

Figure 2.3: Steady-state *vs.* pH

and perturb all of the coefficients by a little amount '$\triangle$,' then using the Taylor expansion, we will have the result concentration $\overrightarrow{end}$, which is also a vector, satisfing

$$\overrightarrow{end} \approx \overrightarrow{ori} + \begin{pmatrix} \frac{\partial}{\partial K_2}[A] & \cdots & \frac{\partial}{\partial JX}[A] \\ \frac{\partial}{\partial K_2}[AH^+] & \cdots & \frac{\partial}{\partial JX}[AH^+] \\ \frac{\partial}{\partial K_2}[(AH^+)^-] & \cdots & \frac{\partial}{\partial JX}[(AH^+)^-] \\ \frac{\partial}{\partial K_2}[(A]^-] & \cdots & \frac{\partial}{\partial JX}[(A]^-] \\ \frac{\partial}{\partial K_2}[(A^-)^-] & \cdots & \frac{\partial}{\partial JX}[(A^-)^-] \\ \frac{\partial}{\partial K_2}[(A)^-X^+] & \cdots & \frac{\partial}{\partial JX}[(A)^-X^+] \end{pmatrix} \begin{pmatrix} \triangle K2 \\ \triangle L2 \\ \triangle L3 \\ \triangle M3 \\ \triangle \widetilde{K1} \\ \triangle \widetilde{K2} \\ \triangle KL_{-2} \\ \triangle KL_{23} \\ \triangle tkk_{-2} \\ \triangle ML_3 \\ \triangle JX \end{pmatrix}.$$

The angle between $\overrightarrow{ori}$ and $\overrightarrow{end}$ represents the influence of the perturbation. Hence, if we calculate each angle with respect to the small perturbation of each parameter, we can figure out which parameters are the most important ones. To process this, we first take the partial derivative of the steady-state concentrations in Eq. 2.19 and Eq. 2.20 with respect to the coefficients in Eq. 2.21 and Eq. 2.22. And then compute each $\overrightarrow{end}$ when we just perturb one parameter in δ amount. Finally, the angle between $\overrightarrow{ori}$ and $\overrightarrow{end}$ is

$$\text{arc}cos\frac{< \overrightarrow{ori}, \overrightarrow{end} >}{\parallel \overrightarrow{ori} \parallel \cdot \parallel \overrightarrow{end} \parallel}.$$

In figure 2.5a and 2.6a, we found that $\widetilde{K_1} = \frac{\widetilde{k_1}}{\widetilde{k_{-1}}}$ has the largest effect when pH is between 4 to 7, while $K_2 = \frac{k_2}{k_{-2}}$ and $L_2 = \frac{l_2}{l_{-2}}$ influence the results in lower pH such as pH≤ 4. Three parameters are the most important ones.

Besides, $\widetilde{K_2} = \frac{\widetilde{k_2}}{\widetilde{k_{-2}}}$ has the effect of pH around 3.7, while $L_3 = \frac{l_3}{l_{-3}}$ changes the results at pH$\leq$ 4 and $J[X^+] = \frac{j_+}{j_-}[X^+]$ affects if pH$\geq$ 4. On the other hand, the less important parameter is $tKK_{-2} = \frac{\widetilde{k_{-2}}}{k_{-2}}$ through all pH. It basically does not influence the results.

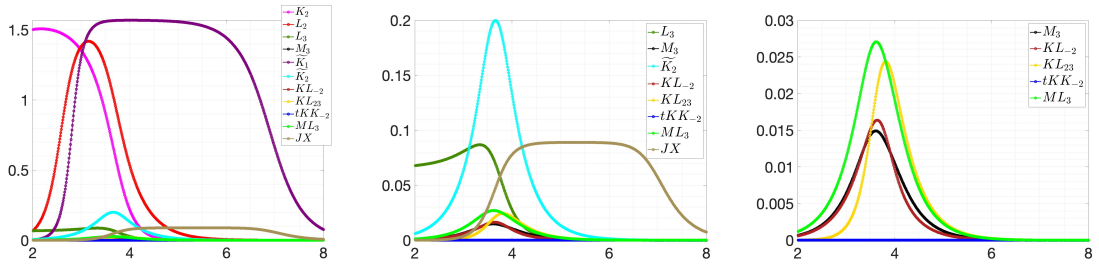

(a) All parameters **(b)** Exclude the largest 3. **(c)** Exclude the largest 6.

Figure 2.4: Sensitivities of parameters when the perturbation is $\delta = 10^{-1}$, angle in radian v.s. pH.

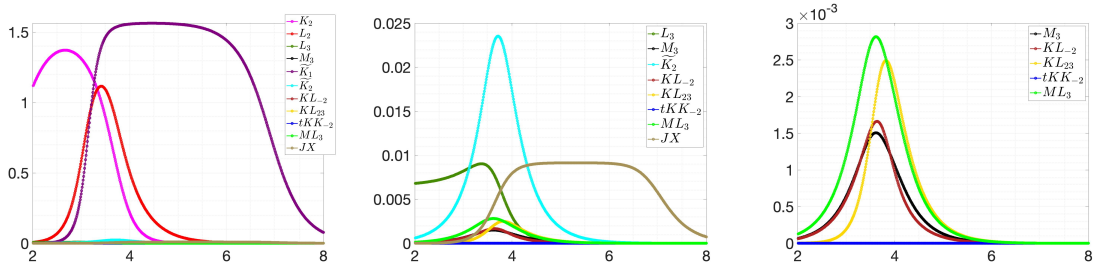

(a) All parameters **(b)** Exclude the largest 3. **(c)** Exclude the largest 6.

Figure 2.5: Sensitivities of parameters when the perturbation is $\delta = 10^{-2}$, angle in radian v.s. pH.

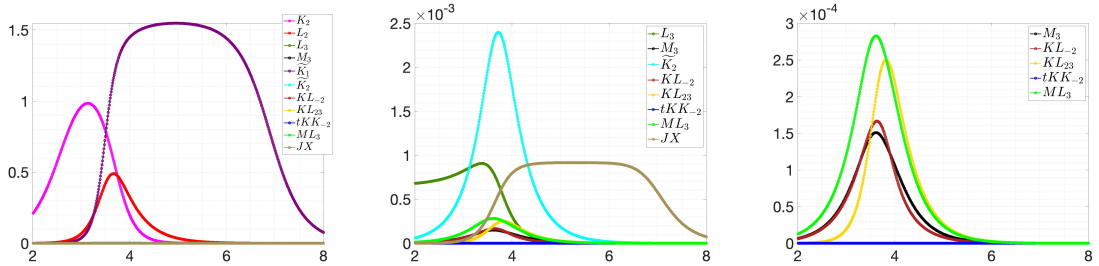

(a) All parameters. **(b)** Exclude the largest 3. **(c)** Exclude the largest 6.

Figure 2.6: Sensitivities of parameters when the perturbation is $\delta = 10^{-3}$, angle in radian v.s. pH.

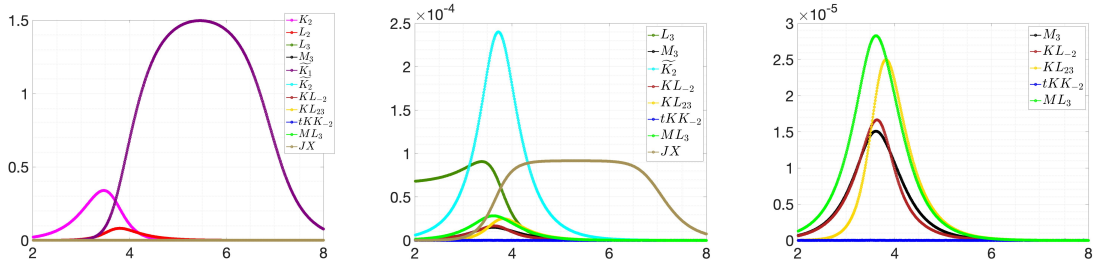

(a) All parameters. **(b)** Exclude the largest 3. **(c)** Exclude the largest 6.

Figure 2.7: Sensitivities of parameters when the perturbation is $\delta = 10^{-4}$, angle in radian v.s. pH.

2.3 Intermolecular association

The results of Section 2.1, as shown in Figure 2.1, demonstrate that the basic monomer scheme implies that colorless species dominate from pH 2 to 7. This includes the pH range of typical cell vacuoles. Anthocyanins should be in colorless form in plants. How is it, then, that colored anthocyanin species are observed in plant cells? Another possible reason for the existence of colored species is intermolecular association with molecule such as cellulose, microtubules, or proteins.

Consider the following basic full scheme with X, where the X represents some compounds such as protein in the cytoplasm.

$$
\begin{array}{llllll}
A^- + H^+ \underset{k_1}{\overset{k_{-1}}{\rightleftharpoons}} A, & & AH^+ + X & \underset{k_7}{\overset{k_{-7}}{\rightleftharpoons}} & AX^+ & \\
A + H^+ \underset{k_2}{\overset{k_{-2}}{\rightleftharpoons}} AH^+, & & B & \underset{k_{-6}}{\overset{k_6}{\rightleftharpoons}} & B^- + H^+ & \\
 & AH^+ \underset{k_{-3}}{\overset{k_3}{\rightleftharpoons}} & B & + H^+ & & \\
 & & B & \underset{k_{-4}}{\overset{k_4}{\rightleftharpoons}} C \underset{k_{-5}}{\overset{k_5}{\rightleftharpoons}} & C^- + H^+ &
\end{array}
$$

Similarly, using the law of mass action, we have the following system of ordinary differential equations:

$$\begin{aligned}
\frac{d}{dt}[A^-] =& \{-k_{-1}[A^-][H^+] + k_1[A]\} \\
\frac{d}{dt}[A] =& -\{-k_{-1}[A^-][H^+] + k_1[A]\} + \{-k_{-2}[A][H^+] + k_2[AH^+]\} \\
\frac{d}{dt}[AH^+] =& -\{-k_{-2}[A][H^+] + k_2[AH^+]\} + \{-k_3[AH^+] + k_{-3}[B][H^+]\} \\
&+ \{-k_{-7}[AH^+][X] + k_7[AX^+]\} \\
\frac{d}{dt}[B] =& -\{-k_3[AH^+] + k_{-3}[B][H^+]\} + \{-k_4[B] + k_{-4}[C]\} + \{-k_6[B] + k_{-6}[B^-][H^+]\} \\
\frac{d}{dt}[B^-] =& -\{-k_6[B] + k_{-6}[B^-][H^+]\} \\
\frac{d}{dt}[C] =& -\{-k_4[B] + k_{-4}[C]\} + \{-k_5[C] + k_{-5}[C^-][H^+]\} \\
\frac{d}{dt}[C^-] =& -\{-k_5[C] + k_{-5}[C^-][H^+]\} \\
\frac{d}{dt}[AX^+] =& -\{-k_{-7}[AH^+][X] + k_7[AX^+]\} \\
\frac{d}{dt}[X] =& \{-k_{-7}[AH^+][X] + k_7[AX^+]\}.
\end{aligned}$$

We are looking the steady-state of this system. Besides Eq. 2.11 - Eq. 2.17, writing all the concentrations in terms of $[A]$, we have an additional relation

$$\frac{[X]}{[AX^+]} = \frac{k_7}{k_{-7}[AH^+]} = \frac{K_7}{\frac{[H^+]}{K_2} \times [A]} = \frac{K_2 \times K_7}{[H^+][A]}. \tag{2.23}$$

Assuming $[T]$ is the total concentration of anthocyanin, and $[TX]$ is the total concentration including X, the conservation laws are

$$[T] = [A^-] + [A] + [AH^+] + [B] + [B^-] + [C] + [C^-] + [AX^+] \tag{2.24}$$

$$[TX] = [X] + [AX^+]. \tag{2.25}$$

Substituting Eq. 2.23 into Eq. 2.25, we have

$$[AX^+] = \frac{[H^+] \times [A]}{K_7 \times K_2 + [H^+] \times [A]} \times [TX] \tag{2.26}$$

$$[X] = \frac{K_7 \times K_2}{K_7 \times K_2 + [H^+] \times [A]} \times [TX]. \tag{2.27}$$

Then the conservation law, Eq. 2.24, becomes

$$\begin{aligned}[T] =\{&\frac{K_1}{[H^+]} + 1 + \frac{[H^+]}{K_2} + \frac{K_3}{K_2} + \frac{K_6 \times K_3}{[H^+] \times K_2} + \frac{K_4 \times K_3}{K2} \\ &+ \frac{K_5 \times K_4 \times K_3}{K_2 \times [H^+]} + \frac{[H^+] \times [TX]}{K_7 \times K_2 + [H^+] \times [A]}\} \times [A].\end{aligned} \tag{2.28}$$

To plot our results, we use the same equilibrium constants as Eq. 2.9 and Eq. 2.10, and set

$$K_7 = \frac{k_7}{k_{-7}} = 10^{-4}.$$

We assume $[TX]$ to be proportional to $[T]$, and then graph the results in Figure 2.8 when $[TX] = 0.4[T]$ and $[TX] = 0.8[T]$. We found that AX^+ appeared when pH≤ 6, which means we might have some color in the pH range 3 to 6 due to the species AX^+. These results depend on the concentration of X and the choice of the equilibrium constant K_7, but they are very different from the basic monomer scheme result in Figure 2.1.

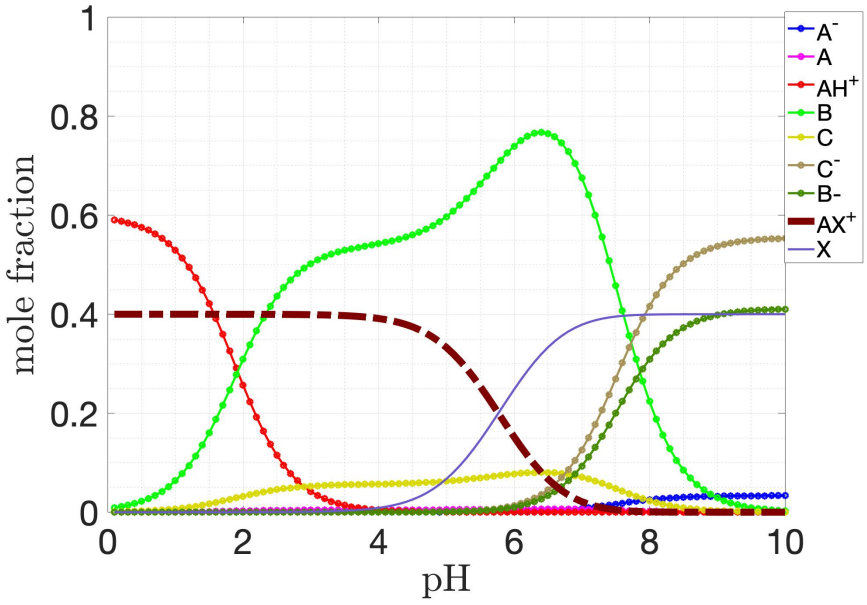

(a) $[\mathrm{TX}] = 0.4[\mathrm{T}]$

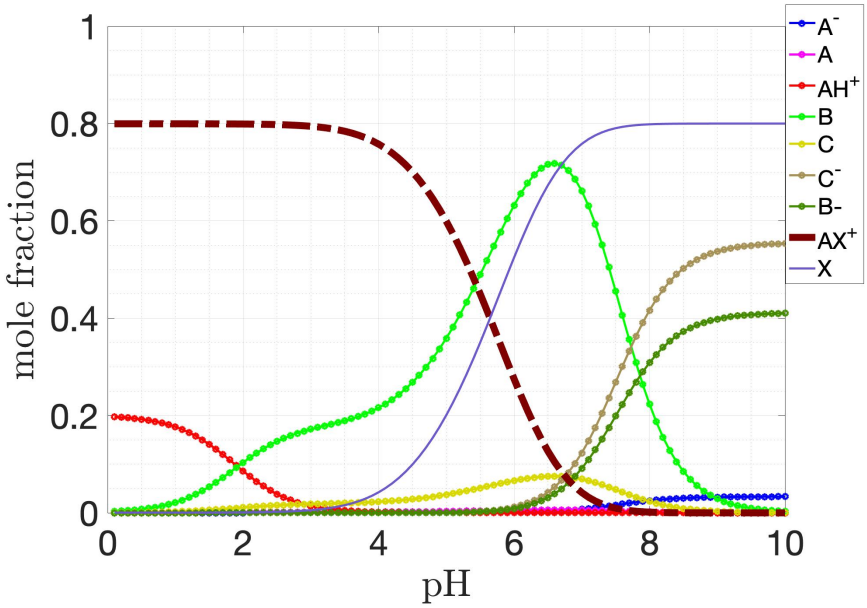

(b) $[\mathrm{TX}] = 0.8[\mathrm{T}]$

Figure 2.8: Steady-state mole fractions of species with X.

2.4 Self association

Recall the results of Section 2.1 as shown in Figure 2.1 and the big question we are trying to answer–why do flowers have colors? We suggest that association is the key to answering this question. As a simple example, consider the case of an aqueous anthocyanin solution buffered at pH 2.5. Figure 2.9 (a) shows that the colorless species B has the largest mole fraction at this pH value, and the only other species with a significant mole fraction is the red AH^+. Also assume that dimerization is the only association that occurs, according to the kinetic equation

$$A_1 \underset{k_-}{\overset{k_+}{\rightleftharpoons}} A_2,$$

where A_1 is the monomer and A_2 is the dimer. Denoting the total moles of anthocyanins in the container of volume V as T, according to the Law of Mass Action, the *mole fraction* $\hat{A}_1$ of monomer in the solution obeys the rate equation

$$\frac{d\hat{A}_1}{dt} = -2\hat{K}\hat{A}_1^2 + 1 - \hat{A}_1, \quad \text{for} \quad \hat{K} = \frac{k_+ T}{k_- V}. \tag{2.29}$$

At steady state, $\hat{A}_1 = (-1 + \sqrt{1 + 8\hat{K}})/(4\hat{K})$. The crucial observation is that $\hat{A}_1$ decreases (and

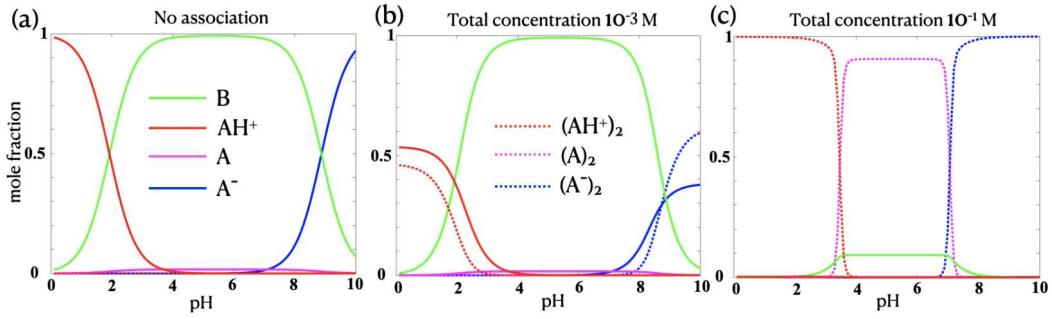

Figure 2.9: Mole fractions of anthocyanin species as a function of pH, assuming (a) no association, or association to form dimers and a total concentration of (b) 10^{-3} M or (c) 10^{-1} M.

the mole fraction of dimers increases) with the concentration T/V. If the pH is such that, say AH^+ and the colorless B (which does not associate with itself), are present in significant concentrations,

this nonlinear effect still functions to drive the equilibrium away from B and towards the (red) AH^+ dimer. The result is enhanced color. Compare the mole fractions of the various anthocyanin forms as a function of pH assuming no association, as shown in Figure 2.9 (a), with analogous relationships assuming association (to form dimers) and a total concentration of 10^{-3} M and 10^{-1} M, shown in Figure 2.9 (b,c); monomeric species are plotted in solid lines, and dimers are plotted in dotted lines. At 10^{-3} M, associated species are present, but at 10^{-1} M the nonlinear effect is strong enough to drive the equilibrium towards the colored species even at pH values 3-7.

In this subsection, we extend our scheme to include self association. Each of the A^-, A, and AH^+ anthocyanin species is known to form associative complexes with members of its own species (as in the steady-state graphs of Figure 2.9), and there is likely also association of A with AH^+. The core reactions, if the maximum associate has size N, are

$$\begin{array}{ccc}
\mathrm{A^- + A^-} \underset{\mathrm{j_{1,-2}}}{\overset{\mathrm{j_{1,2}}}{\rightleftharpoons}} (\mathrm{A^-})_2 & \mathrm{A + A} \underset{\mathrm{j_{2,-2}}}{\overset{\mathrm{j_{2,2}}}{\rightleftharpoons}} (\mathrm{A})_2 & \mathrm{AH^+ + AH^+} \underset{\mathrm{j_{3,-2}}}{\overset{\mathrm{j_{3,2}}}{\rightleftharpoons}} (\mathrm{AH^+})_2 \\
\mathrm{A^- + (A^-)_2} \underset{\mathrm{j_{1,-3}}}{\overset{\mathrm{j_{1,3}}}{\rightleftharpoons}} (\mathrm{A^-})_3 & \mathrm{A + (A)_2} \underset{\mathrm{j_{2,-3}}}{\overset{\mathrm{j_{2,3}}}{\rightleftharpoons}} (\mathrm{A})_3 & \mathrm{AH^+ + (AH^+)_2} \underset{\mathrm{j_{3,-3}}}{\overset{\mathrm{j_{3,3}}}{\rightleftharpoons}} (\mathrm{AH^+})_3 \\
\vdots & \vdots & \vdots \\
\mathrm{A^- + (A^-)_{N-1}} \underset{\mathrm{j_{1,-N}}}{\overset{\mathrm{j_{1,N}}}{\rightleftharpoons}} (\mathrm{A^-})_N & \mathrm{A + (A)_{N-1}} \underset{\mathrm{j_{2,-N}}}{\overset{\mathrm{j_{2,N}}}{\rightleftharpoons}} (\mathrm{A})_N & \mathrm{AH^+ + (AH^+)_{N-1}} \underset{\mathrm{j_{3,-N}}}{\overset{\mathrm{j_{3,N}}}{\rightleftharpoons}} (\mathrm{AH^+})_N
\end{array} \tag{2.30}$$

as well as $A \cdot AH^+$ association

$$\begin{aligned}
\mathrm{A} + \mathrm{AH}^+ &\underset{\mathrm{j}_{4,-2}}{\overset{\mathrm{j}_{4,2}}{\rightleftharpoons}} \mathrm{A} \cdot \mathrm{AH}^+ \\
\mathrm{AH}^+ + \mathrm{A} \cdot \mathrm{AH}^+ &\underset{\mathrm{j}_{4,-3}}{\overset{\mathrm{j}_{4,3}}{\rightleftharpoons}} \mathrm{A} \cdot (\mathrm{AH}^+)_2 \\
\mathrm{A} + \mathrm{A} \cdot (\mathrm{AH}^+)_2 &\underset{\mathrm{j}_{4,-4}}{\overset{\mathrm{j}_{4,4}}{\rightleftharpoons}} (\mathrm{A})_2 \cdot (\mathrm{AH}^+)_2 \\
\mathrm{AH}^+ + (\mathrm{A})_2 \cdot (\mathrm{AH}^+)_2 &\underset{\mathrm{j}_{4,-5}}{\overset{\mathrm{j}_{4,5}}{\rightleftharpoons}} (\mathrm{A})_2 \cdot (\mathrm{AH}^+)_3 \\
&\vdots \\
\mathrm{A} + (\mathrm{A})_{\frac{\mathrm{N}}{2}-1} \cdot (\mathrm{AH}^+)_{\frac{\mathrm{N}}{2}} &\underset{\mathrm{j}_{4,-\mathrm{N}}}{\overset{\mathrm{j}_{4,\mathrm{N}}}{\rightleftharpoons}} (\mathrm{A})_{\frac{\mathrm{N}}{2}} \cdot (\mathrm{AH}^+)_{\frac{\mathrm{N}}{2}}
\end{aligned} \tag{2.31}$$

Here the association equilibrium constants are assumed to not depend on n; that is, we are assuming an *isodesmic model*. Based on measurements in [34], the equilibrium constants are chosen to be

$$J_1 = \frac{j_{1,n}}{j_{1,-n}} = 3200, \quad J_2 = \frac{j_{2,n}}{j_{2,-n}} = 12800, \quad J_3 = \frac{j_{3,n}}{j_{3,-n}} = 9600, \quad J_4 = \frac{j_{4,n}}{j_{4,-n}} = 11200, \tag{2.32}$$
$$j_{1,n} = j_{2,n} = j_{3,n} = j_{4,n} = 8000, \text{for all } n \in \{1, 2, \cdots, N\}.$$

Now we consider the basic scheme as in Eq. 2.1 with the associations mentioned above. Using the same equilibrium constants as Eq. 2.9 and Eq. 2.10, the concentration changing rates are as follows: For $[A^-]$ and its associations,

$$\begin{aligned}
\frac{d}{dt}[A^-] &= \{-k_{-1}[A^-][H^+] + k_1[A]\} + 2\{-j_{1,2}[A^-][A^-] + j_{1,-2}[(A^-)_2]\} \\
&\quad + \{-j_{1,3}[A^-][(A^-)_2] + j_{1,-3}[(A^-)_3]\} + \cdots + \{-j_{1,N}[A^-][(A^-)_{N-1}] + j_{1,-N}[(A^-)_N]\}
\end{aligned} \tag{2.33}$$

$$\frac{d}{dt}[(A^-)_2] = -\{-j_{1,2}[A^-][A^-] + j_{1,-2}[(A^-)_2]\} + \{-j_{1,3}[A^-][(A^-)_2] + j_{1,-3}[(A^-)_3]\} \tag{2.34}$$

$$\vdots$$

$$\frac{d}{dt}[(A^-)_N] = -\{-j_{1,N}[A^-][(A^-)_{N-1}] + j_{1,-N}[(A^-)_N]\}. \tag{2.35}$$

Solving for steady-state, the concentrations are

$$
\begin{aligned}
[(A^-)_N] &= \frac{j_{1,N}}{j_{1,-N}}[A^-][(A^-)_{N-1}] = J_1[A^-][(A^-)_{N-1}] \\
[(A^-)_{N-1}] &= \frac{j_{1,N-1}}{j_{1,-(N-1)}}[A^-][(A^-)_{N-2}] = J_1[A^-][(A^-)_{N-2}] \\
&\vdots \\
[(A^-)_2] &= \frac{j_{1,2}}{j_{1,-2}}[A^-][A^-] = J_1[A^-][A^-] \\
[A^-] &= \frac{K_1}{[H^+]} \times [A].
\end{aligned}
$$

That is,

$$
[A^-] = \frac{K_1}{[H^+]} \times [A], \;\; [(A^-)_n] = (J_1)^{n-1}[A^-]^n, \text{for } n \in \{2, 3, \cdots, N\}. \tag{2.36}
$$

For $[A]$ and its associations,

$$
\begin{aligned}
\frac{d}{dt}[A] =& - \{-k_{-1}[A^-][H^+] + k_1[A]\} + \{-k_{-2}[A][H^+] + k_2[AH^+]\} \\
&+ 2\{-j_{2,2}[A][A] + j_{2,-2}[(A)_2]\} + \{-j_{2,3}[A][(A)_2] + j_{2,-3}[(A)_3]\} \\
&+ \cdots + \{-j_{2,N}[A][(A)_{N-1}] + j_{2,N}[(A)_N]\} \\
&+ \{-j_{4,2}[A][AH^+] + j_{4,-2}[A \cdot AH^+]\} \\
&+ \{-j_{4,4}[A][A \cdot (AH^+)_2] + j_{4,-4}[(A)_2 \cdot (AH^+)_2]\} \\
&+ \cdots + \{-j_{4,N}[A][(A)_{\frac{N}{2}-1} \cdot (AH^+)_{\frac{N}{2}}] + j_{4,-N}[(A)_{\frac{N}{2}} \cdot (AH^+)_{\frac{N}{2}}]\} \qquad (2.37) \\
\frac{d}{dt}[(A)_2] =& - \{-j_{2,2}[A][A] + j_{2,-2}[(A)_2]\} + \{-j_{2,3}[A][(A)_2] + j_{2,-3}[(A)_3]\} \qquad (2.38) \\
&\vdots \\
\frac{d}{dt}[(A)_N] =& - \{-j_{2,N}[A][(A)_{N-1}] + j_{2,N}[(A)_N]\}. \qquad (2.39)
\end{aligned}
$$

By the similar calculation, the association concentrations are

$$
[(A)_n] = (J_2)^{n-1}[A]^n, \text{for } n \in \{2, 3, \cdots, N\}. \tag{2.40}
$$

For $[AH^+]$ and its associations,

$$\begin{aligned}
\frac{d}{dt}[AH^+] =& -\{-k_{-2}[A][H^+] + k_2[AH^+]\} + \{-k_3[AH^+] + k_{-3}[B][H^+]\} \\
&+ 2\{-j_{3,2}[AH^+][AH^+] + j_{3,-2}[(AH^+)_2]\} \\
&+ \{-j_{3,3}[AH^+][(AH^+)_2] + j_{3,-3}[(AH^+)_3]\} \\
&+ \cdots + \{-j_{3,N}[AH^+][(AH^+)_{N-1}] + j_{3,N}[(AH^+)_N]\} \\
&+ \{-j_{4,2}[A][AH^+] + j_{4,-2}[A \cdot AH^+]\} \\
&+ \{-j_{4,3}[A \cdot AH^+][AH^+] + j_{4,-3}[A \cdot (AH^+)_2]\} \\
&+ \cdots + \{-j_{4,N-1}[(A)_{\frac{N}{2}-1} \cdot (AH^+)_{\frac{N}{2}-1}][AH^+] + j_{4,-(N-1)}[(A)_{\frac{N}{2}-1} \cdot (AH^+)_{\frac{N}{2}}]\} \qquad (2.41) \\
\frac{d}{dt}[(AH^+)_2] =& -\{-j_{3,2}[AH^+][AH^+] + j_{3,-2}[(AH^+)_2]\} \\
&+ \{-j_{3,3}[AH^+][(AH^+)_2] + j_{3,-3}[(AH^+)_3]\} \qquad (2.42) \\
&\vdots \\
\frac{d}{dt}[(AH^+)_N] =& -\{-j_{3,N}[AH^+][(AH^+)_{N-1}] + j_{3,-N}[(AH^+)_N]\}. \qquad (2.43)
\end{aligned}$$

The steady-state condition implies

$$[(AH^+)_n] = (J_3)^{n-1}[AH^+]^n, \text{for } n \in \{2, 3, \cdots, N\}. \qquad (2.44)$$

For $[A \cdot AH^+]$ and its associations,

$$\begin{aligned}
\frac{d}{dt}[A \cdot AH^+] =& -\{-j_{4,2}[A][AH^+] + j_{4,-2}[A \cdot AH^+]\} \\
&+ \{-j_{4,3}[A \cdot AH^+][AH^+] + j_{4,-3}[A \cdot (AH^+)_2]\} \qquad (2.45) \\
\frac{d}{dt}[A \cdot (AH^+)_2] =& -\{-j_{4,3}[A \cdot AH^+][AH^+] + j_{4,-3}[A \cdot (AH^+)_2]\} \\
&+ \{-j_{4,4}[A][A \cdot (AH^+)_2] + j_{4,-4}[(A)_2 \cdot (AH^+)_2]\} \qquad (2.46) \\
\frac{d}{dt}[(A)_2 \cdot (AH^+)_2] =& -\{-j_{4,4}[A][A \cdot (AH^+)_2] + j_{4,-4}[(A)_2 \cdot (AH^+)_2]\} \\
&+ \{-j_{4,5}[(A)_2 \cdot (AH^+)_2][AH^+] + j_{4,-5}[(A)_2 \cdot (AH^+)_3]\} \qquad (2.47) \\
&\vdots \\
\frac{d}{dt}[(A)_{\frac{N}{2}} \cdot (AH^+)_{\frac{N}{2}}] =& -\{-j_{4,N}[A][(A)_{\frac{N}{2}-1} \cdot (AH^+)_{\frac{N}{2}}] + j_{4,-N}[(A)_{\frac{N}{2}} \cdot (AH^+)_{\frac{N}{2}}]\}. \qquad (2.48)
\end{aligned}$$

The steady-state concentrations are

$$[(A)_n \cdot (AH^+)_n] = (J_4)^{2n-1}[A]^n[AH^+]^n, \text{for } n \in \{1, 2, \cdots, \frac{N}{2}\}, \qquad (2.49)$$

$$[(A)_{n-1} \cdot (AH^+)_n] = (J_4)^{2n-2}[A]^{n-1}[AH^+]^n, \text{ for } n \in \{2, 3, \cdots, \frac{N}{2}\}. \qquad (2.50)$$

For the other terms such as $[B]$, $[B^-]$, $[C]$ and $[C^-]$, we have

$$\frac{d}{dt}[B] = -\{-k_3[AH^+] + k_{-3}[B][H^+]\} + \{-k_4[B] + k_{-4}[C]\} + \{-k_6[B] + k_{-6}[B^-][H^+]\} \qquad (2.51)$$

$$\frac{d}{dt}[B^-] = -\{-k_6[B] + k_{-6}[B^-][H^+]\} \qquad (2.52)$$

$$\frac{d}{dt}[C] = -\{-k_4[B] + k_{-4}[C]\} + \{-k_5[C] + k_{-5}[C^-][H^+]\} \qquad (2.53)$$

$$\frac{d}{dt}[C^-] = -\{-k_5[C] + k_{-5}[C^-][H^+]\} \qquad (2.54)$$

These are the same concentration relations as what we did in Section 2.1, which are Eq. 2.14-Eq. 2.17. Substituting all the concentrations in terms of A into the conservation law

$$[T] = \sum_{j=1}^{N} j\left([(A^-)_j] + [A_j] + [(AH^+)_j]\right) + \sum_{n=1}^{N/2} 2n[(A)_n \cdot (AH^+)_n] + \sum_{n=2}^{N/2}(2n-1)[(A)_{n-1} \cdot (AH^+)_n] + [B] + [B^-] + [C] + [C^-], \tag{2.55}$$

we can find the mole fraction of each species depends on the pH value and total concentration. The following results are assuming the maximum association size N is 20. In Figure 2.10, we graph the mole fraction *vs.* the total concentration at the given pH value. At pH$= 3.5$, AH^+ and its associations dominate when the total concentration T is greater than $7.5 \times 10^{-3}M$. A and its associations dominate at pH$= 4$ if $T \geq 2.3 \times 10^{-3}M$, while they dominate at pH$= 5$ if $T \geq 1.8 \times 10^{-3}M$. This means if we take associations in count, the colored anthocyanin species dominate when we have higher total concentrations. In Figure 2.11, we graph the mole fraction *vs.* pH value at the given the total concentrations. We observed that when the total concentration goes up to $10^{-2}M$, A and its associations appear in the pH range 4 to 6. Because self association has the nonlinear effect, the mole fractions will be influenced dramatically by the total concentration. If we increase the total concentration up to $10^{-1}M$, the colored form of the anthocyanins dominates through the entire pH range. Note that the total concentrations in plant cells vary from $10^{-4}M$ to $1M$, so that our results are applicable to natural concentrations.

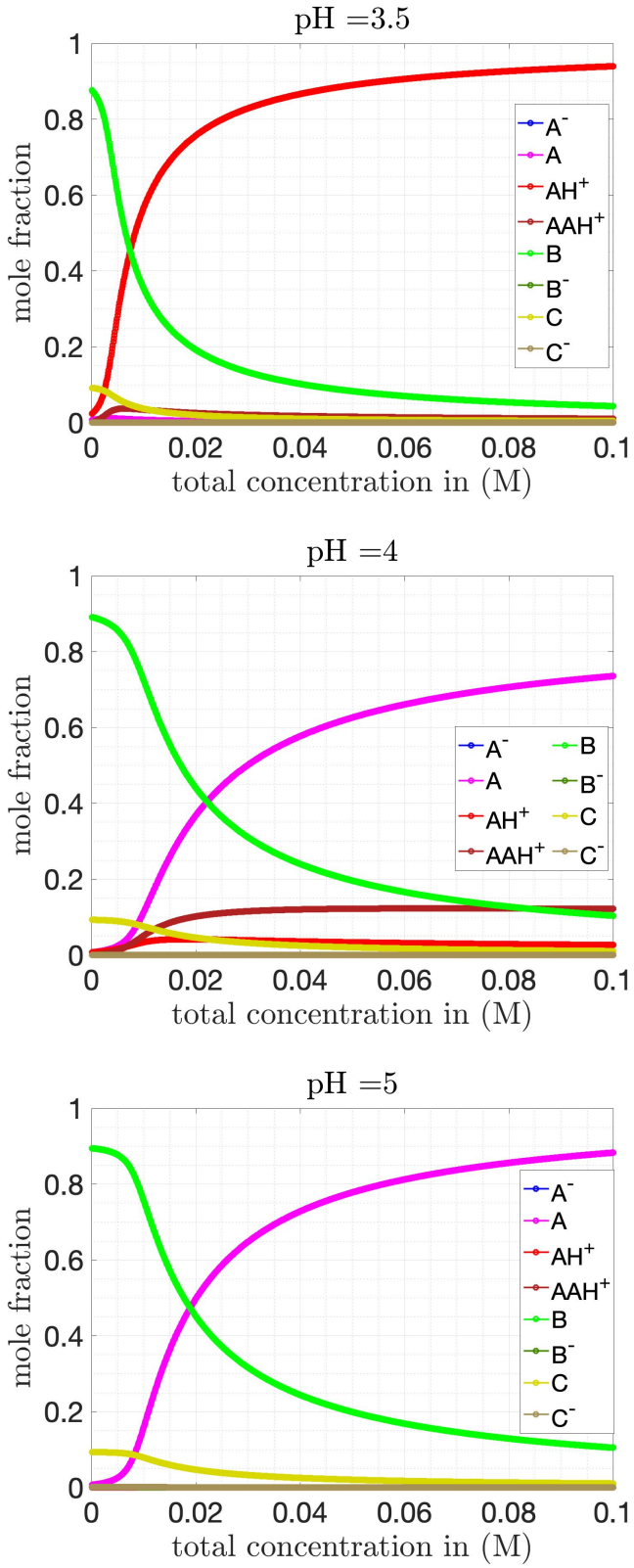

Figure 2.10: Mole fractions vs. the total concentration $[T]$ when pH values are $3.5, 4$, and 5.

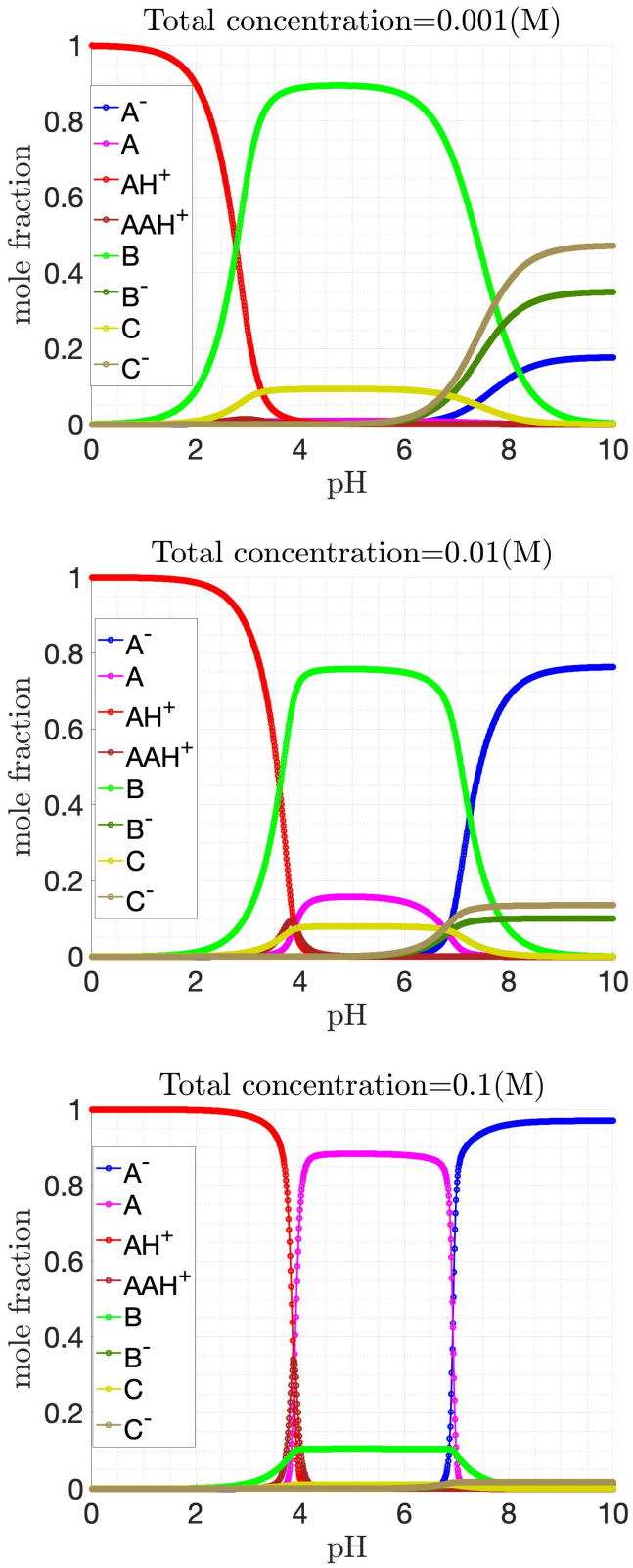

Figure 2.11: Mole fractions v.s. pH value when the total concentrations are $10^{-3}M, 10^{-2}M$, and $10^{-1}M$.

2.5 Evaporative experiments

In this section, we consider again the basic scheme with self association introduced in Section 2.4. But instead of finding the steady state, we are interested in the evolution of mole fractions as the total concentration changes over time. Experimentally, Prof. Thompson has achieved this by allowing a solution to evaporate, performing a so-called *evaporative experiment*. In an evaporative experiment, we start with a solution at a given (low) concentration and allow the water (or other solvent) to evaporate over time. The total concentration therefore becomes a function of time which can be slow relative to the reaction kinetics (so that the solution is effectively always in steady state for the given concentration) or fast. The rate of evaporation can be tuned using a humidity-controlled evaporative chamber, and thereby adjusted relative to the slow kinetics of formation of the colorless hemiketal species B from AH^+ and AH^+ from B. These experiments and models are relevant to the *in vivo* process of the senescence of flowers, in which the anthocyanin concentration increases dramatically and color changes occur. The reverse process of an increase in cell volume, accompanied by a decrease or increase in anthocyanin concentration (depending on the rate of anthocyanin synthesis) occurs as flower petals unfold from the bud. See Figure 2.12.

Figure 2.12: Blue morning glory started from the bud to fully open, and then closed.

Preliminary trials of evaporative experiments reveal a fundamental observation that opens another line of study. As the solvent (typically water) in the solution evaporates and the solution becomes more concentrated, we expect that the mole fractions of j-mers to increase, and in particular for larger j-mers to form. We have emphasized that anthocyanins are water soluble, but there is a limit

to this solubility as the size of the associated complex grows. Indeed, at concentrations on the order of $10^{-1}M$, Prof. Thompson has observed particles to form and come out of solution.

Consider an experiment that begins with an anthocyanin solution at concentration T_0 that has been allowed to come to the steady state. If the solution is at a mid-range pH value (3-8), it will be comprised mostly of the B species and be colorless. Using Eq. 2.33-Eq. 2.54, and the conservation law Eq. 2.55, we know the mole fraction of each species for a given total concentration. We now allow the solution to evaporate.

Numerically, we have modeled this scenario in discrete steps as follows: Choose a time step Δt and suppose that from times $t = 0$ to $t = \Delta t$, the total concentration changes from T_0 to T_1. We simulate this scenario by numerically integrating the system Eq. 2.33-Eq. 2.54 and Eq. 2.55 from time $t = 0$ to time $t = \Delta t$ assuming the initial total concentration T_0. We then multiply each species concentration in the system of ODEs by $\frac{T_1}{T_0}$. We then repeat the process, numerically integrating the system for another time step Δt assuming a total concentration of T_1. Again, we multiply all the fractions by $\frac{T_2}{T_1}$ and apply Eq. 2.33-Eq. 2.54 to them for Δt seconds. We iterate this process until the concentration reaches a desired final concentration (which we choose to be $T_f = 10^{-1}M$).

For this kinetic study, we require values for reaction rate constants such as k_{-1} and k_1 because we cannot set $\frac{d}{dt}[\bullet] = 0$ and use the ratio $\frac{k_1}{k_{-1}} = K_1$ to simply these equations. By reference [35] and [34] , we have $k_2 = 3 \times 10^6$, $k_{-2} = 3 \times 10^{10}$, $k_3 = 0.2849$, and $k_{-3} = 23.7$. Then we make a close guess for the other coefficients as follows.

$$k_1 = 3 \times 10^{3.2},\ k_{-1} = 3 \times 10^{10},\ k_4 = 3 \times 10^5,\ k_{-4} = 3 \times 10^{5.98}, \tag{2.56}$$

$$k_5 = 3 \times 10^{3.25},\ k_{-5} = 3 \times 10^{10},\ k_6 = 3 \times 10^{2.14},\ k_{-6} = 3 \times 10^{10}. \tag{2.57}$$

We assume that the smallest number m that $(\bullet)_m$ does not disassociate for $(\bullet)_{m+1}$ is a half of the largest number of association size N. Now we will simulate the experiment that started anthocyanins in the form of B with concentration equal to 10^{-3} M, let it stay for a day, and then

evaporated it until the total concentration is greater than 10^{-1} M within a time interval equal to 10×10^3 or 10×10^4 seconds as in Figure 2.13- Figure 2.18 in different pH values.

For the pH less than 4.5 (Figure 2.13-Figure 2.15), the length of the time interval does not matter to the mole fraction. We will have the similar results even if we evaporate aqueous solutions faster. However, when pH $\geq$ 4.5 (Figure 2.16-Figure 2.18), the longer time interval has the larger $[A]$ mole fraction. This shows the reaction rate influences the mole fractions more when pH value is higher.

If we started anthocyanins in the form of AH^+, after leaving it stay for a day, the results are similar to that we started from B. See Figure 2.19. These graphs are starting from the total concentration equal to 10^{-4} M, let it stay for a day, and then evaporated it until the total concentration is greater than 10^{-2} M within a time interval equal to 10×10^3 seconds. Because after a day , AH^+ turned to B to reach the steady-state in pH$= 3.5, 4,$ or 4.5.

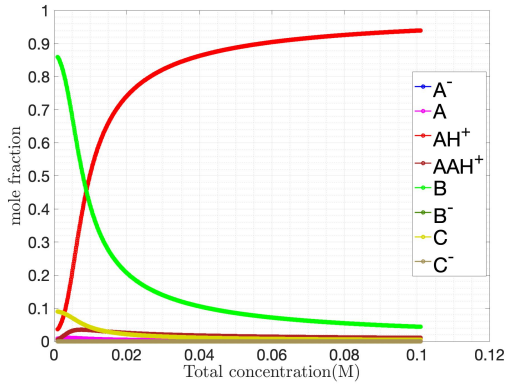

(a) 10×10^3 seconds (fast evaporate).

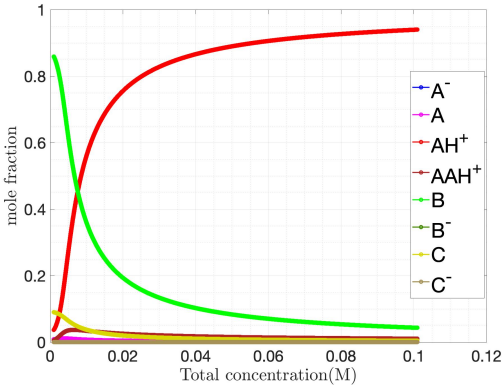

(b) 10×10^4 seconds (slow evaporate).

Figure 2.13: Evaporating simulations for $[T]$ from 10^{-3}M to 10^{-1}M when pH$= 3.5$

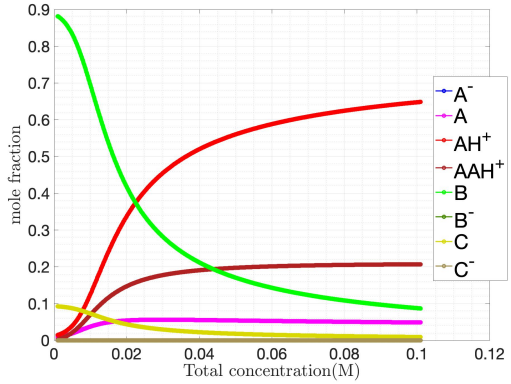

(a) 10×10^3 seconds (fast evaporate).

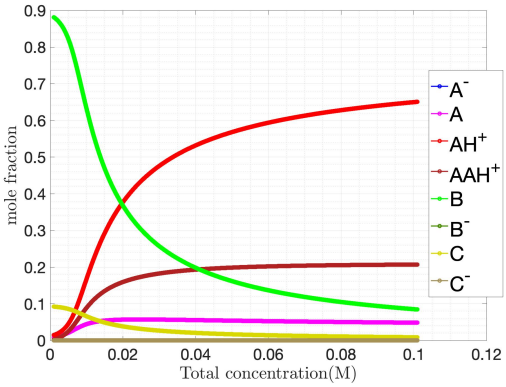

(b) 10×10^4 seconds (slow evaporate).

Figure 2.14: Evaporating simulations for $[T]$ from 10^{-3}M to 10^{-1}M when pH$= 3.8$

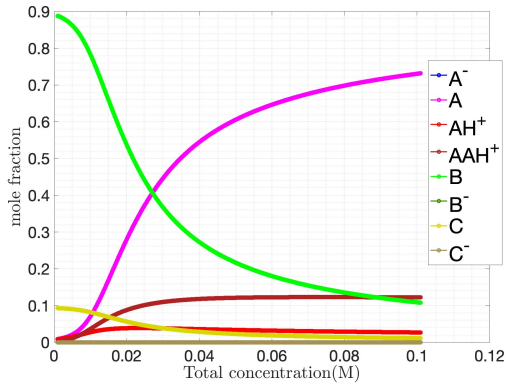

(a) 10×10^3 seconds (fast evaporate).

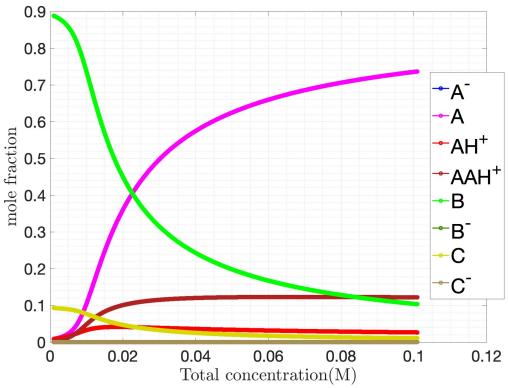

(b) 10×10^4 seconds (slow evaporate).

Figure 2.15: Evaporating simulations for $[T]$ from 10^{-3}M to 10^{-1}M when pH$= 4$

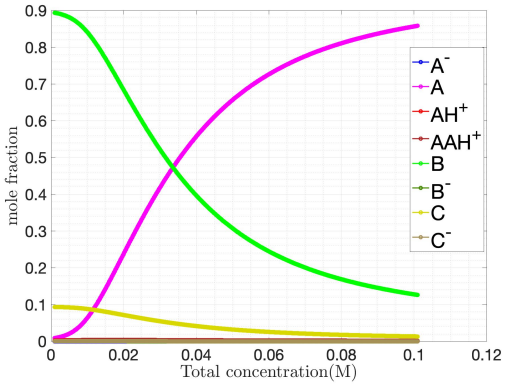

(a) 10×10^3 seconds (fast evaporate).

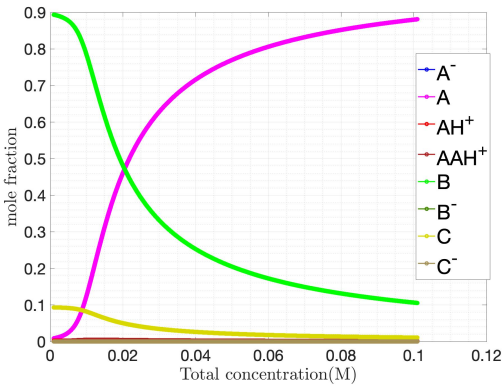

(b) 10×10^4 seconds (slow evaporate).

Figure 2.16: Evaporating simulations for $[T]$ from 10^{-3}M to 10^{-1}M when pH$= 4.5$

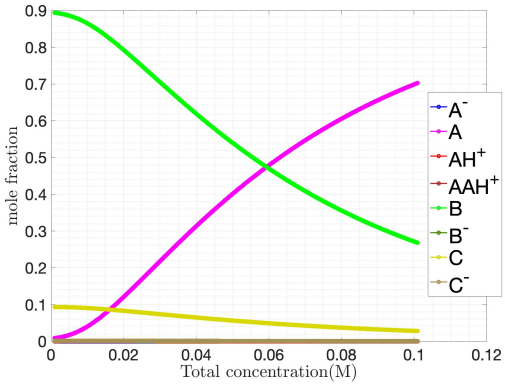

(a) 10×10^3 seconds (fast evaporate).

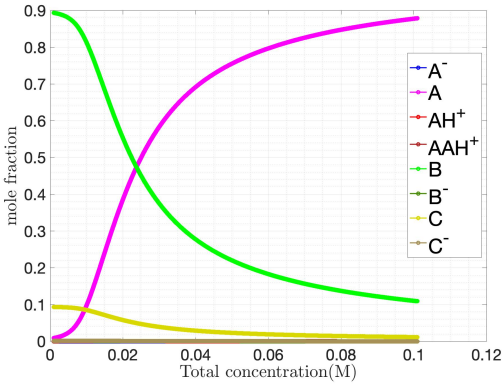

(b) 10×10^4 seconds (slow evaporate).

Figure 2.17: Evaporating simulations for $[T]$ from 10^{-3}M to 10^{-1}M when pH$= 5$

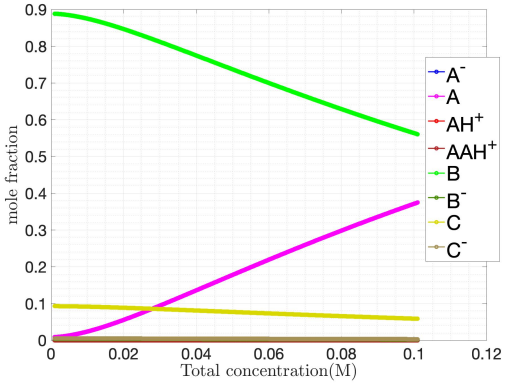

(a) 10×10^3 seconds (fast evaporate).

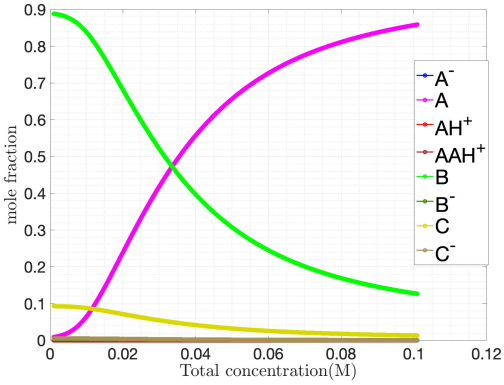

(b) 10×10^4 seconds (slow evaporate).

Figure 2.18: Evaporating simulations for $[T]$ from 10^{-3}M to 10^{-1}M when pH$= 5.5$

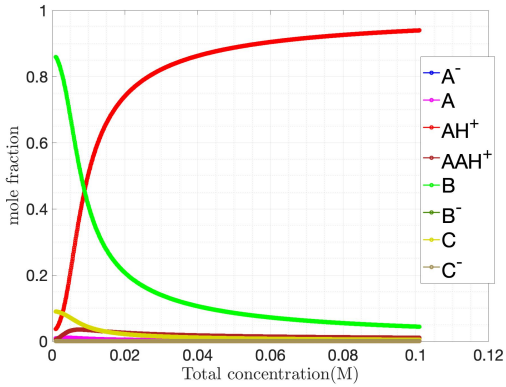

(a) pH= 3.5.

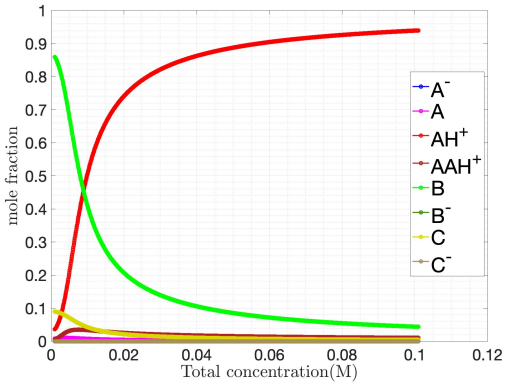

(b) pH= 3.5.

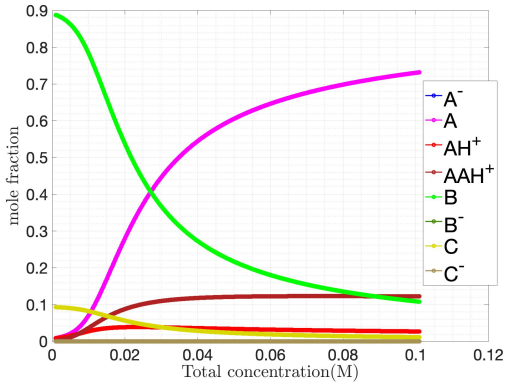

(c) pH= 4.

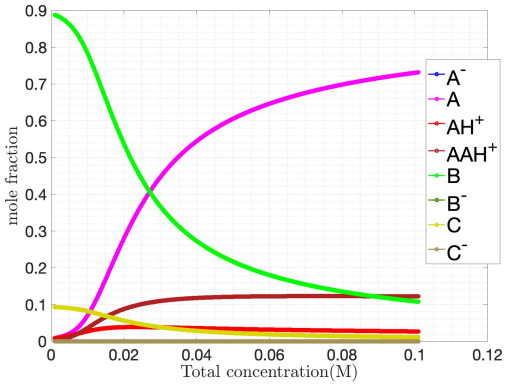

(d) pH= 4.

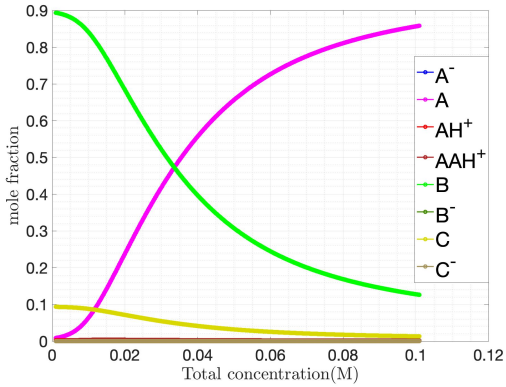

(e) pH= 4.5.

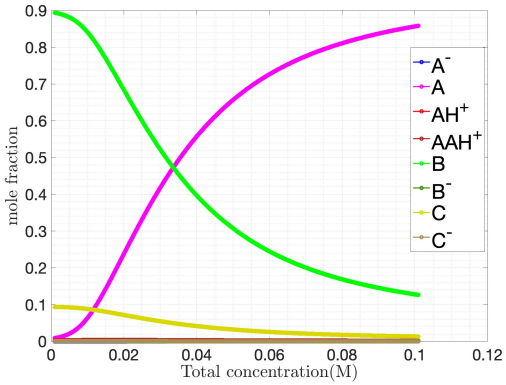

(f) pH= 4.5.

Figure 2.19: Evaporating from 10^{-3}M to 10^{-1}M for 10×10^3 seconds.
(L) Started from $[AH^+]$ (R) Started from $[B]$

2.6 Spatial anthocyanin patterns: An activator-inhibitor system

Spatial patterns in biological systems are often due to the feedback loops between activators and inhibitors [36, 37]. The simplest such pattern-forming system consists of one species of activator molecule and one species of inhibitor molecule. The activator promotes its own production as well as that of a inhibitor, and the inhibitor inhibits the production of the activator.

Figure 2.20: Anthocyanin patterns on petals: From left to right, patterns on a desert willow, a birdeye speedwell, a snapdragon vine, and a palo colorado.

Spatial patterns of coloration due to varying anthocyanin concentrations are observed on many flowers; see Figure 2.20. Ding and colleagues [31] have recently identified activator and inhibitor proteins involved in anthocyanin production. The activator activates both its own production and that of anthocyanin. The authors of Ref. [31] proposed a modified Gierer-Meinhardt model (mGM) for this system and show through numerical simulations that the model can reproduce a range of spatial activator patterns that are similar to spatial anthocyanin patterns observed on petals. These researchers can also modify the inhibitor degradation rate constant, change the observed pattern, and affect the degree to which pollinators are attracted to a flower. This is an amazing accomplishment!

The mGM model proposed by Ding and colleagues only involves the activator and inhibitor; they assume that the anthocyanin concentration is proportional to that of the activator. Their simulations

show highly disordered spot patterns, whereas patterns on plant petals can be stripes or closer to ordered spots on a regular lattice.

In this subsection, we first provide a linear stability analysis of the mGM equations. This allows us to find parameter values close to a Turing instability threshold. If the parameter values are close to the instability threshold, we expect to find, and do find, more ordered patterns. We find, through numerical simulations, both hexagonal lattice and square lattice patterns. Square lattices in a Gierer-Meinhardt-type system are a novel finding of this thesis. We also provide a nonlinear analysis which is valid for parameter values close to threshold and results in a system of ordinary differential equations for the amplitudes of a finite number of Fourier modes that approximate the solution [38]. This allows us to study the competition between stripe patterns and patterns of hexagons or squares. Our analysis parallels work of Song and colleagues [39] for a variation of the Gierer-Meinhardt model that includes saturation.

Next, we propose an extension of the model of Ding and colleagues in [31] to include the activator-induced production of anthocyanin, the anthocyanin scheme discussed above, as well as anthocyanin self association. We assume the production rate to be given by a sigmoidal function of the activator A [40] and very low or no diffusion of anthocyanin between cells. A simple but biologically important observation from numerical simulations of this model is that the degree of association can vary dramatically across the pattern, being very strongly associated where there is a high concentration of anthocyanins, but dominated by the monomer where there is a low anthocyanin concentration.

2.6.1 The Gierer-Meinhardt and modified Gierer-Meinhardt models

The Gierer-Meinhardt model, proposed by its namesakes in 1972 [41], is a well-known activator-inhibitor model. It is a system of two reaction-diffusion equations that has been applied to model a wide range of problems of pattern formation in morphogenesis. The quantities of interest in the model are the activator A and the inhibitor I. The activator is *autocatalytic* in that the production rate of activator increases with A. The inhibitor inhibits the production of activator; the produc-

tion rate of activator decreases with increasing I. The activator has a relatively small diffusion coefficient compared to the inhibitor. (One says that the activator is of 'short range' whereas the inhibitor is of 'long range' [41–43].) The Gierer-Meinhardt model reads

$$\frac{\partial A}{\partial t} = D_A \triangle A + G_A \left(\frac{A^2}{I} + \widetilde{A_0} \right) - U_A A$$
$$\frac{\partial I}{\partial t} = D_I \triangle I + G_I A^2 - U_I I.$$

The operator Δ is two-dimensional Laplacian $\Delta = \frac{\partial^2}{\partial x^2} + \frac{\partial^2}{\partial y^2}$ for the two spatial variables x and y. The parameters D_A and D_I are the diffusion coefficients of A and I, respectively. The assumption that the activator is of short range compared to the inhibitor implies that $D_A << D_I$. The molecules degrade with rate constants U_A and U_I and have background production rates $G_A\widetilde{A_0}$ and $I_0 = 0$, respectively. The term $G_A A^2/I$ models the self-activation of A and inhibition of A by I; the term $G_I A^2$ models the activation of I by A. The activator is self-activated with a potency G_A, whereas the inhibitor is activated by the activator with a potency G_I.

Identifying the activator and inhibitor molecules in flowers of the genus *Mimulus* (monkeyflowers) has been accomplished by Ding and colleagues [31]. The authors show R2R3-MYB to be a molecular activator for itself as well as for anthocyanin production and that R3-MYB inhibits activator production.

The activator-inhibitor model introduced by Ding and colleagues [31] is a modification of the Gierer-Meinhardt model and consists of a system of partial differential equations for the concentrations A of an activator molecule and I of an inhibitor molecule. The reason to add the K in the denominator is to prevent it from becoming zero. Then we can have the inhibitor to be zero as the initial condition. The system reads

$$\frac{\partial A}{\partial t} = D_A \cdot \triangle A + G_A \frac{A^2 + A_0}{I + K} - U_A \cdot A \tag{2.58}$$
$$\frac{\partial I}{\partial t} = D_I \cdot \triangle I + G_I \cdot A^2 + I_0 - U_I \cdot I, \tag{2.59}$$

where D_A and D_I refer to the diffusion coefficients of A and I, respectively. The molecules degrade with rate constants U_A and U_I and have background production rates $A_0 = 0.01$ and $I_0 = 0$, respectively. The term $G_A(A^2 + A_0)/(I + K)$ models the self-activation of A and inhibition of A by I; the term $G_I A^2$ models the activation of I by A. The activator is self-activated with a potency G_A, whereas the inhibitor is activated by the activator with a potency G_I. The residual value $K = 0.001$ in the denominator prevents the denominator from being zero.

Figure 2.21 shows simulations of the system (Eq. 2.58 and Eq. 2.59) based on parameter values measured by Ding and colleagues for wild-type *M. lewisii*. For all numerical simulations in this thesis, we employ a Fourier spectral method with periodic boundary conditions and a fourth-order exponential time differencing Runge-Kutta method for the time stepping as the numerical technique [44, 45] with periodic boundary conditions. The spatial grid is 256×256 unless otherwise noted.

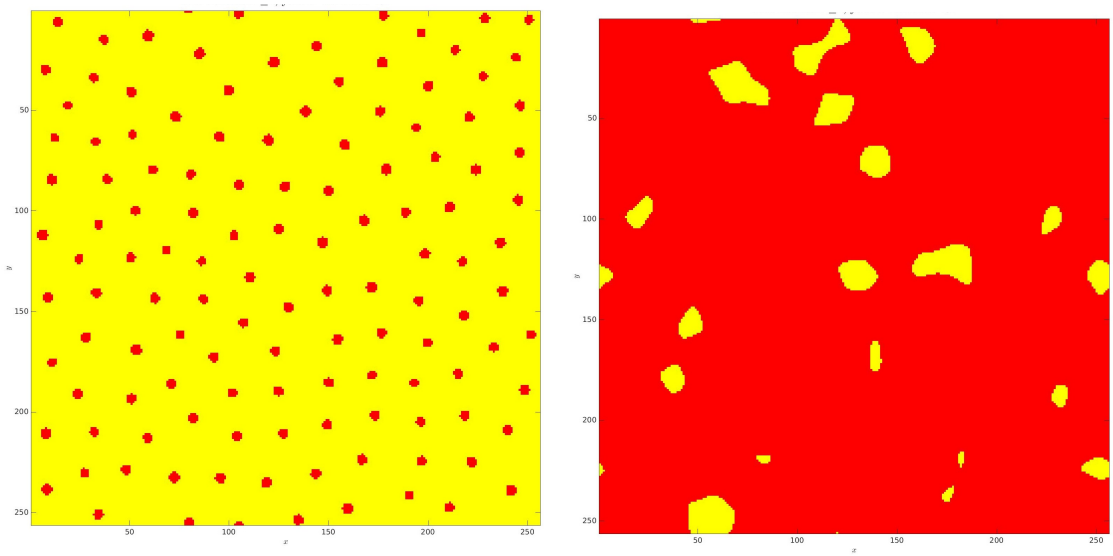

(a) Activator pattern. **(b)** Inhibitor pattern.

Figure 2.21: Spatial concentration patterns of activator and inhibitor at time 10^3 seconds, resulting from simulations of the system given by Eqns.(2.58) and (2.59) with parameter values as follows: The diffusion coefficients are $D_A = 0.01, D_I = 0.5$, the degradation rate constants are $U_A = 0.03$, $U_I = 0.03$, the background production rate constants are $A_0 = 0.01$, $I_0 = 0$, and the activation potency rate constants are $G_A = 0.08$, $G_I = 0.12$. The initial concentration of the activator is $1M$, and that of the inhibitor is $0M$. The spatial domain is $0 \leq x, y \leq 50$. The time step for the simulation was 0.01 seconds, and the spatial step size was $50/256$. The red points represent the concentrations of activator are greater or equal to 3, and yellow means that are less than 3.

As the authors suggest, "subtle changes in simple activator-inhibitor systems are likely essential contributors to the evolution of the remarkable diversity of pigmentation patterns in flowers" [31], and therefore to the diversity of flower-pollinator interactions. Here, we compare the influences of the different parameters. Figure 2.22 shows further examples of patterns resulting from simulations with parameter values equal to those as for Figure 2.21, except for the degradation rate constant U_I for the inhibitor. Increasing U_I increases the degradation of the inhibitor. There will then be less inhibitor to repress the activator, thereby increasing the concentration of the activator. The degradation constant U_I is the parameter that Ding and colleagues modify experimentally to produce a variety of patterns.

Note that in the simulations of Figure 2.21 and Figure 2.22, the pattern is a rather disordered arrangement of dots. Stripe patterns, such as those observed in the second panel of Figure 2.20 are not observed in these simulations, nor are patterns consisting of well-ordered hexagonal lattices as are common in many pattern-forming systems.

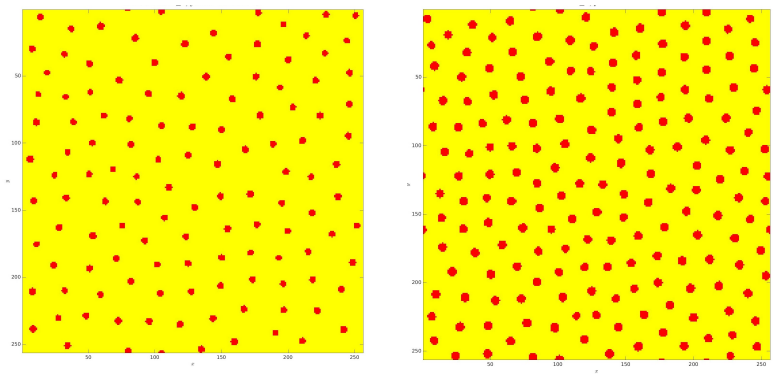

(a) $U_I = 0.03$ **(b)** $U_I = 0.06$

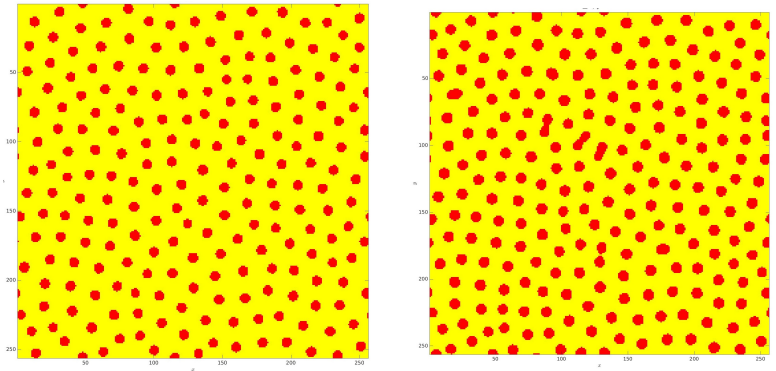

(c) $U_I = 0.09$ **(d)** $U_I = 0.12$

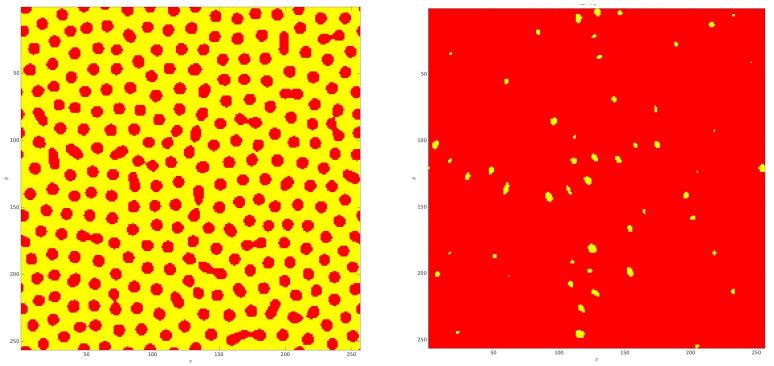

(e) $U_I = 0.15$ **(f)** $U_I = 0.18$

Figure 2.22: Spatial concentration patterns of activator at time 10^3 seconds, resulting from simulations of the system Eq.(2.58) and Eq.(2.59) with parameter values as follows: The diffusion coefficients are $D_A = 0.01, D_I = 0.5$, the degradation rate constants are $U_A = 0.03,\ U_I$ as mentioned below each figure, the background production rate constants are $A_0 = 0.01,\ I_0 = 0$, and the activation potency rate constants are $G_A = 0.08,\ G_I = 0.12$. The initial concentration of the activator is $1M$, and that of the inhibitor is $0M$. The spatial domain is $0 \leq x, y \leq 50$. The time step for the simulation was 0.01 seconds, and the spatial step size was $50/256$. The red points represent the concentrations of activator are greater or equal to 3, and yellow means that are less than 3.

2.6.2 Analysis of the modified Gierer-Meinhardt model

In this section, we first nondimensionalize the mGM equations. We then perform a linear stability analysis of a homogeneous steady-state solution to these nondimensionalized equations. In [31], the authors change the parameter U_I of the system given by Eqns. 2.58 and 2.59 to have different patterns. Therefore, we are particularly interested in this parameter, and thereby focus on a parameter $Q = \frac{U_I}{U_A}$ which we treat as a bifurcation parameter. As Q increases above a critical values Q_T, the homogeneous steady-state solution becomes unstable to periodic disturbances in a Turing instability. We find ordered patterns in numerical simulations and nonlinear analysis of the nondimensionalized mGM equations when Q is close to the critical value Q_T for this Turing instability.

Nondimensionalization and steady-state solutions

The modified Gierer-Meinhardt (mGM) model given by Eqns (2.58) and (2.59) involves three independent variables (two for space and one for time), the two dependent variables A and I, and nine parameters. Rescaling the variables and redefining parameters, we can write the system in terms of nondimensional variables and only four nondimensional parameters. First, we note the dimensions of the variables and parameters in the mGM model: Denoting the dimensions of a variable or parameter ξ by $[\xi]$, and writing and C for 'concentration,' τ for 'time,' and L for 'length,' the dimensions of the original variables and parameters are as follows:

$$[x] = [y] = L;\ [t] = \tau;\ [A] = [I] = C;$$

$$[D_A] = [D_I] = L^2\tau^{-1};$$

$$[G_A] = \tau^{-1};\ [G_I] = C^{-1}\tau^{-1};$$

$$[I_0] = C\tau^{-1};\ [A_0] = C^2;\ [K] = C;$$

$$[U_A] = [U_I] = \tau^{-1}.$$

The rescaled variables

$$u = \frac{G_A}{U_I K} A,\ v = \frac{U_A}{U_I}\left(\frac{I}{K} + 1\right), \tau = U_A t,\ X = \sqrt{\frac{U_A}{D_I}} x,\ Y = \sqrt{\frac{U_A}{D_I}} y, \tag{2.60}$$

and parameters

$$D = \frac{D_A}{D_I},\ P = \frac{G_I}{G_A^2} U_I K,\ Q = \frac{U_I}{U_A},\ u_0 = \frac{A_0 G_A^2}{U_I^2 K^2} \tag{2.61}$$

are therefore dimensionless. In terms of these dimensionless quantities, the mGM models reads

$$\begin{aligned} \frac{\partial u}{\partial \tau} &= D \triangle u + \frac{u^2 + u_0}{v} - u \quad \doteq D \triangle u + f_1(u, v) \\ \frac{\partial v}{\partial \tau} &= \triangle v + P u^2 - Q v + 1 \quad \doteq \triangle v + f_2(u, v). \end{aligned} \tag{2.62}$$

where now $\Delta = \frac{\partial^2}{\partial X^2} + \frac{\partial^2}{\partial Y^2}$. We refer to the system (2.62) as the *dimensionless modified Gierer-Meinhardt model* (dmGM).

Our analysis of the system (2.62) begins by looking for the simplest type of solution: the homogeneous steady-state solution $u \equiv u^*, v \equiv v^*$, where u^* and v^* are constants. The values u^* and v^* satisfy the cubic polynomial system

$$\begin{cases} \dfrac{(u^*)^2 + u_0}{v^*} - u^* = 0 \\ P(u^*)^2 - Q v^* + 1 = 0 \end{cases} \Rightarrow \begin{cases} \dfrac{(u^*)^2 + u_0}{u^*} = v^* \\ P(u^*)^2 - Q\dfrac{(u^*)^2 + u_0}{u^*} + 1 = 0 \end{cases} \tag{2.63}$$

Thus u^* is the solution of $f(s) = Ps^3 - Qs^2 + s - Qu_0 = 0$. That is,

$$\begin{aligned} u^* = \frac{Q}{3P} &- \frac{\sqrt[3]{2}(3P - Q^2)}{3P\sqrt[3]{-9PQ + 2Q^3 + 27P^2Qu_0 + \sqrt{4(3P - Q^2)^3 + (-9PQ + 2Q^3 + 27P^2Qu_0)^2}}} \\ &+ \frac{\sqrt[3]{-9PQ + 2Q^3 + 27P^2Qu_0 + \sqrt{4(3P - Q^2)^3 + (-9PQ + 2Q^3 + 27P^2Qu_0)^2}}}{3\sqrt[3]{2}P}. \end{aligned}$$

Note that $f(0) = -Qu_0 < 0$. Since $f'(s) = 3Ps^2 - 2Qs + 1 = 0$ when $s = \frac{Q \pm \sqrt{Q^2-3P}}{3P}$ and $f(\frac{Q-\sqrt{Q^2-3P}}{3P}) < 0$, we know that $f(s) = 0$ has one and only one real positive root. We will also refer to (u^*, v^*) as the *equilibrium solution*.

Linear stability analysis

The linearization of the system (2.62) at its equilibrium is

$$\begin{pmatrix} \frac{\partial u}{\partial \tau} \\ \\ \frac{\partial v}{\partial \tau} \end{pmatrix} = \mathbf{L} \begin{pmatrix} u \\ \\ v \end{pmatrix}, \tag{2.64}$$

where

$$\mathbf{L} = \begin{pmatrix} \frac{\partial f_1}{\partial u} & \frac{\partial f_1}{\partial v} \\ \frac{\partial f_2}{\partial u} & \frac{\partial f_2}{\partial v} \end{pmatrix} \Bigg|_{(u^*,v^*)} = \begin{pmatrix} \frac{2u^*}{v^*} - 1 & -\frac{(u^*)^2+u_0}{(v^*)^2} \\ 2Pu^* & -Q \end{pmatrix} = \begin{pmatrix} \frac{2u^*}{v^*} - 1 & -\frac{u^*}{v^*} \\ 2Pu^* & -Q \end{pmatrix}, \tag{2.65}$$

because $(u^*)^2 + u_0 = u^*v^*$.

The characteristic polynomial of the matrix $\mathbf{L}$ is

$$p(\lambda) = \lambda^2 - T_0\lambda + J_0, \tag{2.66}$$

where

$$T_0 = \text{Tr}(\mathbf{L}) = \frac{2u^*}{v^*} - 1 - Q, \tag{2.67}$$

and

$$J_0 = \det(\mathbf{L}) = (1 - \frac{2u^*}{v^*})Q + 2P\frac{(u^*)^2}{v^*}. \tag{2.68}$$

The Hopf bifurcation occurs when the real part of the roots in Eq. 2.66 is zero, which is equivalent to $T_0 = 0$. Hence we have that the critical value of the Hopf bifurcation Q_H is approximately equal to 1; see Figure 2.23.

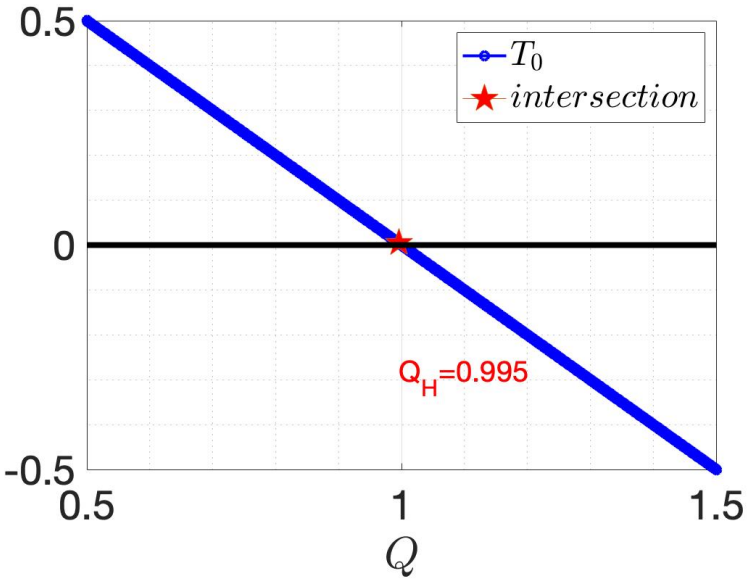

Figure 2.23: The original parameters are $G_A = 0.08, G_I = 0.12, K = 0.001, A_0 = 0.01$, and $U_A = 0.03$. In terms of the nondimensional parameters of Eq. 2.61, we have the coefficients $P = 5.6250 \cdot 10^{-4}Q$, and $u_0 = \frac{71111}{Q^2}$. Using the relations in Eq. 2.60, we can have T_0 curve when varying the value of Q. The curve T_0 curve is graphed in blue. The critical value Q_H for a Hopf bifurcation is marked in red.

To analyze the stability of the uniform state under nonuniform perturbations, we seek solutions of the form

$$\begin{pmatrix} u \\ v \end{pmatrix} = \begin{pmatrix} u^* \\ v^* \end{pmatrix} + \epsilon \begin{pmatrix} u_k \\ v_k \end{pmatrix} \exp(i\mathbf{k} \cdot \mathbf{x} + \lambda t) + c.c + o(\epsilon^2), \tag{2.69}$$

where 'c.c.' is the complex conjugate of $\exp(i\mathbf{k} \cdot \mathbf{x} + \lambda t)$. Substituting Eq. 2.69 into

$$\begin{pmatrix} \frac{\partial u}{\partial \tau} \\ \frac{\partial v}{\partial \tau} \end{pmatrix} = \mathbf{L} \begin{pmatrix} u \\ v \end{pmatrix} + \begin{pmatrix} D \triangle u \\ \triangle v \end{pmatrix}, \tag{2.70}$$

we have the dispersion relation being the function of eigenvalue λ at the wave number $k = |\mathbf{k}|$:

$$p_k(\lambda) = \lambda^2 - T_k\lambda + J_k = 0, \tag{2.71}$$

where

$$T_k = -(D+1)k^2 + T_0, \tag{2.72}$$

$$J_k = Dk^4 + \left(DQ - \frac{2u^*}{v^*} + 1\right)k^2 + J_0. \tag{2.73}$$

The characteristic values of 2.71 are

$$\lambda_{k_\pm} = \frac{T_k \pm \sqrt{T_k^2 - 4J_k}}{2}. \tag{2.74}$$

If $J_k \geq 0$, we either have $T_k^2 - 4J_k \geq 0$ or $T_k^2 - 4J_k < 0$. For the case $T_k^2 - 4J_k \geq 0$, $\lambda_{k_\pm}$ are both real, and the sign of $\text{Re}(\lambda_{k_\pm})$ depends on the sign of T_k. When $T_k^2 - 4J_k < 0$, we have $2\text{Re}(\lambda_{k_\pm}) = T_k$, which means the stability also depends on the sign of T_k.

Suppose $J_k < 0$, we then have $T_k^2 - 4J_k > T_k^2 > 0$, which implies

$$2\lambda_{k_+} = \underbrace{T_k}_{\text{smaller}} + \underbrace{\sqrt{T_k^2 - 4J_k}}_{\text{larger, positive}} > 0.$$

This shows that the system is unstable. Hence the unstable term appears when (a) $T_k > 0$ and $J_k \geq 0$, or (b) $J_k < 0$. The Turing bifurcation occurs when $J_k = 0$ at $k = k_T$. We can rewrite J_k as

$$\begin{aligned} J_k &= Dk^4 + \left(DQ - \frac{2u^*}{v^*} + 1\right)k^2 + J_0 \\ &= D\left(k^4 + \frac{DQ - \frac{2u^*}{v^*} + 1}{D}k^2 + (\frac{DQ - \frac{2u^*}{v^*} + 1}{2D})^2\right) + J_0 - \frac{\left(DQ - \frac{2u^*}{v^*} + 1\right)^2}{4D}. \end{aligned} \tag{2.75}$$

When $J_0 = \frac{\left(DQ - \frac{2u^*}{v^*} + 1\right)^2}{4D}$, $J_k = 0$ at

$$k^2 = k_T^2 = -\frac{DQ - \frac{2u^*}{v^*} + 1}{2D} = \frac{\sqrt{4DJ_0}}{2D} = \sqrt{\frac{J_0}{D}}. \tag{2.76}$$

Then the critical value of Q is the solution of

$$4DJ_0 = \left(DQ - \frac{2u^*}{v^*} + 1\right)^2. \tag{2.77}$$

It is clear that the Turing bifurcation Q_T is dependent on the parameter D, which equals $\frac{D_A}{D_I}$. Hence, when we fix the original parameters are $G_A = 0.08, G_I = 0.12, K = 0.001, A_0 = 0.01$, and $U_A = 0.03$. In terms of the nondimensional parameters of Eq. 2.61, we have the coefficients $P = 5.6250 \times 10^{-4}Q, u_0 = \frac{71111}{Q^2}$, a Turing bifurcation Q_T will be different if we pick different values of $D = \frac{D_A}{D_I}$. For $D = 0.02$, then the Turing bifurcation $Q_T \approx 8.58$, and the corresponding critical wave number $k_T \approx 4.55$. We can do the similar approximation for $D = 0.1$, and then $Q_T \approx 1.7$, $k_T \approx 2$. Numerically, Eq. 2.76 and Eq. 2.77 can be solved and we can find the exactly values of Q_T and k_T; see Figure 2.25 and Figure 2.24.

Figure 2.24b and Figure 2.25b show that when $Q < Q_T$, we will have a narrow band of unstable wavelengths.

Nonlinear analysis of the Turing instability: Amplitude equations

We now analyze the system given by Eq. 2.62 for parameter values that yield a Turing bifurcation [46]. We assume the bifurcation parameter Q to be slightly below the critical value Q_T. As discussed in the previous section, there is then a narrow band of unstable wave numbers about k_T (that is, an annulus in the two-dimensional space of wave vectors) for which the corresponding Fourier modes have a positive linear growth rate. The following analysis yields nonlinear ordinary differential equations for the evolution of the amplitudes of these unstable modes [38, 47, 48].

The nonlinear analysis will aim to understand solutions that are approximately sums of a small number of Fourier modes. Numerical simulations of the modified Gierer-Meinhardt model, shown

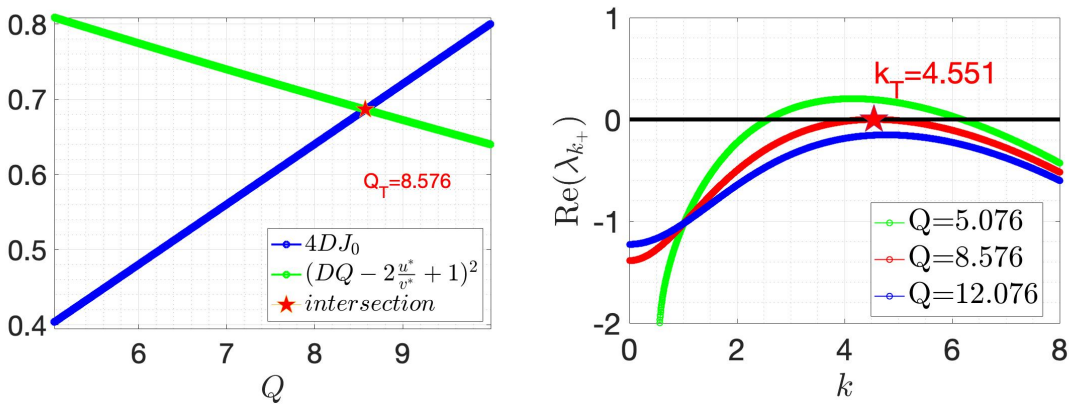

(a) $Q_T = 8.576$ **(b)** $k_T = 4.551$

Figure 2.24: The original parameters are $G_A = 0.08, G_I = 0.12, K = 0.001, A_0 = 0.01, U_A = 0.03, D_A = 0.01$, and $D_I = 0.5$. In terms of the nondimensional parameters of Eq. 2.61, we have the coefficients $P = 5.6250 \cdot 10^{-4}Q, u_0 = \frac{71111}{Q^2}$, and $D = 0.02$. Using the relations in Eq. 2.77 and Eq. 2.76, we can have Q_T and k_T values.
(b) The real part of λ_{k_+} for different value of Q. Green curve: $Q \approx 5$, red curve: $Q = Q_T = 8.576$, and blue curve: $Q \approx 12$.

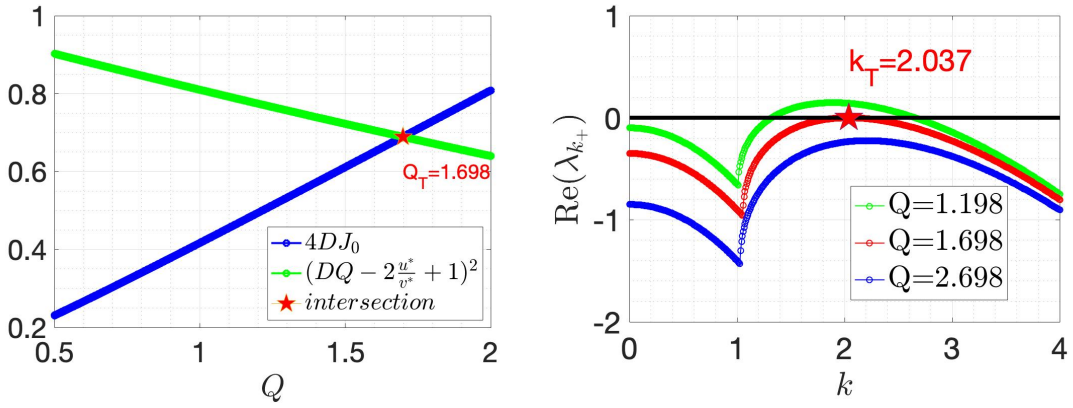

(a) $Q_T = 0.1651$ **(b)** $k_T = 2.023$

Figure 2.25: The original parameters are $G_A = 0.08, G_I = 0.12, K = 0.001, A_0 = 0.01, U_A = 0.03, D_A = 0.05$, and $D_I = 0.5$. In terms of the nondimensional parameters of Eq. 2.61, we have the coefficients $P = 5.6250 \cdot 10^{-4}Q, u_0 = \frac{71111}{Q^2}$, and $D = 0.1$. Using the relations in Eq. 2.77 and Eq. 2.76, we can have Q_T and k_T values.
(b) The real part of λ_{k_+} for different value of Q. Green curve: $Q = 1.165$, red curve: $Q = Q_T = 1.651$, and blue curve: $Q = 2.651$.

in Fig. 2.26, provide us with motivation for the form of the approximate nonlinear solutions that may arise from this model. A *roll pattern* (Fig. 2.26 (a)) is approximately given by one Fourier mode;

$$\begin{pmatrix} u \\ v \end{pmatrix} \simeq \begin{pmatrix} A(t) \\ B(t) \end{pmatrix} \mathrm{e}^{i\vec{k}\cdot\vec{x}} \; + \; \text{c.c.},$$

where 'c.c.' is the complex conjugate of the previous term. A *hexagonal pattern* (Fig. 2.26 (b)) is approximately given by the sum of three Fourier modes,

$$\begin{pmatrix} u \\ v \end{pmatrix} \simeq \sum_{j=1}^{3} \begin{pmatrix} A_j(t) \\ B_j(t) \end{pmatrix} \mathrm{e}^{i\vec{k}_j\cdot\vec{x}} \; + \; \text{c.c.},$$

where the wavevectors $\vec{k}_j$ obey the relation $\vec{k}_1 + \vec{k}_2 + \vec{k}_3 = \vec{0}$ and $|\vec{k}_1| = |\vec{k}_2| = |\vec{k}_3|$ [49]. A *square pattern* (Fig. 2.26 (c)) is approximately given by the sum of two Fourier modes, approximately given by the sum of two Fourier modes,

$$\begin{pmatrix} u \\ v \end{pmatrix} \simeq \sum_{j=1}^{2} \begin{pmatrix} A_j(t) \\ B_j(t) \end{pmatrix} \mathrm{e}^{i\vec{k}_j\cdot\vec{x}} \; + \; \text{c.c.},$$

where the wavevectors $\vec{k}_j$ are orthogonal and of equal length. Similar patterns of rolls and hexagons have been observed in a wide array of laboratory experiments and natural systems. A few of the many examples include Rayleigh-Bénard convection [50] in which convection rolls appear in a container of fluid that is heated from below, nanoscale surface structures formed by bombarding a solid with a broad ion beam [51–53], and the Rosenzweig instability in magnetically excited ferrofluids [54].

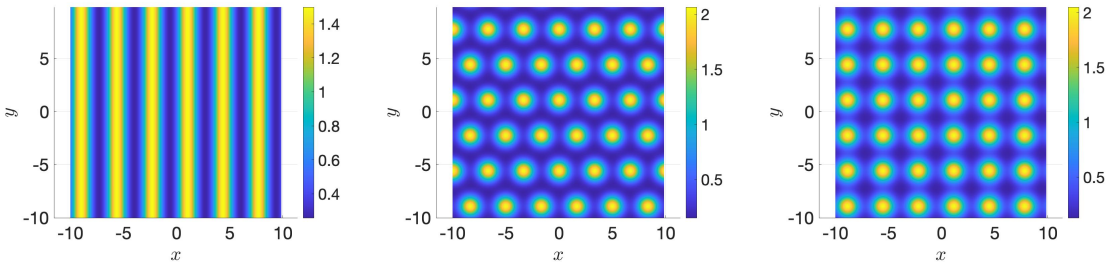

(a) Roll patterns **(b)** Hexagon patterns **(c)** Square patterns

Figure 2.26: Solutions $u(x, y, t = 3000)$ of the modified Gierer-Meinhardt model: The original parameters are $G_A = 0.08, G_I = 0.12, K = 0.001, A_0 = 0.01, U_A = 0.03, D_A = 0.05$, and $D_I = 0.5$. In terms of the nondimensional parameters of Eq. 2.61, we have the coefficients $P = 5.6250 \cdot 10^{-4} Q, u_0 = \frac{71111}{Q^2}$, and $D = 0.1$. We could have different kinds of patterns when we choose the parameter Q close to the critical value Q_T. (a) $Q_T - Q = 8\% \times Q_T$. (b) $Q_T - Q = 4\% \times Q_T$. (c) $Q_T - Q = 3\% \times Q_T$.

Roll-Hexagon competition

To analyze the competition between roll patterns and hexagon patterns, we begin by rewriting the system in Eq. 2.62 at the steady state $((u^*)_T, (v^*)_T)$ as

$$\begin{aligned} \frac{\partial}{\partial \tau}\begin{pmatrix} u \\ v \end{pmatrix} &= \mathscr{L}\begin{pmatrix} u \\ v \end{pmatrix} + \mathscr{N}(u, v) \\ &= \begin{pmatrix} D\triangle + \frac{2u^*}{v^*} - 1 & -\frac{u^*}{v^*} \\ 2Pu^* & \triangle - Q \end{pmatrix}\begin{pmatrix} u \\ v \end{pmatrix} \\ &+ \begin{pmatrix} \frac{1}{v^*}u^2 - 2\frac{u^*}{(v^*)^2}uv + \frac{(u^*)^2+u_0}{(v^*)^3}v^2 - \frac{1}{(v^*)^2}u^2v + \frac{2u^*}{(v^*)^3}uv^2 - \frac{(u^*)^2+u_0}{(v^*)^4}v^3 \\ Pu^2 \end{pmatrix}, \end{aligned} \tag{2.78}$$

where $\mathscr{L}$ is a linear operator and $\mathscr{N}$ is a nonlinear operator. We consider the bifurcation parameter Q to be slightly below the critical value Q_T; that is, we set

$$Q = Q_T - \epsilon Q_1 - \epsilon^2 Q_2 + \cdots, \tag{2.79}$$

where $\epsilon > 0$ is small and $Q_1 > 0$ and $Q_2 > 0$ are of order 1. In Figure 2.24b and Figure 2.25b, there is an interval around k_T in which $\mathrm{Re}(\lambda_{k_+}) > 0$. We can also decompose the linear operator

$\mathscr{L}$ into

$$\mathscr{L} = \mathscr{L}_T + (Q_T - Q)\mathscr{M},$$

where

$$\mathscr{L}_T = \begin{pmatrix} D\triangle + \frac{2(u^*)_T}{(v^*)_T} - 1 & -\frac{(u^*)_T}{(v^*)_T} \\ 2P(u^*)_T & \triangle - Q_T \end{pmatrix}.$$

Because $2P(u^*) \approx 2Q$ by $u^* \approx v^* \approx \frac{Q}{P}$, we have

$$\begin{aligned} \mathscr{M} &= \frac{1}{Q_T - Q}(\mathscr{L} - \mathscr{L}_T) = \frac{1}{Q_T - Q}\begin{pmatrix} \frac{2u^*}{v^*} - \frac{2(u^*)_T}{(v^*)_T} & -\frac{u^*}{v^*} + \frac{(u^*)_T}{(v^*)_T} \\ 2Pu^* - 2P(u^*)_T & -Q + Q_T \end{pmatrix} \\ &\approx \frac{1}{Q_T - Q}\begin{pmatrix} 0 & 0 \\ 2Q - 2Q_T & -Q + Q_T \end{pmatrix} = \begin{pmatrix} 0 & 0 \\ -2 & 1 \end{pmatrix}. \end{aligned}$$

We expand u and v in powers of ϵ and write

$$\begin{pmatrix} u \\ v \end{pmatrix} = \begin{pmatrix} (u^*)_T \\ (v^*)_T \end{pmatrix} + \epsilon \begin{pmatrix} u_1 \\ v_1 \end{pmatrix} + \epsilon^2 \begin{pmatrix} u_2 \\ v_2 \end{pmatrix} + \cdots . \tag{2.80}$$

We expect that the amplitudes of the unstable modes will evolve slowly in time because the linear growth rate Reλ_+ is of order ϵ. Here, we need the multiple time scales $t_n = \epsilon^n \tau$ for $n = 0, 1, 2, \cdots$, which can be regarded as independent variables. Then we can write

$$\frac{\partial}{\partial \tau} = \frac{\partial}{\partial t_0} + \epsilon \frac{\partial}{\partial t_1} + \epsilon^2 \frac{\partial}{\partial t_2} + \cdots . \tag{2.81}$$

At order ϵ, the linear system of equations reads

$$\mathscr{L}_T \begin{pmatrix} u_1 \\ v_1 \end{pmatrix} = \begin{pmatrix} 0 \\ 0 \end{pmatrix}. \tag{2.82}$$

This system has solutions of the form

$$\begin{pmatrix} u_1 \\ v_1 \end{pmatrix} = \sum_{\vec{k}_j \in \mathcal{C}} \begin{pmatrix} \frac{DQ_T + \frac{2(u^*)_T}{(v^*)_T} - 1}{4PD(u^*)_T} \\ 1 \end{pmatrix} (V_j e^{i\mathbf{k}_j \cdot \mathbf{x}} + c.c.), \tag{2.83}$$

where $\mathcal{C}$ is the circle of wave vectors of magnitute k_T, the complex-valued amplitudes V_j depend on the slow time t_1 but not on t_0, and c.c. denotes the complex conjugate. Later, we will restrict this infinite sum to a finite sum of wavevectors that interact via the nonlinear terms and allow for the study of competition between roll and hexagon planforms, namely

$$\begin{pmatrix} u_1 \\ v_1 \end{pmatrix} = \sum_{j=1}^{3} \begin{pmatrix} \frac{DQ_T + \frac{2(u^*)_T}{(v^*)_T} - 1}{4PD(u^*)_T} \\ 1 \end{pmatrix} (V_j e^{i\mathbf{k}_j \cdot \mathbf{x}} + c.c.), \tag{2.84}$$

where $\mathbf{k}_1 + \mathbf{k}_2 + \mathbf{k}_3 = 0$, and $\mathbf{k}_j \in \mathcal{C}$ for $j = 1, 2, 3$.

Equations for the time evolution of the amplitudes V_j arise as solvability conditions for the correction term at order ϵ^2. The system of equations obtained at order ϵ^2 is

$$\mathscr{L}_T \begin{pmatrix} u_2 \\ v_2 \end{pmatrix} = \frac{\partial}{\partial t_1} \begin{pmatrix} u_1 \\ v_1 \end{pmatrix} - Q_1 \mathscr{M} \begin{pmatrix} u_1 \\ v_1 \end{pmatrix} - \begin{pmatrix} \frac{1}{v^*} u_1^2 - 2\frac{u^*}{(v^*)^2} u_1 v_1 + \frac{(u^*)^2 + u_0}{(v^*)^3} v_1^2 \\ P u_1^2 \end{pmatrix} \doteq \begin{pmatrix} F_u \\ F_v \end{pmatrix}. \tag{2.85}$$

The operator $\mathscr{L}_T$ is not invertible since it has the eigenvector $(u_1, v_1)^T$ of eigenvalue 0. According to the Fredholm Alternative (see Refs. [38, 55]), Eq. 2.85 has a solution if and only if $(F_u, F_v)^T$ is

orthogonal to the kernel of the adjoint operator $\mathscr{L}_T^\dagger$. The zero eigenvector of $\mathscr{L}_T^\dagger$ is

$$\begin{pmatrix} 1 \\ -\frac{DQ_T+\frac{2(u^*)_T}{(v^*)_T}-1}{4P(u^*)_T} \end{pmatrix} (e^{i\mathbf{k}_T\cdot\mathbf{x}} + c.c.), \tag{2.86}$$

where $\mathbf{k}_T \in \mathcal{C}$. The definition of the inner product $\langle \boldsymbol{a}|\boldsymbol{b}\rangle$ of $\boldsymbol{a} = (a_x, a_y)^T \mathrm{e}^{i\boldsymbol{k}\cdot\boldsymbol{x}}$ and $\boldsymbol{b} = (b_x, b_y)^T \mathrm{e}^{i\boldsymbol{q}\cdot\boldsymbol{x}}$ is the average of $\boldsymbol{a}^* \cdot \boldsymbol{b}$ over the region $\mathcal{R} \equiv [0, 2\pi/k_T] \times [0, 2\pi/k_T]$ in wavevector space. Denoting the area of $\mathcal{R}$ by $|\mathcal{R}|$, we have

$$\langle \boldsymbol{a}|\boldsymbol{b}\rangle = \frac{1}{|\mathcal{R}|}\int_{\mathcal{R}} \left[(a_x, a_y)\mathrm{e}^{-i\boldsymbol{k}\cdot\boldsymbol{x}} \begin{pmatrix} b_x \\ b_y \end{pmatrix} \mathrm{e}^{i\boldsymbol{q}\cdot\boldsymbol{x}} \right] \mathrm{d}x\mathrm{d}y = \frac{1}{|\mathcal{R}|}\int_{\mathcal{R}} (a_x b_x + a_y b_y)\mathrm{e}^{i(\boldsymbol{q}-\boldsymbol{k})\cdot\boldsymbol{x}}\mathrm{d}x\mathrm{d}y$$

$$= \begin{cases} a_x b_x + a_y b_y & \text{if } \boldsymbol{k} = \boldsymbol{q}; \\ 0 & otherwise. \end{cases}$$

Denote $\frac{DQ_T+\frac{2(u^*)_T}{(v^*)_T}-1}{4PD(u^*)_T}$ by Y, and let F_u^j, F_v^j represent the coefficients corresponding to $e^{i\mathbf{k}_j\cdot\mathbf{x}}$. Then, from Eq. 2.85, we have, for $j, p, q \in [1, 2, 3]$ and $j \neq p \neq q$,

$$\begin{aligned} \begin{pmatrix} F_u^j \\ F_v^j \end{pmatrix} = &\begin{pmatrix} Y\frac{\partial}{\partial t_1}V_j \\ \frac{\partial}{\partial t_1}V_j \end{pmatrix} - Q_1 \begin{pmatrix} 0 \\ (-2Y+1)V_j \end{pmatrix} \\ &- \begin{pmatrix} \frac{1}{v^*}Y^2(2\overline{V_pV_q}) - 2\frac{u^*}{(v^*)^2}Y(2\overline{V_pV_q}) + \frac{(u^*)^2+u_0}{(v^*)^3}(2\overline{V_pV_q}) \\ PY^2(2\overline{V_pV_q}) \end{pmatrix}. \end{aligned} \tag{2.87}$$

Since

$$(1, -DY) \begin{pmatrix} F_u^j \\ F_v^j \end{pmatrix} = 0, \text{ for } j \in [1, 2, 3] \tag{2.88}$$

we have, for $j, p, q \in [1, 2, 3]$ and $j \neq p \neq q$,

$$\begin{aligned} Y(1-D)\frac{\partial}{\partial t_1}V_j = &- DY(-2Y+1)Q_1V_j \\ &+ \left(2(\frac{1}{v^*}Y^2 - 2\frac{u^*}{(v^*)^2}Y + \frac{(u^*)^2+u_0}{(v^*)^3}) - 2PDY^3\right)\overline{V_pV_q}. \end{aligned} \tag{2.89}$$

We now proceed to order ϵ^2 and write

$$\begin{aligned} \begin{pmatrix} u_2 \\ v_2 \end{pmatrix} = &\begin{pmatrix} U_0 \\ V_0 \end{pmatrix} + \sum_{j=1}^{3}\begin{pmatrix} \widetilde{U_j} \\ \widetilde{V_j} \end{pmatrix}\exp(i\mathbf{k}_j\cdot\mathbf{x}) + \sum_{j=1}^{3}\begin{pmatrix} UU_j \\ VV_j \end{pmatrix}\exp(2i\mathbf{k}_j\cdot\mathbf{x}) \\ &+ \begin{pmatrix} UU_{12} \\ VV_{12} \end{pmatrix}\exp(i(\mathbf{k}_1-\mathbf{k}_2)\cdot\mathbf{x}) + \begin{pmatrix} UU_{23} \\ VV_{23} \end{pmatrix}\exp(i(\mathbf{k}_2-\mathbf{k}_3)\cdot\mathbf{x}) \\ &+ \begin{pmatrix} UU_{31} \\ VV_{31} \end{pmatrix}\exp(i(\mathbf{k}_3-\mathbf{k}_1)\cdot\mathbf{x}) + c.c. \end{aligned} \tag{2.90}$$

Then,

$$\mathscr{L}_T \begin{pmatrix} u_2 \\ v_2 \end{pmatrix} = \begin{pmatrix} \frac{2(u^*)_T}{(v^*)_T} - 1 & -\frac{(u^*)_T}{(v^*)_T} \\ 2P(u^*)_T & -Q_T \end{pmatrix} \begin{pmatrix} U_0 \\ V_0 \end{pmatrix}$$
$$+ \sum_{j=1}^{3} \begin{pmatrix} -Dk^2 + \frac{2(u^*)_T}{(v^*)_T} - 1 & -\frac{(u^*)_T}{(v^*)_T} \\ 2P(u^*)_T & -k^2 - Q_T \end{pmatrix} \begin{pmatrix} \widetilde{U_j} \\ \widetilde{V_j} \end{pmatrix} \exp(i\mathbf{k}_j \cdot \mathbf{x})$$
$$+ \sum_{j=1}^{3} \begin{pmatrix} -4Dk^2 + \frac{2(u^*)_T}{(v^*)_T} - 1 & -\frac{(u^*)_T}{(v^*)_T} \\ 2P(u^*)_T & -4k^2 - Q_T \end{pmatrix} \begin{pmatrix} UU_j \\ VV_j \end{pmatrix} \exp(2i\mathbf{k}_j \cdot \mathbf{x})$$
$$+ \begin{pmatrix} -3Dk^2 + \frac{2(u^*)_T}{(v^*)_T} - 1 & -\frac{(u^*)_T}{(v^*)_T} \\ 2P(u^*)_T & -3k^2 - Q_T \end{pmatrix} \begin{pmatrix} UU_{12} \\ VV_{12} \end{pmatrix} \exp(i(\mathbf{k}_1 - \mathbf{k}_2) \cdot \mathbf{x})$$
$$+ \begin{pmatrix} -3Dk^2 + \frac{2(u^*)_T}{(v^*)_T} - 1 & -\frac{(u^*)_T}{(v^*)_T} \\ 2P(u^*)_T & -3k^2 - Q_T \end{pmatrix} \begin{pmatrix} UU_{23} \\ VV_{23} \end{pmatrix} \exp(i(\mathbf{k}_2 - \mathbf{k}_3) \cdot \mathbf{x})$$
$$+ \begin{pmatrix} -3Dk^2 + \frac{2(u^*)_T}{(v^*)_T} - 1 & -\frac{(u^*)_T}{(v^*)_T} \\ 2P(u^*)_T & -3k^2 - Q_T \end{pmatrix} \begin{pmatrix} UU_{31} \\ VV_{31} \end{pmatrix} \exp(i(\mathbf{k}_3 - \mathbf{k}_1) \cdot \mathbf{x}) + c.c., \tag{2.91}$$

because $|\mathbf{k}_1 - \mathbf{k}_2| = \sqrt{3}k$ if $|\mathbf{k}_1| = |\mathbf{k}_2| = k$.

The first element of the third term of the right hand side of Eq. 2.85 is

$$-\left(\frac{Y^2}{v^*} - 2\frac{Yu^*}{(v^*)^2} + \frac{(u^*)^2 + u_0}{(v^*)^3}\right)\left(\sum_{j=1}^{3} V_j^2 \exp(2i\mathbf{k}_j \cdot \mathbf{x}) + 2\sum_{j=1}^{3} V_j\overline{V_j}\right. \tag{2.92}$$
$$\left. +2 \sum_{j\neq\tilde{j}\in[1,2,3]} V_j V_{\tilde{j}} \exp(i(\mathbf{k}_j + \mathbf{k}_{\tilde{j}}) \cdot \mathbf{x}) + 2 \sum_{j\neq\tilde{j}\in[1,2,3]} V_j\overline{V_{\tilde{j}}} \exp(i(\mathbf{k}_j - \mathbf{k}_{\tilde{j}}) \cdot \mathbf{x}) + c.c.\right).$$

We can write $V_j\overline{V_j} = |V_j|^2$, and $\mathbf{k}_1 + \mathbf{k}_2 = -\mathbf{k}_3, \mathbf{k}_2 + \mathbf{k}_3 = -\mathbf{k}_1, \mathbf{k}_3 + \mathbf{k}_1 = -\mathbf{k}_2$. Then the second element is

$$-PY^2 \left(\sum_{j=1}^{3} V_j^2 \text{exp}(2i\mathbf{k}_j \cdot \mathbf{x}) + 2\sum_{j=1}^{3} |V_j|^2 + 2 \sum_{j\neq p\neq q\in[1,2,3]} V_j V_p \text{exp}(i(-\mathbf{k}_q) \cdot \mathbf{x}) \right. \tag{2.93}$$
$$\left. +2 \sum_{j\neq\tilde{j}\in[1,2,3]} V_j \overline{V_{\tilde{j}}} \text{exp}(i(\mathbf{k}_j - \mathbf{k}_{\tilde{j}}) \cdot \mathbf{x}) + c.c. \right).$$

Solving Eq. 2.85, we have

$$\begin{pmatrix} U_0 \\ V_0 \end{pmatrix} = \begin{pmatrix} \frac{2(u^*)_T}{(v^*)_T} - 1 & -\frac{(u^*)_T}{(v^*)_T} \\ 2P(u^*)_T & -Q_T \end{pmatrix}^{-1} \begin{pmatrix} -2\left(\frac{Y^2}{v^*} - 2\frac{Yu^*}{(v^*)^2} + \frac{(u^*)^2+u_0}{(v^*)^3}\right) \\ -2PY^2 \end{pmatrix} (|V_1|^2 + |V_2|^2 + |V_3|^2) \tag{2.94}$$
$$\doteq \begin{pmatrix} \widetilde{u_0} \\ \widetilde{v_0} \end{pmatrix} (|V_1|^2 + |V_2|^2 + |V_3|^2),$$

$$\begin{pmatrix} UU_j \\ VV_j \end{pmatrix} = \begin{pmatrix} -4Dk^2 + \frac{2(u^*)_T}{(v^*)_T} - 1 & -\frac{(u^*)_T}{(v^*)_T} \\ 2P(u^*)_T & -4k^2 - Q_T \end{pmatrix}^{-1} \begin{pmatrix} -\left(\frac{Y^2}{v^*} - 2\frac{Yu^*}{(v^*)^2} + \frac{(u^*)^2+u_0}{(v^*)^3}\right) \\ -PY^2 \end{pmatrix} V_j^2 \tag{2.95}$$
$$\doteq \begin{pmatrix} \widetilde{uu} \\ \widetilde{vv} \end{pmatrix} V_j^2,$$

$$\begin{pmatrix} UU_{j\tilde{j}} \\ VV_{j\tilde{j}} \end{pmatrix} = \begin{pmatrix} -3Dk^2 + \frac{2(u^*)_T}{(v^*)_T} - 1 & -\frac{(u^*)_T}{(v^*)_T} \\ 2P(u^*)_T & -3k^2 - Q_T \end{pmatrix}^{-1} \begin{pmatrix} -2\left(\frac{Y^2}{v^*} - 2\frac{Yu^*}{(v^*)^2} + \frac{(u^*)^2+u_0}{(v^*)^3}\right) \\ -2PY^2 \end{pmatrix} V_j \overline{V_{\tilde{j}}} \tag{2.96}$$

$$\doteq \begin{pmatrix} \widetilde{uu_{\neq}} \\ \widetilde{vv_{\neq}} \end{pmatrix} V_j \overline{V_{\tilde{j}}}.$$

Also, we have $\widetilde{U_j} = Y\widetilde{V_j}$. Denote $\widetilde{V_j}$ by W_j.

At order ϵ^3, we have

$$\begin{aligned} \mathscr{L}_T \begin{pmatrix} u_3 \\ v_3 \end{pmatrix} &\doteq \begin{pmatrix} H_u \\ H_v \end{pmatrix} \\ &= \frac{\partial}{\partial t_1}\begin{pmatrix} u_2 \\ v_2 \end{pmatrix} + \frac{\partial}{\partial t_2}\begin{pmatrix} u_1 \\ v_1 \end{pmatrix} - Q_1\mathscr{M}\begin{pmatrix} u_2 \\ v_2 \end{pmatrix} - Q_2\mathscr{M}\begin{pmatrix} u_1 \\ v_1 \end{pmatrix} - \begin{pmatrix} N_3(u,v) \\ 2Pu_1u_2 \end{pmatrix}, \end{aligned} \tag{2.97}$$

where

$$\begin{aligned} N_3(u,v) =& \frac{1}{v^*}2u_1u_2 - \frac{2u^*}{(v^*)^2}(u_1v_2 + u_2v_1) + \frac{(u^*)^2 + u_0}{(v^*)^3}2v_1v_2 \\ &- \frac{1}{(v^*)^2}u_1^2v_1 + \frac{2u^*}{(v^*)^3}u_1v_1^2 - \frac{(u^*)^2 + u_0}{(v^*)^4}v_1^3. \end{aligned}$$

Again, according to the Fredholm Alternative, Eq. 2.97 has a solution if and only if

$$(1, -DY)\begin{pmatrix} H_u^j \\ H_v^j \end{pmatrix} = 0, \text{ for } j \in [1,2,3], \tag{2.98}$$

where we denote H_u^j, H_v^j to represent the coefficients corresponding to $e^{i\mathbf{k}_j\cdot\mathbf{x}}$.

Expanding $(H_u^j, H_v^j)^T$ as

$$\begin{pmatrix} H_u^j \\ H_v^j \end{pmatrix} = \begin{pmatrix} Y\left(\frac{\partial}{\partial t_1}W_j + \frac{\partial}{\partial t_2}V_j\right) \\ \frac{\partial}{\partial t_1}W_j + \frac{\partial}{\partial t_2}V_j \end{pmatrix} - \begin{pmatrix} 0 \\ (-2Y+1)\left(Q_1 W_j + Q_2 V_j\right) \end{pmatrix} + \begin{pmatrix} NH_u^j \\ -2P\overbrace{u_1 u_2}^{}_{j} \end{pmatrix}, \tag{2.99}$$

where $\overbrace{ab}^{}_{j}$ is the coefficient corresponding to $e^{i\mathbf{k}_j\cdot\mathbf{x}}$ in ab, and

$$\begin{aligned} NH_u^j = &-\frac{2}{v^*}\overbrace{u_1 u_2}^{}_{j} + \frac{2u^*}{(v^*)^2}(\overbrace{u_1 v_2}^{}_{j} + \overbrace{u_2 u_1}^{}_{j}) - 2\frac{(u^*)^2 + A_0}{(v^*)^3}\overbrace{v_1 v_2}^{}_{j} \\ &+ \frac{1}{(v^*)^2}\overbrace{u_1^2 v_1}^{}_{j} - \frac{2u^*}{(v^*)^3}\overbrace{u_1 v_1^2}^{}_{j} + \frac{(u^*)^2 + A_0}{(v^*)^4}\overbrace{v_1^3}^{}_{j}. \end{aligned}$$

For $j, p, q \in [1,2,3]$ and $j \neq p \neq q$, the expansions for the terms $\overbrace{ab}^{}_{j}$ are

$$\begin{aligned} \overbrace{u_1 u_2}^{}_{j} &= YV_j\widetilde{u_0}(|V_j|^2 + |V_p|^2 + |V_q|^2) + Y\overline{V_p}Y\overline{W_q} + Y\overline{V_q}Y\overline{W_p} + Y\overline{V_j}\widetilde{uu}V_j^2 \\ &\quad + YV_p\widetilde{uu_{\neq}}V_j\overline{V_p} + YV_q\widetilde{uu_{\neq}}V_j\overline{V_q} \\ &= Y\left[(\widetilde{u_0} + \widetilde{uu})|V_j|^2 + (\widetilde{u_0} + \widetilde{uu_{\neq}})(|V_p|^2 + |V_q|^2)\right]V_j + Y^2\left(\overline{V_pW_q} + \overline{V_qW_p}\right), \end{aligned} \tag{2.100}$$

$$\overbrace{u_1 v_2}^{}_{j} = Y\left[(\widetilde{v_0} + \widetilde{vv})|V_j|^2 + (\widetilde{v_0} + \widetilde{vv_{\neq}})(|V_p|^2 + |V_q|^2)\right]V_j + Y\left(\overline{V_pW_q} + \overline{V_qW_p}\right), \tag{2.101}$$

$$\overbrace{v_1 u_2}^{}_{j} = \left[(\widetilde{u_0} + \widetilde{uu})|V_j|^2 + (\widetilde{u_0} + \widetilde{uu_{\neq}})(|V_p|^2 + |V_q|^2)\right]V_j + Y\left(\overline{V_pW_q} + \overline{V_qW_p}\right), \tag{2.102}$$

$$\overbrace{v_1 v_2}^{}_{j} = \left[(\widetilde{v_0} + \widetilde{vv})|V_j|^2 + (\widetilde{v_0} + \widetilde{vv_{\neq}})(|V_p|^2 + |V_q|^2)\right]V_j + \left(\overline{V_pW_q} + \overline{V_qW_p}\right), \tag{2.103}$$

$$\overbrace{u_1^2 v_1}^{}_{j} = \left(3|V_j|^2 + 6|V_p|^2 + 6|V_q|^2\right)Y^2V_j, \tag{2.104}$$

$$\overbrace{u_1 v_1^2}^{}_{j} = \left(3|V_j|^2 + 6|V_p|^2 + 6|V_q|^2\right)YV_j, \tag{2.105}$$

$$\overbrace{v_1^3}^{}_{j} = \left(3|V_j|^2 + 6|V_p|^2 + 6|V_q|^2\right)V_j. \tag{2.106}$$

The first element of the third term of Eq. 2.99 can be rewritten as

$$\left[G_{11}|V_j|^2 + G_{12}(|V_p|^2 + |V_q|^2)\right] V_j + \left(-\frac{2}{v^*}Y^2 + 2\frac{2u^*}{(v^*)^2}Y - 2\frac{(u^*)^2 + A_0}{(v^*)^3}\right)\left(\overline{V_pW_q} + \overline{V_qW_p}\right), \tag{2.107}$$

where

$$\begin{aligned} G_{11} = &\left(-\frac{2}{v^*}Y + \frac{2u^*}{(v^*)^2}\right)(\widetilde{u_0} + \widetilde{uu}) + \left(\frac{2u^*}{(v^*)^2}Y - 2\frac{(u^*)^2 + A_0}{(v^*)^3}\right)(\widetilde{v_0} + \widetilde{vv}) \\ &+ 3\left(\frac{1}{(v^*)^2}Y^2 - \frac{2u^*}{(v^*)^3}Y + \frac{(u^*)^2 + A_0}{(v^*)^4}\right), \end{aligned} \tag{2.108}$$

$$\begin{aligned} G_{12} = &\left(-\frac{2}{v^*}Y + \frac{2u^*}{(v^*)^2}\right)(\widetilde{u_0} + \widetilde{uu_{\neq}}) + \left(\frac{2u^*}{(v^*)^2}Y - 2\frac{(u^*)^2 + A_0}{(v^*)^3}\right)(\widetilde{v_0} + \widetilde{vv_{\neq}}) \\ &+ 6\left(\frac{1}{(v^*)^2}Y^2 - \frac{2u^*}{(v^*)^3}Y + \frac{(u^*)^2 + A_0}{(v^*)^4}\right). \end{aligned} \tag{2.109}$$

The second element of the third term of Eq. 2.99 can be rewritten as

$$\left[G_{21}|V_j|^2 + G_{22}(|V_p|^2 + |V_q|^2)\right] V_j + \left(-2PY^2\right)\left(\overline{V_pW_q} + \overline{V_qW_p}\right), \tag{2.110}$$

where

$$G_{21} = (-2PY)(\widetilde{u_0} + \widetilde{uu}) \tag{2.111}$$

$$G_{22} = (-2PY)(\widetilde{u_0} + \widetilde{uu_{\neq}}). \tag{2.112}$$

By Eq. 2.98, we have, for $j, p, q \in [1, 2, 3]$ and $j \neq p \neq q$,

$$\begin{aligned} (Y - DY)\left(\frac{\partial}{\partial t_1}W_j + \frac{\partial}{\partial t_2}V_j\right) = &-DY(-2Y + 1)\left(Q_1W_j + Q_2V_j\right) \\ &+ \left[(-G_{11} + DYG_{21})|V_j|^2 + (-G_{12} + DYG_{22})(|V_p|^2 + |V_q|^2)\right] V_j \\ &+ \left(\frac{2}{v^*}Y^2 - 2\frac{2u^*}{(v^*)^2}Y + 2\frac{(u^*)^2 + A_0}{(v^*)^3} - 2PDY^3\right)\left(\overline{V_pW_q} + \overline{V_qW_p}\right). \end{aligned} \tag{2.113}$$

The amplitude A_j can be expanded into

$$A_j = \epsilon V_j + \epsilon^2 W_j + O(\epsilon^3). \tag{2.114}$$

Combining Eq. 2.79, Eq. 2.81 and Eq. 2.114, we have

$$\begin{aligned}(Q_T - Q)A_j &= (\epsilon Q_1 + \epsilon^2 Q_2 + \cdots)(\epsilon V_j + \epsilon^2 W_j + \cdots) \\ &= Q_1 V_j \epsilon^2 + (Q_1 W_j + Q_2 V_j)\epsilon^3 + \cdots ,\end{aligned} \tag{2.115}$$

$$\begin{aligned}\frac{\partial}{\partial t} A_j &= \left(\frac{\partial}{\partial t_0} + \epsilon \frac{\partial}{\partial t_1} + \epsilon^2 \frac{\partial}{\partial t_2} + \cdots\right)(\epsilon V_j + \epsilon^2 W_j + \cdots) \\ &= \left(\frac{\partial}{\partial t_1} V_j\right)\epsilon^2 + \left(\frac{\partial}{\partial t_1} W_j + \frac{\partial}{\partial t_2} V_j\right)\epsilon^3 + \cdots ,\end{aligned} \tag{2.116}$$

and

$$\begin{aligned}\overline{A_p A_q} &= (\epsilon \overline{V_p} + \epsilon^2 \overline{W_p} + \cdots)(\epsilon \overline{V_q} + \epsilon^2 \overline{W_q} + \cdots) \\ &= \overline{V_p V_q}\epsilon^2 + (\overline{V_p W_q} + \overline{W_p V_q})\epsilon^3 + \cdots ,\end{aligned} \tag{2.117}$$

$$|A_j|^2 A_j = |V_j|^2 V_j \epsilon^3 + \cdots \tag{2.118}$$

$$|A_p|^2 A_j = |V_p|^2 V_j \epsilon^3 + \cdots . \tag{2.119}$$

By Eq. 2.89 and Eq. 2.113,

$$\begin{aligned}Y(1-D)\frac{\partial}{\partial t} A_j &= DY(2Y-1)(Q_T - Q)A_j \\ &+ \left(2(\frac{1}{v^*}Y^2 - 2\frac{u^*}{(v^*)^2}Y + \frac{(u^*)^2 + A_0}{(v^*)^3}) - 2PDY^3\right)\overline{A_p}\,\overline{A_q} \\ &+ \left[(DYG_{21} - G_{11})|A_j|^2 + (DYG_{22} - G_{12})(|A_p|^2 + |A_q|^2)\right] A_j\end{aligned} \tag{2.120}$$

.

The amplitude equation can be written as

$$\frac{\partial}{\partial t}A_j \doteq \sigma A_j + \xi\overline{A_p}\,\overline{A_q} - \left[\gamma_1|A_j|^2 + \gamma_2(|A_p|^2 + |A_q|^2)\right] A_j, \tag{2.121}$$

where

$$\begin{aligned}
\sigma &= \frac{DY(2Y-1)(Q_T - Q)}{Y(1-D)} \\
\xi &= \frac{2(\frac{1}{v^*}Y^2 - 2\frac{u^*}{(v^*)^2}Y + \frac{(u^*)^2+A_0}{(v^*)^3}) - 2PDY^3}{Y(1-D)} \\
\gamma_1 &= \frac{G_{11} - DYG_{21}}{Y(1-D)} \\
\gamma_2 &= \frac{G_{12} - DYG_{22}}{Y(1-D)}
\end{aligned}$$

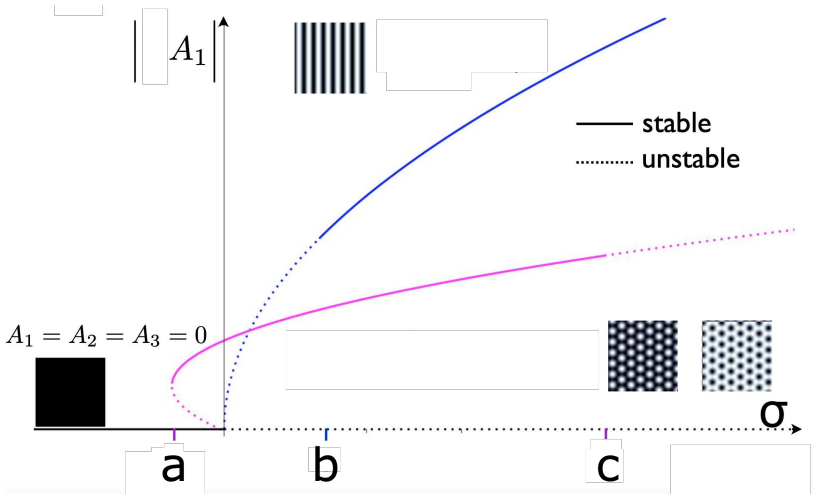

Figure 2.27: The bifurcation diagram for the amplitude equation in the case $0 < \gamma_1 < \gamma_2$ in Eq. 2.121. Rolls are stable in the range $\sigma > c = \frac{\xi^2(2\gamma_1+\gamma_2)}{(\gamma_1-\gamma_2)^2}$. Both hexagons and rolls are stable in the range $b = \frac{\xi^2\gamma_1}{(\gamma_1-\gamma_2)^2} < \sigma < c$.

Observations

From our analysis, we arrive at the following observations:

- If we choose the parameter Q that is very close to the Turing bifurcation Q_T, we can have more ordered patterns, such as hexagon and rolls; see Figure 2.26. If Q is far from Q_T, then the patterns will not have those ordered patterns; see Figure 2.21.

- In the case $Q = 0.98Q_T$, we will have the hexagon down pattern Figure 2.29; while the case $Q = 0.83Q_T$, the pattern will be the hexagon up Figure 2.31. These two patterns can be regarded as the complementary. The reason we will have these two kinds of patterns is the sign of $\frac{\gamma_1}{\xi}$ could be positive or negative. In the case of hexagon up Figure 2.31, the $\frac{\gamma_1}{\xi}$ value is negative; while the case $Q = 0.98 \times Q_T$, we have $\frac{\gamma_1}{\xi} > 0$.

- For $0.83Q_T < Q < 0.98Q_T$, the system evolves to a pattern of rolls; see Figure 2.30. One interesting aspect of this evolution is that the square pattern will evaluate to the hexagon up after a while.

- The coefficient γ_1 in our amplitude equation 2.121 could be negative, which means the bifurcation diagram Figure 2.27 does not apply for this situation. We need to include higher order terms in the amplitude equation and find the bifurcation. In the case $\gamma_1 > 0$, which will be $Q \leq 0.88 \times Q_T$, we have σ in the range $b < \sigma < c$ for $0.85 \times Q_T \leq Q \leq 0.88 \times Q_T$, and we have rolls pattern. When $Q = 0.84Q_T$, the σ in the range $\sigma > c$, which means that the roll pattern is stable, and we have rolls pattern after 5×10^3(s); see Figure 2.28. This is consistent with predictions from the bifurcation diagram.

- In the case $Q \leq 0.83 \times Q_T$, we will have hexagon up patterns; see Figure 2.31.

In the following results, we choose the parameters as $G_A = 0.08, G_I = 0.12, K = 0.001, A_0 = 0.01, D_A = 0.05, D_I = 0.5$.

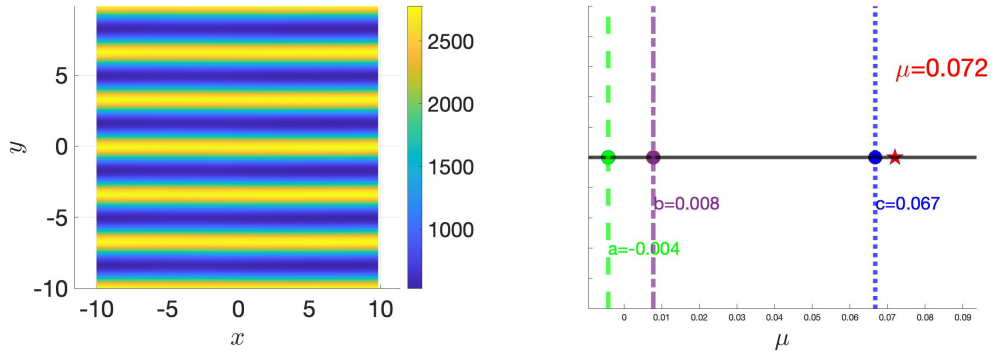

(a) Evolution after 5×10^3(s). **(b)** σ in Eq. 2.121 is in the range $\sigma > c$.

Figure 2.28: In the case $Q = 0.84Q_T$. The original parameters are $G_A = 0.08, G_I = 0.12, K = 0.001, A_0 = 0.01, U_A = 0.03, D_A = 0.05$, and $D_I = 0.5$. In terms of the nondimensional parameters of Eq. 2.61, we have the coefficients $P = 5.6250 \cdot 10^{-4}Q, u_0 = \frac{71111}{Q^2}$, and $D = 0.1$.

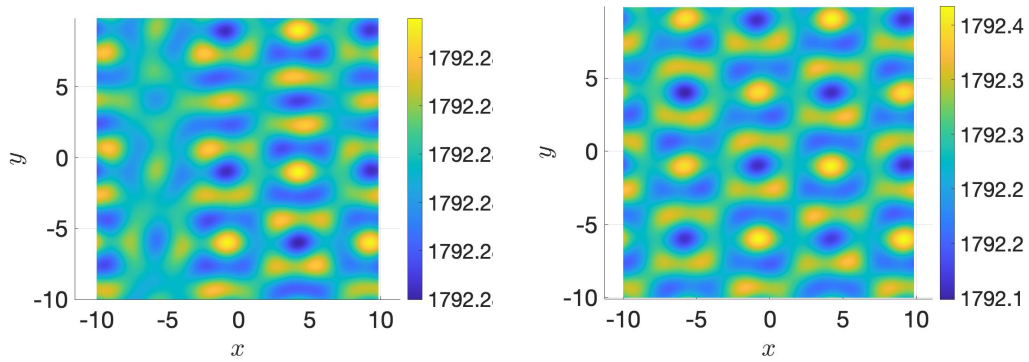

(a) Evolution after 1×10^4(s). **(b)** Evolution after 2×10^4(s).

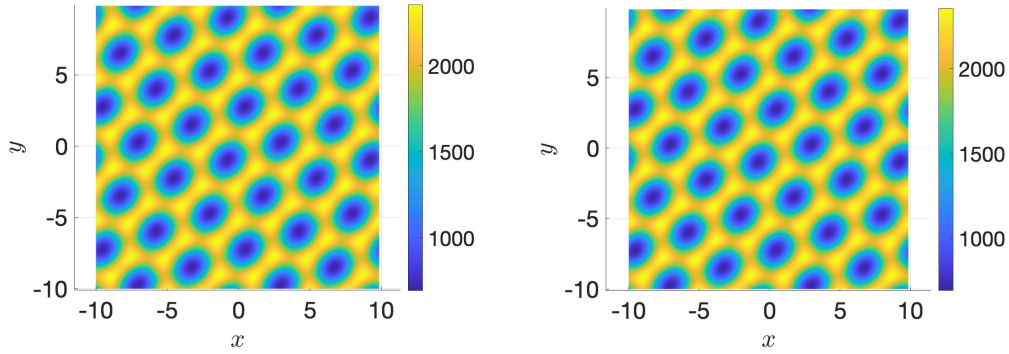

(c) Evolution after 4×10^4(s). **(d)** Evolution after 8×10^4(s).

Figure 2.29: In the case $Q = 0.98Q_T$. The original parameters are $G_A = 0.08, G_I = 0.12, K = 0.001, A_0 = 0.01, U_A = 0.03, D_A = 0.05$, and $D_I = 0.5$. In terms of the nondimensional parameters of Eq. 2.61, we have the coefficients $P = 5.6250 \cdot 10^{-4}Q, u_0 = \frac{71111}{Q^2}$, and $D = 0.1$.

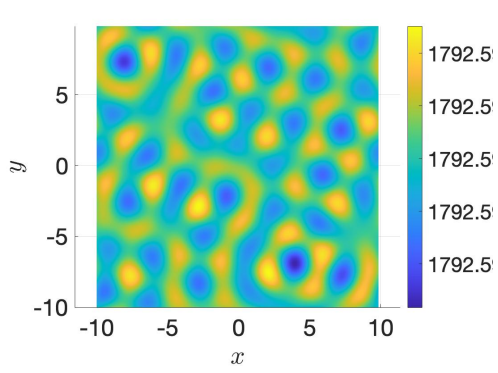

(a) Evolution after 1×10^4(s).

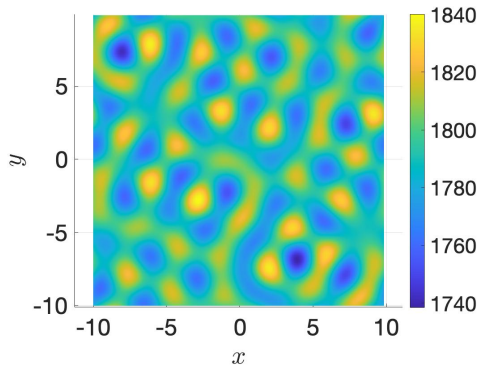

(b) Evolution after 2×10^4(s).

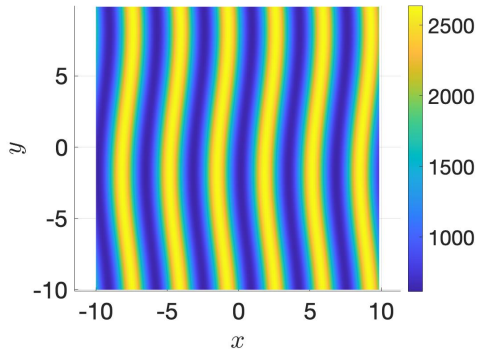

(c) Evolution after 4×10^4(s).

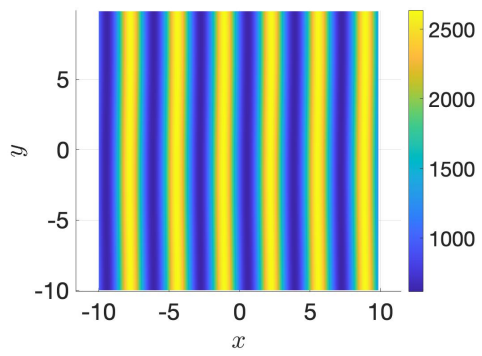

(d) Evolution after 8×10^4(s).

Figure 2.30: In the case $Q = 0.94Q_T$. The original parameters are $G_A = 0.08, G_I = 0.12, K = 0.001, A_0 = 0.01, U_A = 0.03, D_A = 0.05$, and $D_I = 0.5$. In terms of the nondimensional parameters of Eq. 2.61, we have the coefficients $P = 5.6250 \cdot 10^{-4}Q, u_0 = \frac{71111}{Q^2}$, and $D = 0.1$.

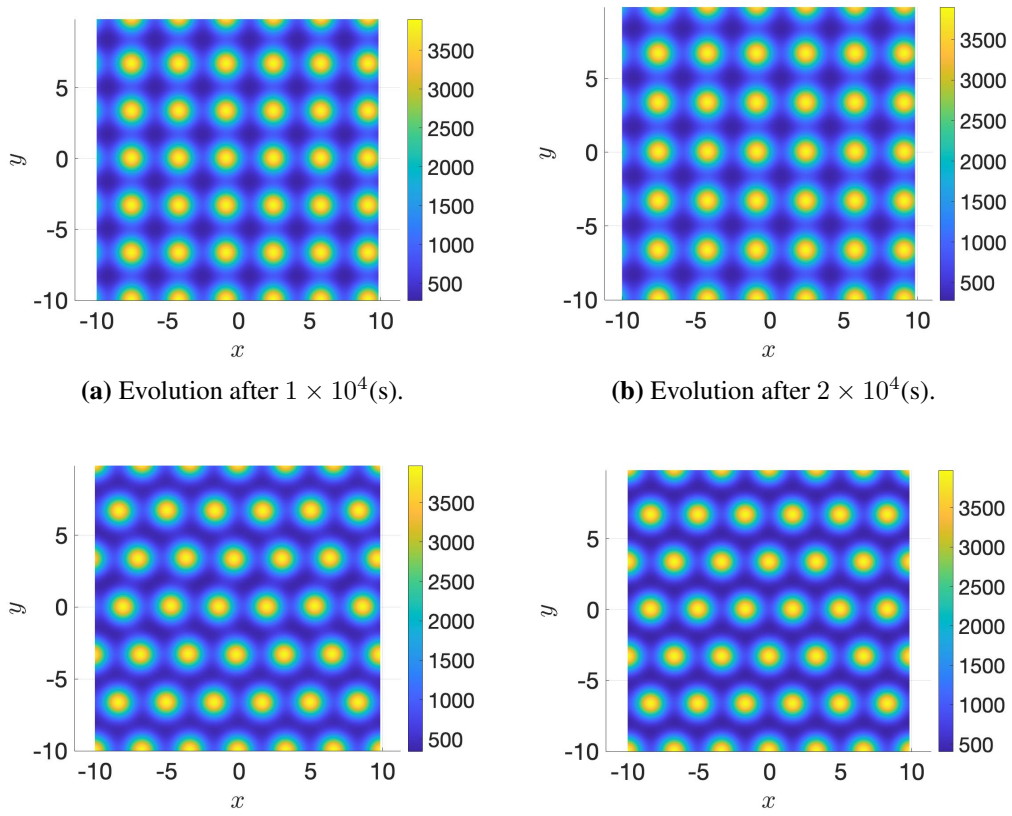

(a) Evolution after 1×10^4(s).

(b) Evolution after 2×10^4(s).

(c) Evolution after 4×10^4(s).

(d) Evolution after 8×10^4(s).

Figure 2.31: In the case $Q = 0.83Q_T$. The original parameters are $G_A = 0.08, G_I = 0.12, K = 0.001, A_0 = 0.01, U_A = 0.03, D_A = 0.05$, and $D_I = 0.5$. In terms of the nondimensional parameters of Eq. 2.61, we have the coefficients $P = 5.6250 \cdot 10^{-4}Q, u_0 = \frac{71111}{Q^2}$, and $D = 0.1$.

Roll-Square competition

We now analyze the competition between rolls and square patterns. This analysis proceeds analogously to that for roll-hexagon competition. Even so, at the acknowledged expense of being repetitive, we include the full analysis for the sake of completeness and to have the details of the computations on hand.

We consider the bifurcation parameter Q is slightly below the critical value Q_T, and set

$$Q = Q_T - \epsilon Q_1 - \epsilon^2 Q_2 - \epsilon^3 Q_3 - \epsilon^4 Q_4 + \cdots , \tag{2.122}$$

where $\epsilon > 0$ is small and $Q_j > 0$ are of order j for $j \in \mathbb{N}$. In Figure 2.24b and Figure 2.25b, there is an interval around k_T in which $\mathrm{Re}(\lambda_{k_+}) > 0$. We can also decompose the linear operator $\mathscr{L}$ into

$$\mathscr{L} = \mathscr{L}_T + (Q_T - Q)\mathscr{M} ,$$

and write

$$\frac{\partial}{\partial \tau} = \frac{\partial}{\partial t_0} + \epsilon \frac{\partial}{\partial t_1} + \epsilon^2 \frac{\partial}{\partial t_2} + \epsilon^3 \frac{\partial}{\partial t_3} + \epsilon^4 \frac{\partial}{\partial t_4} + \cdots . \tag{2.123}$$

We expand u and v in powers of ϵ and write

$$\begin{pmatrix} u \\ v \end{pmatrix} = \begin{pmatrix} (u^*)_T \\ (v^*)_T \end{pmatrix} + \epsilon \begin{pmatrix} u_1 \\ v_1 \end{pmatrix} + \epsilon^2 \begin{pmatrix} u_2 \\ v_2 \end{pmatrix} + \epsilon^3 \begin{pmatrix} u_3 \\ v_3 \end{pmatrix} + \epsilon^4 \begin{pmatrix} u_4 \\ v_4 \end{pmatrix} + \cdots . \tag{2.124}$$

At order ϵ, we have

$$\mathscr{L}_T \begin{pmatrix} u_1 \\ v_1 \end{pmatrix} = \begin{pmatrix} 0 \\ 0 \end{pmatrix} , \tag{2.125}$$

which has solutions of the form

$$\begin{pmatrix} u_1 \\ v_1 \end{pmatrix} = \sum_{j=1}^{2} \begin{pmatrix} \frac{DQ_T + \frac{2(u^*)_T}{(v^*)_T} - 1}{4PD(u^*)_T} \\ 1 \end{pmatrix} (V_{1,j} e^{i\mathbf{k}_j \cdot \mathbf{x}} + c.c.). \tag{2.126}$$

where $\mathbf{k}_1 \cdot \mathbf{k}_2 = 0$, and $\mathbf{k}_j \in \mathbb{C}$ for $j = 1, 2$.

The system obtained at order ϵ^2 is

$$\mathscr{L}_T \begin{pmatrix} u_2 \\ v_2 \end{pmatrix} = \frac{\partial}{\partial t_1} \begin{pmatrix} u_1 \\ v_1 \end{pmatrix} - Q_1 \mathscr{M} \begin{pmatrix} u_1 \\ v_1 \end{pmatrix} - \begin{pmatrix} \frac{1}{v^*} u_1^2 - 2\frac{u^*}{(v^*)^2} u_1 v_1 + \frac{(u^*)^2 + A_0}{(v^*)^3} v_1^2 \\ P u_1^2 \end{pmatrix} \doteq \begin{pmatrix} F_u \\ F_v \end{pmatrix}. \tag{2.127}$$

According to the Fredholm Alternative, Eq. 2.127 has a solution if and only if $(F_u, F_v)^T$ is orthogonal to the kernel of the adjoint operator $\mathscr{L}_T^\dagger$. The zero eigenvector of $\mathscr{L}_T^\dagger$ is

$$\begin{pmatrix} 1 \\ -\frac{DQ_T + \frac{2(u^*)_T}{(v^*)_T} - 1}{4P(u^*)_T} \end{pmatrix} (e^{i\mathbf{k}_j \cdot \mathbf{x}} + c.c.). \tag{2.128}$$

Denote $\frac{DQ_T + \frac{2(u^*)_T}{(v^*)_T} - 1}{4PD(u^*)_T}$ by Y, and let F_u^j, F_v^j represent the coefficients corresponding to $e^{i\mathbf{k}_j \cdot \mathbf{x}}$, then from Eq. 2.127, we have, for $j \in [1, 2]$,

$$\begin{pmatrix} F_u^j \\ F_v^j \end{pmatrix} = \begin{pmatrix} Y \frac{\partial}{\partial t_1} V_{1,j} \\ \frac{\partial}{\partial t_1} V_{1,j} \end{pmatrix} - Q_1 \begin{pmatrix} 0 \\ (-2Y + 1) V_{1,j} \end{pmatrix}. \tag{2.129}$$

Since

$$(1, -DY) \begin{pmatrix} F_u^j \\ F_v^j \end{pmatrix} = 0, \text{ for } j \in [1, 2] \tag{2.130}$$

we have, for $j \in [1,2]$,

$$Y(1-D)\frac{\partial}{\partial t_1}V_{1,j} = -DY(-2Y+1)Q_1 V_{1,j}. \tag{2.131}$$

Here we introduce high-order terms and set

$$\begin{pmatrix} u_2 \\ v_2 \end{pmatrix} = \begin{pmatrix} U_0 \\ V_0 \end{pmatrix} + \sum_{j=1}^{2} \begin{pmatrix} UU_j \\ VV_j \end{pmatrix} \exp(2i\mathbf{k}_j \cdot \mathbf{x}) + \begin{pmatrix} UU_{12} \\ VV_{12} \end{pmatrix} \exp(i(\mathbf{k}_1+\mathbf{k}_2)\cdot\mathbf{x}) + +c.c., \tag{2.132}$$

then

$$\begin{aligned} \mathscr{L}_T \begin{pmatrix} u_2 \\ v_2 \end{pmatrix} = & \begin{pmatrix} \frac{2(u^*)_T}{(v^*)_T} - 1 & -\frac{(u^*)_T}{(v^*)_T} \\ 2P(u^*)_T & -Q_T \end{pmatrix} \begin{pmatrix} U_0 \\ V_0 \end{pmatrix} \\ & + \sum_{j=1}^{2} \begin{pmatrix} -4Dk^2 + \frac{2(u^*)_T}{(v^*)_T} - 1 & -\frac{(u^*)_T}{(v^*)_T} \\ 2P(u^*)_T & -4k^2 - Q_T \end{pmatrix} \begin{pmatrix} UU_j \\ VV_j \end{pmatrix} \exp(2i\mathbf{k}_j \cdot \mathbf{x}) \\ & + \begin{pmatrix} -2Dk^2 + \frac{2(u^*)_T}{(v^*)_T} - 1 & -\frac{(u^*)_T}{(v^*)_T} \\ 2P(u^*)_T & -2k^2 - Q_T \end{pmatrix} \begin{pmatrix} UU_{12} \\ VV_{12} \end{pmatrix} \exp(i(\mathbf{k}_1+\mathbf{k}_2)\cdot\mathbf{x}) + c.c., \end{aligned} \tag{2.133}$$

because $|\mathbf{k}_1 + \mathbf{k}_2| = \sqrt{2}k$ if $|\mathbf{k}_1| = |\mathbf{k}_2| = k$. The first element of the third term of the right hand side of Eq. 2.127 is

$$\begin{aligned} -\left(\frac{Y^2}{v^*} - 2\frac{Yu^*}{(v^*)^2} + \frac{(u^*)^2 + A_0}{(v^*)^3}\right) & \left(\sum_{j=1}^{2} V_{1,j}^2 \exp(2i\mathbf{k}_j \cdot \mathbf{x})\right. \\ & \left. +2\sum_{j=1}^{2} V_{1,j}\overline{V_{1,j}} + 2V_{1,1}V_{1,2}\exp(i(\mathbf{k}_1+\mathbf{k}_2)\cdot\mathbf{x}) + c.c.\right). \end{aligned} \tag{2.134}$$

We can write $V_{1,j}\overline{V_{1,j}} = |V_{1,j}|^2$. Then the second element can be expressed

$$-PY^2\left(\sum_{j=1}^{2} V_{1,j}^2 \exp(2i\mathbf{k}_j \cdot \mathbf{x}) + 2\sum_{j=1}^{2} |V_{1,j}|^2 + 2V_{1,1}V_{1,2}\exp(i(\mathbf{k}_1+\mathbf{k}_2)\cdot\mathbf{x}) + c.c.\right) \tag{2.135}$$

Solving Eq. 2.127, we have

$$\begin{pmatrix} U_0 \\ V_0 \end{pmatrix} = \begin{pmatrix} \frac{2(u^*)_T}{(v^*)_T} - 1 & -\frac{(u^*)_T}{(v^*)_T} \\ 2P(u^*)_T & -Q_T \end{pmatrix}^{-1} \begin{pmatrix} -2\left(\frac{Y^2}{v^*} - 2\frac{Yu^*}{(v^*)^2} + \frac{(u^*)^2+A_0}{(v^*)^3}\right) \\ -2PY^2 \end{pmatrix} (|V_{1,1}|^2 + |V_{1,2}|^2) \tag{2.136}$$

$$\doteq \begin{pmatrix} \widetilde{u_0} \\ \widetilde{v_0} \end{pmatrix} (|V_{1,1}|^2 + |V_{1,2}|^2),$$

$$\begin{pmatrix} UU_j \\ VV_j \end{pmatrix} = \begin{pmatrix} -4Dk^2 + \frac{2(u^*)_T}{(v^*)_T} - 1 & -\frac{(u^*)_T}{(v^*)_T} \\ 2P(u^*)_T & -4k^2 - Q_T \end{pmatrix}^{-1} \begin{pmatrix} -\left(\frac{Y^2}{v^*} - 2\frac{Yu^*}{(v^*)^2} + \frac{(u^*)^2+A_0}{(v^*)^3}\right) \\ -PY^2 \end{pmatrix} V_{1,j}^2 \tag{2.137}$$

$$\doteq \begin{pmatrix} \widetilde{uu} \\ \widetilde{vv} \end{pmatrix} V_{1,j}^2,$$

$$\begin{pmatrix} UU_{12} \\ VV_{12} \end{pmatrix} = \begin{pmatrix} -2Dk^2 + \frac{2(u^*)_T}{(v^*)_T} - 1 & -\frac{(u^*)_T}{(v^*)_T} \\ 2P(u^*)_T & -2k^2 - Q_T \end{pmatrix}^{-1} \begin{pmatrix} -2\left(\frac{Y^2}{v^*} - 2\frac{Yu^*}{(v^*)^2} + \frac{(u^*)^2+A_0}{(v^*)^3}\right) \\ -2PY^2 \end{pmatrix} V_{1,1}V_{1,2} \tag{2.138}$$

$$\doteq \begin{pmatrix} \widetilde{uu_{\neq}} \\ \widetilde{vv_{\neq}} \end{pmatrix} V_{1,1}V_{1,2}.$$

At order ϵ^3, we have

$$\begin{aligned}\mathscr{L}_T \begin{pmatrix} u_3 \\ v_3 \end{pmatrix} &\doteq \begin{pmatrix} H_u \\ H_v \end{pmatrix} \\ &= \frac{\partial}{\partial t_1}\begin{pmatrix} u_2 \\ v_2 \end{pmatrix} + \frac{\partial}{\partial t_2}\begin{pmatrix} u_1 \\ v_1 \end{pmatrix} - Q_1\mathscr{M}\begin{pmatrix} u_2 \\ v_2 \end{pmatrix} - Q_2\mathscr{M}\begin{pmatrix} u_1 \\ v_1 \end{pmatrix} - \begin{pmatrix} N_3(u,v) \\ 2Pu_1u_2 \end{pmatrix},\end{aligned} \tag{2.139}$$

where

$$\begin{aligned}N_3(u,v) =& \frac{1}{v^*}2u_1u_2 - 2\frac{u^*}{(v^*)^2}(u_1v_2+u_2v_1) + \frac{(u^*)^2+A_0}{(v^*)^3}2v_1v_2 \\ &- \frac{1}{(v^*)^2}u_1^2v_1 + \frac{2u^*}{(v^*)^3}u_1v_1^2 - \frac{(u^*)^2+A_0}{(v^*)^4}v_1^3.\end{aligned}$$

Again, according to the Fredholm Alternative, Eq. 2.139 has a solution if and only if

$$(1, -DY)\begin{pmatrix} H_u^j \\ H_v^j \end{pmatrix} = 0, \text{ for } j \in [1,2], \tag{2.140}$$

when we denote H_u^j, H_v^j represent the coefficients corresponding to $e^{i\mathbf{k}_j\cdot\mathbf{x}}$.

Expanding $(H_u^j, H_v^j)^T$ as

$$\begin{pmatrix} H_u^j \\ H_v^j \end{pmatrix} = \begin{pmatrix} Y\frac{\partial}{\partial t_2}V_{1,j} \\ \frac{\partial}{\partial t_2}V_{1,j} \end{pmatrix} - \begin{pmatrix} 0 \\ (-2Y+1)Q_2V_{1,j} \end{pmatrix} + \begin{pmatrix} NH_u^j \\ -2P\overbrace{u_1u_2}^{}_{j} \end{pmatrix}, \tag{2.141}$$

where $\overbrace{ab}^{}_{j}$ is the coefficient corresponding to $e^{i\mathbf{k}_j\cdot\mathbf{x}}$ in ab, and

$$\begin{aligned}NH_u^j =& -\frac{2}{v^*}\overbrace{u_1u_2}^{}_{j} + \frac{2u^*}{(v^*)^2}(\overbrace{u_1v_2}^{}_{j} + \overbrace{u_2u_1}^{}_{j}) - 2\frac{(u^*)^2+A_0}{(v^*)^3}\overbrace{v_1v_2}^{}_{j} \\ &+ \frac{1}{(v^*)^2}\overbrace{u_1^2v_1}^{}_{j} - \frac{2u^*}{(v^*)^3}\overbrace{u_1v_1^2}^{}_{j} + \frac{(u^*)^2+A_0}{(v^*)^4}\overbrace{v_1^3}^{}_{j}.\end{aligned}$$

For $j, p \in [1, 2]$ and $j \neq p$, their expansions are

$$\begin{aligned}
\overbrace{\underset{j}{u_1 u_2}} &= Y V_{1,j} \widetilde{u_0}(|V_{1,j}|^2 + |V_{1,p}|^2) + Y \overline{V_{1,j}} \widetilde{uu} V_{1,j}^2 + Y \overline{V_{1,p}} \widetilde{uu_{\neq}} V_{1,j} V_{1,p} \\
&= Y \left[(\widetilde{u_0} + \widetilde{uu})|V_{1,j}|^2 + (\widetilde{u_0} + \widetilde{uu_{\neq}})|V_{1,p}|^2 \right] V_{1,j}, \qquad (2.142) \\
\overbrace{\underset{j}{u_1 v_2}} &= Y \left[(\widetilde{v_0} + \widetilde{vv})|V_{1,j}|^2 + (\widetilde{v_0} + \widetilde{vv_{\neq}})|V_{1,p}|^2 \right] V_{1,j}, \qquad (2.143) \\
\overbrace{\underset{j}{v_1 u_2}} &= \left[(\widetilde{u_0} + \widetilde{uu})|V_{1,j}|^2 + (\widetilde{u_0} + \widetilde{uu_{\neq}})|V_{1,p}|^2 \right] V_{1,j}, \qquad (2.144) \\
\overbrace{\underset{j}{v_1 v_2}} &= \left[(\widetilde{v_0} + \widetilde{vv})|V_{1,j}|^2 + (\widetilde{v_0} + \widetilde{vv_{\neq}})|V_{1,p}|^2 \right] V_{1,j}, \qquad (2.145) \\
\overbrace{\underset{j}{u_1^2 v_1}} &= \left(3|V_{1,j}|^2 + 6|V_{1,p}|^2 \right) Y^2 V_{1,j}, \qquad (2.146) \\
\overbrace{\underset{j}{u_1 v_1^2}} &= \left(3|V_{1,j}|^2 + 6|V_{1,p}|^2 \right) Y V_{1,j}, \qquad (2.147) \\
\overbrace{\underset{j}{v_1^3}} &= \left(3|V_{1,j}|^2 + 6|V_{1,p}|^2 \right) V_{1,j}. \qquad (2.148)
\end{aligned}$$

The first element of the third term of Eq. 2.141 can rewrite as

$$\left[G_{11}|V_{1,j}|^2 + G_{12}|V_{1,p}|^2 \right] V_{1,j}, \qquad (2.149)$$

where

$$\begin{aligned}
G_{11} &= \left(-\frac{2}{v^*} Y + \frac{2u^*}{(v^*)^2} \right) (\widetilde{u_0} + \widetilde{uu}) + \left(\frac{2u^*}{(v^*)^2} Y - 2\frac{(u^*)^2 + A_0}{(v^*)^3} \right) (\widetilde{v_0} + \widetilde{vv}) \\
&\quad + 3 \left(\frac{1}{(v^*)^2} Y^2 - \frac{2u^*}{(v^*)^3} Y + \frac{(u^*)^2 + A_0}{(v^*)^4} \right), \qquad (2.150) \\
G_{12} &= \left(-\frac{2}{v^*} Y + \frac{2u^*}{(v^*)^2} \right) (\widetilde{u_0} + \widetilde{uu_{\neq}}) + \left(\frac{2u^*}{(v^*)^2} Y - 2\frac{(u^*)^2 + A_0}{(v^*)^3} \right) (\widetilde{v_0} + \widetilde{vv_{\neq}}) \\
&\quad + 6 \left(\frac{1}{(v^*)^2} Y^2 - \frac{2u^*}{(v^*)^3} Y + \frac{(u^*)^2 + A_0}{(v^*)^4} \right). \qquad (2.151)
\end{aligned}$$

The second element of the third term of Eq. 2.141 can rewrite as

$$\left[G_{21}|V_{1,j}|^2 + G_{22}|V_{1,p}|^2 \right] V_{1,j}, \qquad (2.152)$$

where

$$G_{21} = (-2PY)(\widetilde{u_0} + \widetilde{uu}) \tag{2.153}$$

$$G_{22} = (-2PY)(\widetilde{u_0} + \widetilde{uu_{\neq}}). \tag{2.154}$$

By Eq. 2.140, we have, for $j, p \in [1, 2]$ and $j \neq p$,

$$\begin{aligned}(Y - DY)\frac{\partial}{\partial t_2}V_{1,j} &= -DY(-2Y + 1)Q_2V_{1,j} \\ &\quad + \left[(-G_{11} + DYG_{21})|V_{1,j}|^2 + (-G_{12} + DYG_{22})|V_{1,p}|^2\right] V_{1,j}.\end{aligned} \tag{2.155}$$

By Eq. 2.131 and Eq. 2.155,

$$\begin{aligned}Y(1 - D)\frac{\partial}{\partial t}A_j &= DY(2Y - 1)(Q_T - Q)A_j \\ &\quad + \left[(DYG_{21} - G_{11})|A_j|^2 + (DYG_{22} - G_{12})|A_p|^2\right] A_j \\ \Rightarrow \frac{\partial}{\partial t}A_j &\doteq \mu A_j - \left[\gamma_1|A_j|^2 + \gamma_2|A_p|^2\right] A_j,\end{aligned} \tag{2.156}$$

where

$$\mu = \frac{DY(2Y - 1)(Q_T - Q)}{Y(1 - D)},\ \gamma_1 = \frac{G_{11} - DYG_{21}}{Y(1 - D)},\ \gamma_2 = \frac{G_{12} - DYG_{22}}{Y(1 - D)}.$$

Conclusions and Further Work

The coefficient γ_1 can be positive or negative. In the case $\gamma_1 > 0$, we can apply the bifurcation diagram shown in Figure 2.27 to predict what kind of pattern is stable. However, in the case $\gamma_1 < 0$, we need to extend the amplitude equations to include quartic and quintic terms in order to analyze the stability of patterns.

Our numerical simulations have found square patterns, but they evolve to hexagon patterns Figure 2.31. Are there parameter values for which square patterns are the stable steady-state solution?

We will need to derive the amplitude equations for roll-square competition but including quintic terms to test the stability of the square pattern in the mGM.

2.6.3 Activator-inhibitor system combined with anthocyanin association

In this subsection, we extend the model of Ding and colleagues to include i) anthocyanin synthesis, and ii) anthocyanin association. We assume that anthocyanin forms in the hemiketal form (B) at a rate given by a sigmoidal function of the activator, converts to AH^+ following the scheme described in Subsection 2.1, and then associates to form dimers $(AH^+)_2$, trimers $(AH^+)_3$, and larger associates, up to a largest particle size $(AH^+)_N$, according to the kinetics described in subsection 2.4. We take $N = 6$ in our simulations. In subsection 2.6.4, we further extend this model to take into account the locations in the cell of anthocyanin production and conversion to other species, to include more species in the scheme, and to allow for larger N-mers.

The rate of anthocyanin synthesis is an increasing function of activator concentration in a cell. The dependence of production rate on activator production typically follows a sigmoidal relationship [40] which we model using a function of the form like the Hill sigmoidal function for some power n with threshold, which is our constant τ. That is,

$$u_{act}(A; n, \tau) = \frac{A^n}{A^n + \tau^n}. \tag{2.157}$$

The parameter τ is a threshold value of a activator, below (above) which the production rate of anthocyanin is small (large). The author in [40] also pointed out the half of the normal amount of the activator is insufficient. Then we choose $\tau = 3$ because of the maximum of the concentration of the activator is approximately 6.

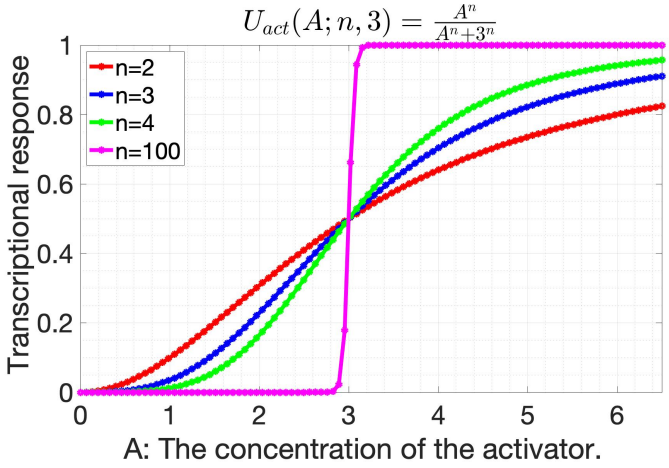

Figure 2.32: A sigmoidal relationship from Eq. 2.157 represents the dependence of production rate on activator production when the threshold constant $\tau = 3$.

Combining the activator-inhibitor system with the association scheme, we arrive at the following system of equations:

$$\frac{d[B]}{dt} = D_B \cdot \triangle\,[B] - \delta[B] + \gamma u_{act(n,thr)}(A) + (k_3[AH^+] - k_{-3}[B][H^+]) \tag{2.158}$$

$$\begin{aligned}\frac{d[AH_1^+]}{dt} =& D_{AH_1} \cdot \triangle\,[AH_1^+] - \delta[AH_1^+] - (k_3[AH^+] - k_{-3}[B][H^+]) \\ &+ 2(-j_{3,2}[AH_1^+]^2 + j_{3,-2}[AH_2^+]) + (-j_{3,3}[AH_1^+][AH_2^+] + j_{3,-3}[AH_3^+]) \\ &+ (-j_{3,4}[AH_1^+][AH_3^+] + j_{3,-4}[AH_4^+]) + (-j_{3,5}[AH_1^+][AH_4^+] + j_{3,-5}[AH_5^+]) \\ &+ (-j_{3,6}[AH_1^+][AH_5^+] + j_{3,-6}[AH_6^+])\end{aligned} \tag{2.159}$$

$$\begin{aligned}\frac{d[AH_2^+]}{dt} =& D_{AH_2} \cdot \triangle\,[AH_2^+] - \delta[AH_2^+] - (-j_{3,2}[AH_1^+]^2 + j_{3,-2}[AH_2^+]) \\ &+ (-j_{3,3}[AH_1^+][AH_2^+] + j_{3,-3}[AH_3^+])\end{aligned} \tag{2.160}$$

$$\begin{aligned}\frac{d[AH_3^+]}{dt} =& D_{AH_3} \cdot \triangle\,[AH_3^+] - \delta[AH_3^+] - (-j_{3,3}[AH_1^+][AH_2^+] + j_{3,-3}[AH_3^+]), \\ &+ (-j_{3,4}[AH_1^+][AH_3^+] + j_{3,-4}[AH_4^+])\end{aligned} \tag{2.161}$$

$$\begin{aligned}\frac{d[AH_4^+]}{dt} =& D_{AH_4} \cdot \triangle\,[AH_4^+] - \delta[AH_4^+] - (-j_{3,4}[AH_1^+][AH_3^+] + j_{3,-4}[AH_4^+]) \\ &+ (-j_{3,5}[AH_1^+][AH_4^+] + j_{3,-5}[AH_5^+])\end{aligned} \tag{2.162}$$

$$\frac{d[AH_5^+]}{dt} = D_{AH_5} \cdot \triangle [AH_5^+] - \delta[AH_5^+] - (-j_{3,5}[AH_1^+][AH_4^+] + j_{3,-5}[AH_5^+]) \tag{2.163}$$
$$+ (-j_{3,6}[AH_1^+][AH_5^+] + j_{3,-6}[AH_6^+])$$
$$\frac{d[AH_6^+]}{dt} = D_{AH_6} \cdot \triangle [AH_6^+] - \delta[AH_6^+] - (-j_{3,6}[AH_1^+][AH_5^+] + j_{3,-6}[AH_6^+]) \tag{2.164}$$

where D_B, D_{AH_1}, $D_{AH_2}, \cdots$, D_{AH_6} refer to the diffusion coefficients. Here we assume all the anthocyanins degrade with a rate δ and the hemiketal anthocyanin is activated by the activator with a potency γ. Suppose all the aggregation coefficients are the same, that is, $j_{3,n} \approx 8000(1/(M \times sec)),\ \forall n$, see [35], and set $j_{-3,n} = \frac{j_{3,n}}{J_{3,n}} \approx \frac{8000}{J_{3,n}}(1/sec),\ \forall n$.

For pH$= 1$

By the chemical reaction between a hemiketal and a flavylfum cation, namely $AH^+ \underset{\mathrm{k}_{-3}}{\overset{\mathrm{k}_3}{\rightleftharpoons}} B + H^+$, we can anticipate that we will have more anthocyanins in colored form such as $(AH^+)_n$ in lower pH values such as pH$= 1$. In the following results, we have the parameters as following

1. The production potency: $\gamma = 2 \times 10^{-5}$.
2. The diffusion coefficients: $D_B = 10^{-2},\ D_{AH_j} = 10^{-(j+1)}$, for $j = 1, 2, \cdots, 6$.
3. The aggregation constants: $J_{3,n} = 5000$, for $j = 1, 2, \cdots, 6$.
4. The proton transfer rate constants: $k_3 = 0.2849$ (1/sec), $k_{-3} = 23.7$(1/(M$\times$sec)).
5. The sigmoidal response power $n = 3$ with the threshold constant $\tau = 3$.
6. The length of time: $3 \times 10^5 \times 0.01$ seconds where a time step is 0.01.

For the activator-inhibitor system of the parameters in Figure 2.21, Figure 2.33 shows the concentrations of anthocyanins when the production potency $\gamma = 2 \times 10^{-5}$. We simulate patterns at time$= 3 \times 10^5 \times 0.01$(s) because all of the species already reached the pseudo-steady-state by that time; see Figure 2.34. It is clear that a high activator concentration leads a larger production rate of anthocyanins. So, a larger value of U_I, which corresponds to a larger activator production rate, results in a larger concentration of anthocyanins. When we look at the concentrations of anthocyanin

species such as $B, AH^+, \cdots, AH_6^+$, we realize that at the maximum point, they tend to associate to $5-$mer or $6-$mer. On the other hand, at the minimum point, monomer would dominate; see Figure 2.35.

For the higher production potency γ, we will have more anthocyanins. If we increase the production potency γ to 3×10^{-5} and look at the concentrations of anthocyanins species in Figure 2.36, we found the $6-$mer dominates the maximum while the monomer dominates the minimum when $\gamma = 3 \times 10^{-5}$ and $U_I = 0.03$.

For pH$= 5$

When we increase the pH value, by Figure 2.11, we know we will have more anthocyanins in the B or A form. If we adjust the parameters, we will have the A_6 dominates the maximum while the B dominates the minimum. In the following results, we have the parameters as following

1. The production potency: $\gamma = 7 \times 10^{-5}$.
2. The aggregation constant $J_{3,n} = 5 \times 10^4$ for $j = 1, 2, \cdots, 6$.
3. The proton transfer rate constants $k_3 = 0.2849$, $K_3 = \frac{k_3}{k_{-3}} = 10^{-pK3}$, and $pK3 = 4.5$.
4. The length of time: $2 \times 10^5 \times 0.01$ or $3 \times 10^5 \times 0.01$ or $4.5 \times 10^5 \times 0.01$ seconds where a time step is 0.01.

In these simulations, we are confronted with a huge issue, which is that the largest association number will influence our results. In other words, if we want to have more realistic results, we need to allow the anthocyanins to associate to larger size. But how large would be enough to have a satisfying result without making the association size infinity? We need the population analysis to answer this question, which is in the next subsection.

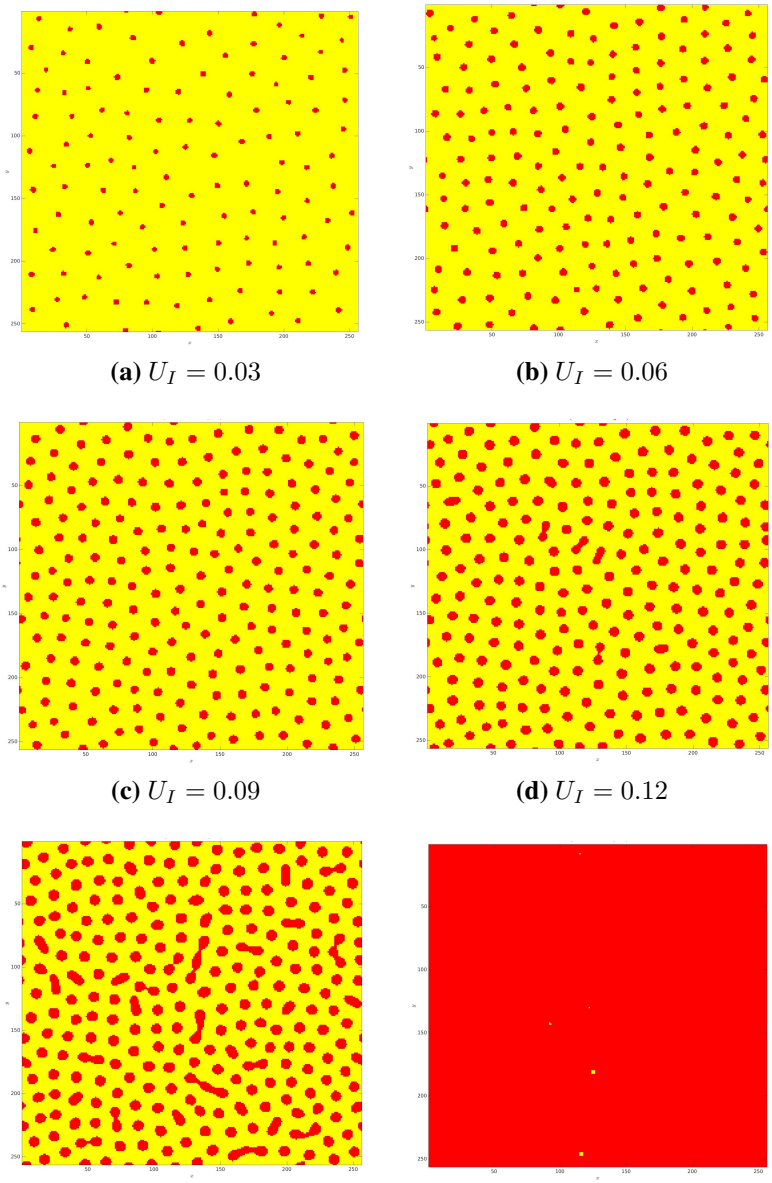

(a) $U_I = 0.03$ **(b)** $U_I = 0.06$

(c) $U_I = 0.09$ **(d)** $U_I = 0.12$

(e) $U_I = 0.15$ **(f)** $U_I = 0.18$

Figure 2.33: Spatial concentration patterns of anthocyanin at time 3×10^3 seconds, resulting from simulations of Figure 2.22 and the system Eq.(2.158) to Eq.(2.164) with parameter values as follows: The production potency is $\gamma = 2 \times 10^{-5}$, the diffusion coefficients are $D_B = 10^{-2}$, $D_{AH_j} = 10^{-(j+1)}$, for $j = 1, 2, \cdots, 6$, the degradation rate constants are $\delta = 0.01$, U_I as mentioned below each figure, the aggregation constants $J_{3,n} = 5000$, for $j = 1, 2, \cdots, 6$, the proton transfer rate constants $k_3 = 0.2849$ (1/sec), $k_{-3} = 23.7$(1/(M$\times$sec)), and the sigmoidal response power $n = 3$ with the threshold constant $\tau = 3$. The spatial domain is $0 \leq x, y \leq 50$. The time step for the simulation was 0.01 seconds, and the spatial step size was $50/256$. The red points represent the concentrations of AH^+ are greater or equal to 3, and yellow means that are less than 3.

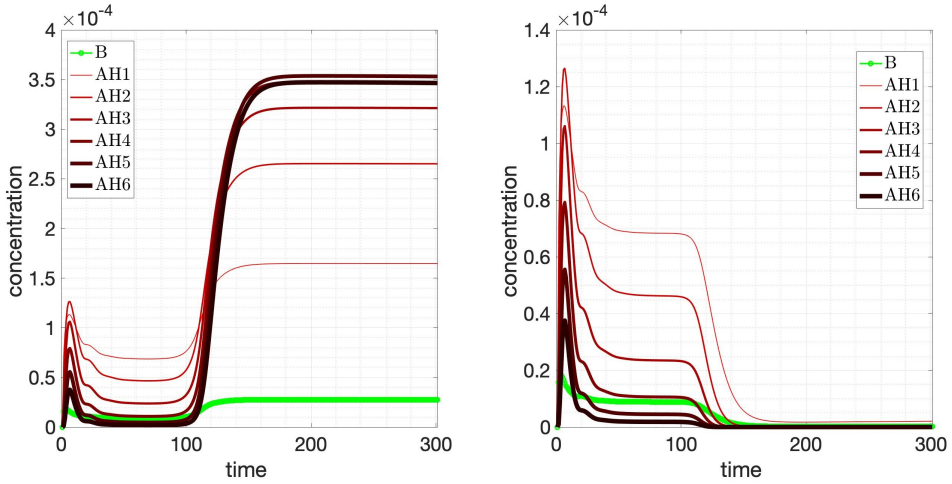

Figure 2.34: The concentrations of anthocyanin species v.s. time at the Max(L) and the min(R) position for $U_I = 0.06, \gamma = 2 \times 10^{-5}$.

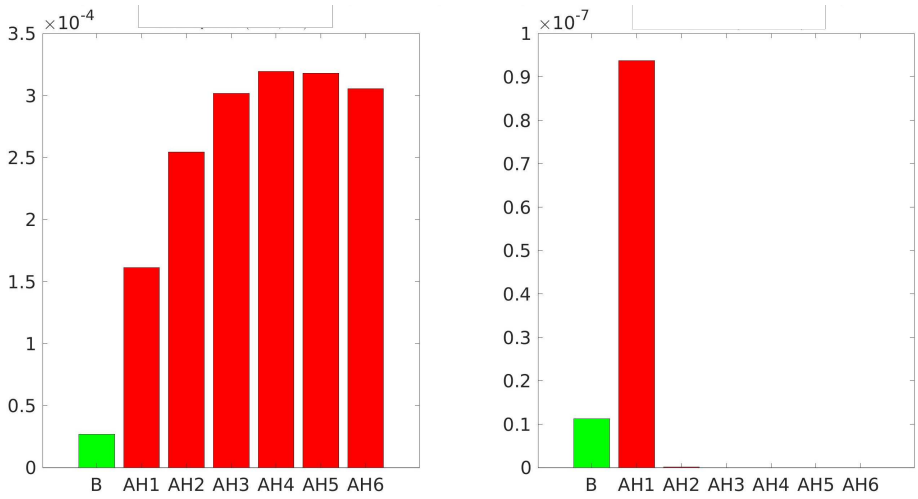

Figure 2.35: The concentrations of anthocyanin species at the end time at the Max(L) and the min(R) position for $U_I = 0.03, \gamma = 2 \times 10^{-5}$.

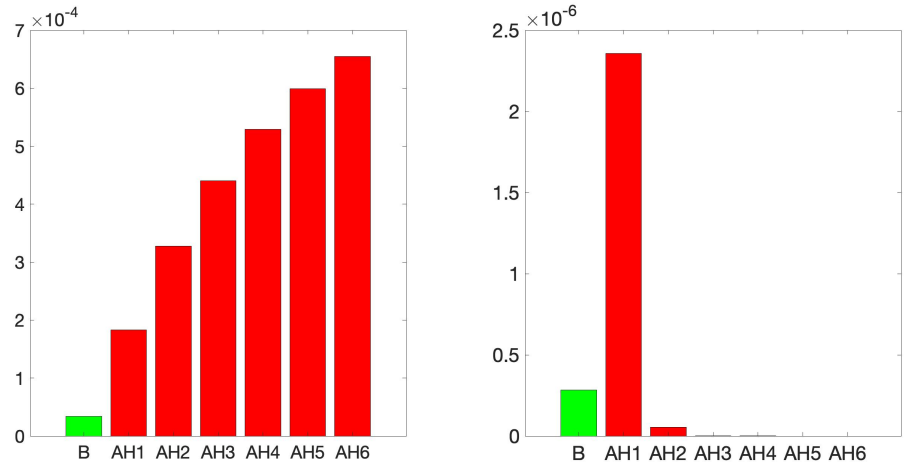

Figure 2.36: The concentrations of anthocyanin species at the end time at the Max(L) and the min(R) position for $U_I = 0.03, \gamma = 3 \times 10^{-5}$.

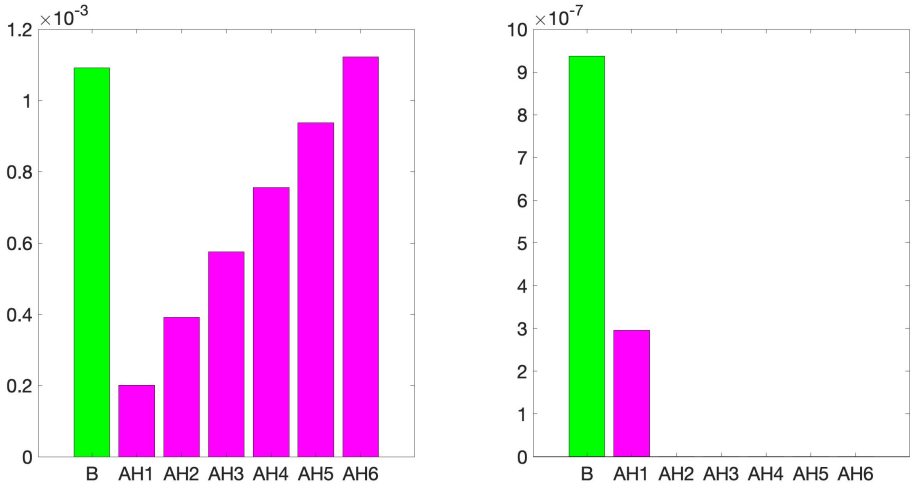

Figure 2.37: The concentrations of anthocyanin species at the end time at the Max(L) and the min(R) position for $UI = 0.03, \gamma = 7 \times 10^{-5}, J = 10^5, pK3 = 4.5$ at the end time $= 2000(s)$.

2.6.4 Activator activates the Hemiketal B in the cytoplasm

In this subsection, we extend the model given in subsection 2.6.3 to take into account the locations in the cell of anthocyanin production and conversion to other species, to include more species in the scheme, and to allow for larger N-mers.

From previous studies [56], we know that anthocyanin is synthesized in the cytoplasm, and then is transported to the vacuole. Note that the pH in the cytoplasm is approximately 7, and the range of pH values in the vacuole is $3-6$. If the anthocyanin is in the cytoplasm, it should be in the hemiketal B form, and it could diffuse to a nearby cell. On the other hand, if the anthocyanin is in the vacuole, it could be in various forms like A^-, A, or AH^+. Also, it is confined to one cell and cannot diffuse directly to other cell vacuoles because anthocyanin needs to transport back to the cytoplasm to diffuse.

In this subsection, we assume the activator only activates the Hemiketal B in cytoplasm. Then B is transported across the vacuolar membrane into the vacuole. In the vacuole, anthocyanin follows the pH-dependent scheme for conversion to other forms and may also associate. The only species that we allow to diffuse are the activator, the inhibitor, and the Hemiketal B that is present cytoplasm. We denote the Hemiketal in the cytoplasm by BC and the Hemiketal in the vacuole by BV.

The partial differential equations that govern the diffusing species are as follows:

$$\frac{\partial A}{\partial t} = D_A \cdot \triangle\, A + G_A \frac{A^2 + A_0}{I + K} - U_A \cdot A \tag{2.165}$$

$$\frac{\partial I}{\partial t} = D_I \cdot \triangle\, I + G_I \cdot A^2 + I_0 - U_I \cdot I \tag{2.166}$$

$$\frac{\partial [BC]}{\partial t} = D_{BC} \cdot \triangle\, [BC] + \gamma u_{act(n,thr)}(A) - \delta [BC] - trcv[BC], \tag{2.167}$$

where $trcv$ is the transport rate from B in cytoplasm to vacuole. After anthocyanins are transported into the vacuole, we use the ODEs in Section 2.5 to find the concentrations of different species like A^-, A, AH^+, etc. Assuming all species will degrade with rate δ, we have the system of ordinary differential equations similar to Eq. 2.2 to Eq. 2.8, but adding a degradation term to each equation,

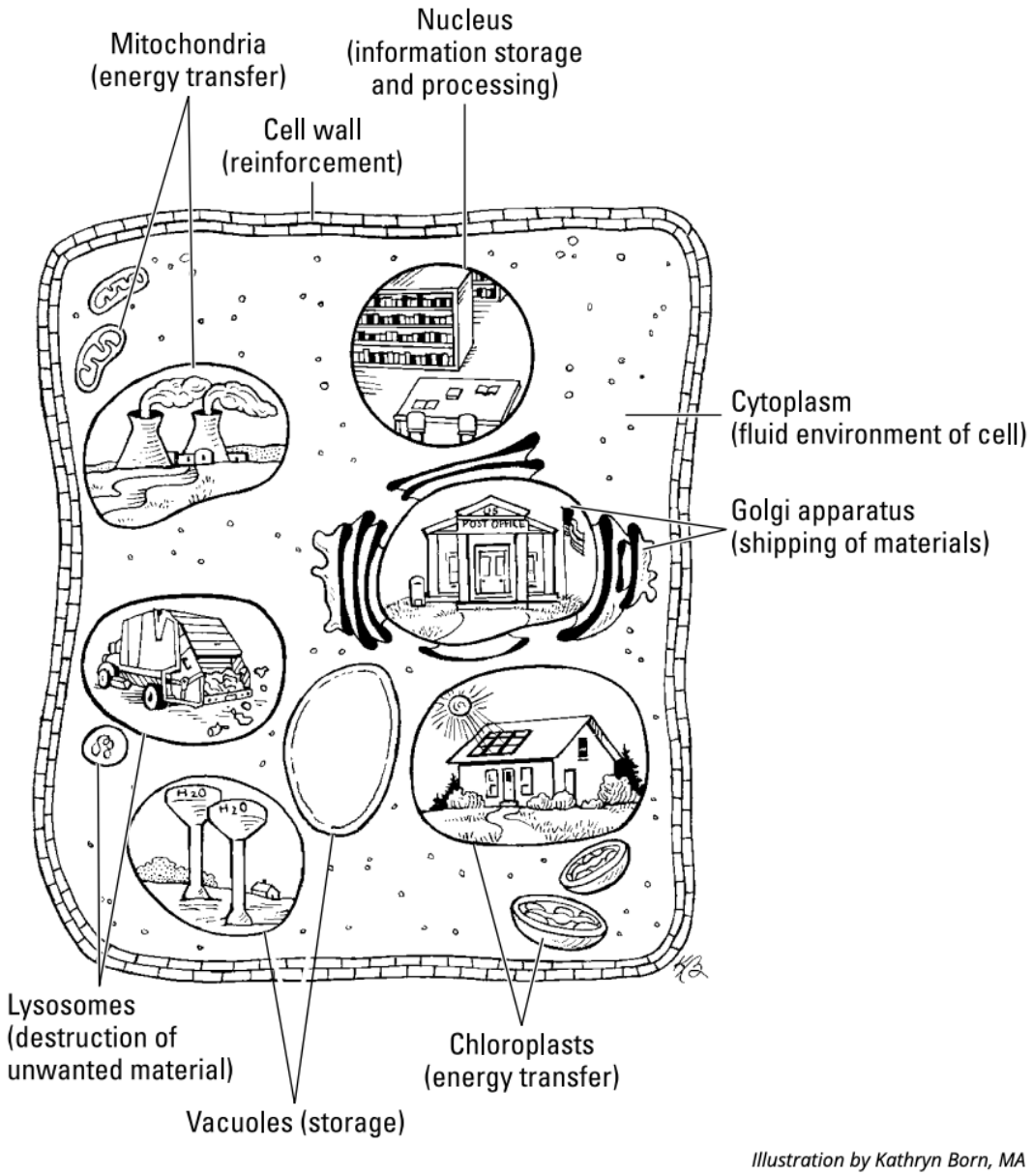

Figure 2.38: Structure of a plant cell. This images is taken from Ref. [57]. Anthocyanins are synthesized in the cytoplasm, which pH value is 7, and then transported to the vacuole, which pH value is between $3 - 6$.

the rate of change of B in vacuole is

$$\frac{d}{dt}[Bv] = trcv[BC] - \delta[BV] \tag{2.168}$$
$$- \{-k_3[AH^+] + k_{-3}[B][H^+]\} + \{-k_4[B] + k_{-4}[C]\} + \{-k_6[B] + k_{-6}[B^-][H^+]\}$$

For the self association species $(A^-)_{N1}$, A_{N2}, $(AH^+)_{N3}$, and $(A)_{N4/2} \cdot (AH^+)_{N4/2}$, we use Eq. 2.33 to Eq. 2.48 simulate the results.

In the following results, we have the following parameters:

1. The production potency: $\gamma = 5 \times 10^{-3}$.
2. The diffusion coefficients: $D_A = 0.01, D_I = 0.5, D_B = 10^{-2}$.
3. The association constants: $J_1 = 3200, J_2 = 12800, J_3 = 9600, J_4 = 11200$, and $j_{1,n} = j_{2,n} = j_{3,n} = j_{4,n} = 8000$, for all $n \in \{1, 2, \cdots, N\}$.
4. The kinetic constants: $k_1 = 3 \times 10^{3.2},\ k_{-1} = 3 \times 10^{10},\ k_2 = 3 \times 10^6$, $k_{-2} = 3 \times 10^{10}$, $k_3 = 0.2849,\ k_{-3} = 23.7,\ k_4 = 3 \times 10^5,\ k_{-4} = 3 \times 10^{5.98}$, $k_5 = 3 \times 10^{3.25},\ k_{-5} = 3 \times 10^{10},\ k_6 = 3 \times 10^{2.14},\ k_{-6} = 3 \times 10^{10}$.
5. The sigmoidal response power $n = 3$ with the threshold constant $\tau = 3$.
6. The degrade rate $\delta = 10^{-2}$
7. The length of time: $2 \times 10^5 \times 0.1$ seconds where a time step is 0.1.
8. The transport rate: $trcv = 0.5$.

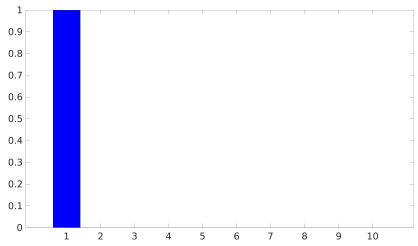

(a) A^- distribution up to 10th mer at the Max BC.

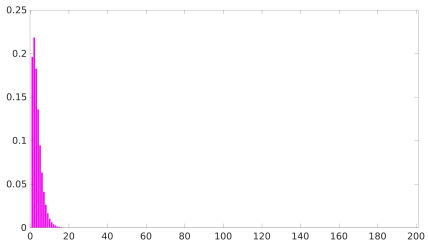

(b) A distribution up to 200th mer at the Max BC.

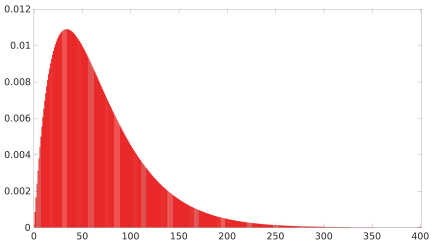

(c) AH^+ distribution up to 400th mer at the Max BC.

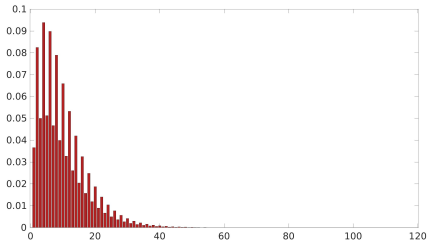

(d) $A \cdot AH^+$ distribution up to 120th mer at the Max BC.

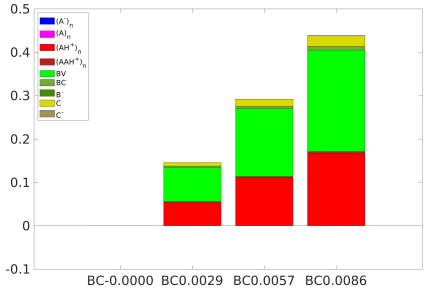

(e) Species distribution in different BC.

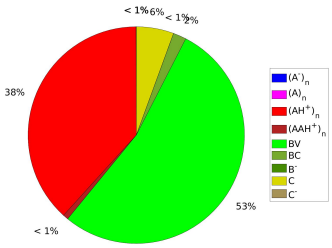

(f) Species distribution at the Max BC.

Figure 2.39: Anthocyanin species at time 2×10^4 seconds, resulting from simulations of the system (Eq. 2.165 to Eq. 2.168 and the association scheme Eq. 2.2 to Eq. 2.8) with parameter values as follows: The diffusion coefficients are $D_A = 0.01, D_I = 0.5$, the degradation rate constants are $U_A = 0.03,\ U_I = 0.03$, the background production rate constants are $A_0 = 0.01,\ I_0 = 0$, the activation potency rate constants are $G_A = 0.08,\ G_I = 0.12$, the production potency: $\gamma = 5 \times 10^{-3}$, the degrade rate $\delta = 10^{-2}$, and the transport rate $trcv = 0.5$ at pH$= 3.5$. The initial concentration of the activator is $1M$, and that of the inhibitor is $0M$. The spatial domain is $0 \leq x, y \leq 50$. The time step for the simulation was 0.01 seconds, and the spatial step size was $50/256$. The largest association numbers for A^-, A, AH^+, and $A \cdot AH^+$ are $10, 200, 400, 120$, respectively.

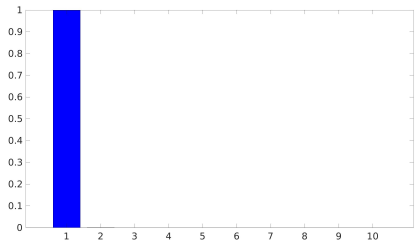

(a) A^- distribution up to 10th mer at the Max BC.

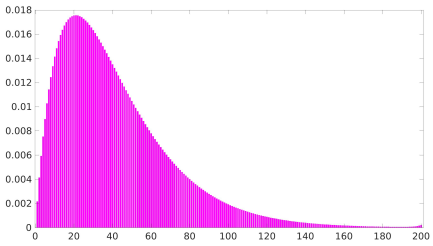

(b) A distribution up to 200th mer at the Max BC.

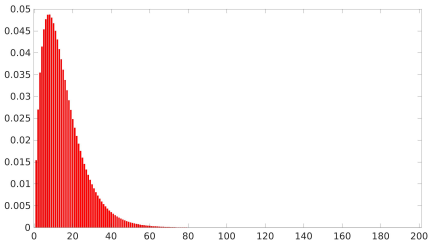

(c) AH^+ distribution up to 200th mer at the Max BC.

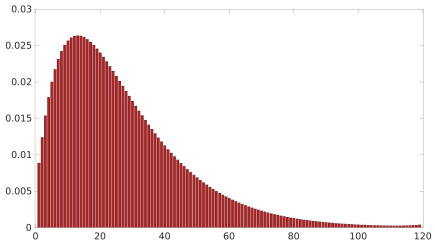

(d) $A \cdot AH^+$ distribution up to 120th mer at the Max BC.

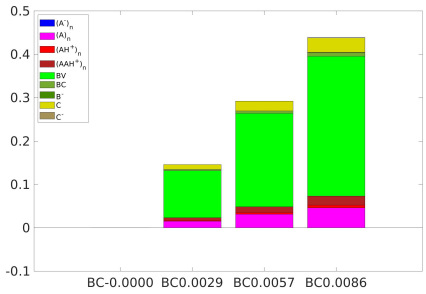

(e) Species distribution in different BC.

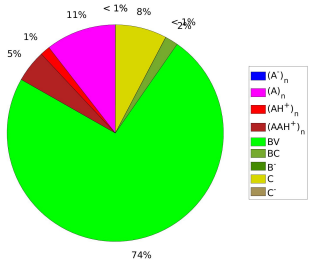

(f) Species distribution at the Max BC.

Figure 2.40: Anthocyanin species at time 2×10^4 seconds, resulting from simulations of the system (Eq. 2.165 to Eq. 2.168 and the association scheme Eq. 2.2 to Eq. 2.8) with parameter values as follows: The diffusion coefficients are $D_A = 0.01, D_I = 0.5$, the degradation rate constants are $U_A = 0.03,\ U_I = 0.03$, the background production rate constants are $A_0 = 0.01,\ I_0 = 0$, the activation potency rate constants are $G_A = 0.08,\ G_I = 0.12$, the production potency: $\gamma = 5 \times 10^{-3}$, the degrade rate $\delta = 10^{-2}$, and the transport rate $trcv = 0.5$ at pH$= 4$. The initial concentration of the activator is $1M$, and that of the inhibitor is $0M$. The spatial domain is $0 \leq x, y \leq 50$. The time step for the simulation was 0.01 seconds, and the spatial step size was $50/256$. The largest association numbers for A^-, A, AH^+, and $A \cdot AH^+$ are $10, 200, 200, 120$, respectively.

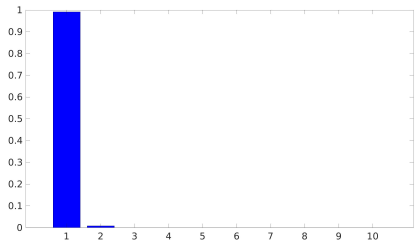

(a) A^- distribution up to 10th mer at the Max BC.

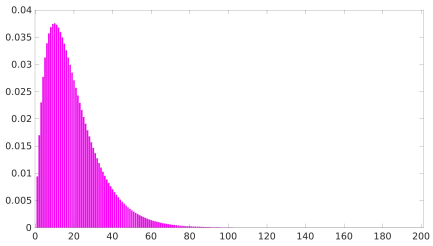

(b) A distribution up to 200th mer at the Max BC.

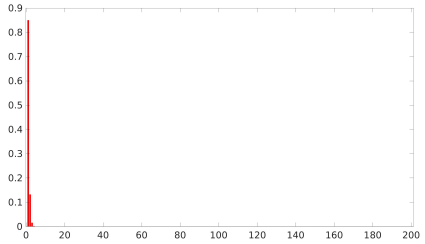

(c) AH^+ distribution up to 200th mer at the Max BC.

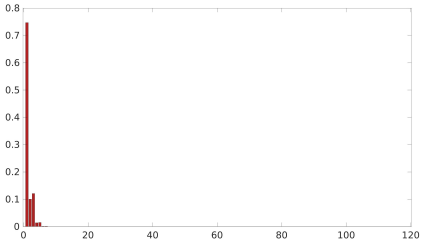

(d) $A \cdot AH^+$ distribution up to 120th mer at the Max BC.

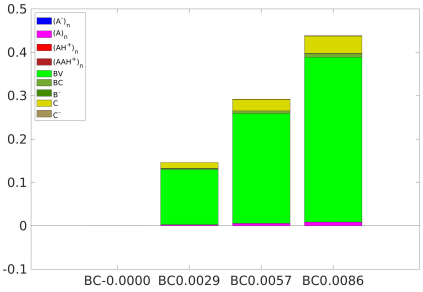

(e) Species distribution in different BC.

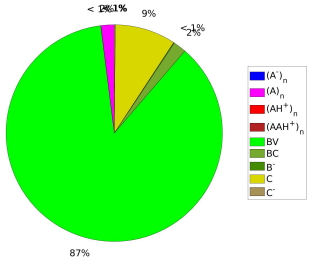

(f) Species distribution at the Max BC.

Figure 2.41: Anthocyanin species at time 2×10^4 seconds, resulting from simulations of the system (Eq. 2.165 to Eq. 2.168 and the association scheme Eq. 2.2 to Eq. 2.8) with parameter values as follows: The diffusion coefficients are $D_A = 0.01, D_I = 0.5$, the degradation rate constants are $U_A = 0.03,\ U_I = 0.03$, the background production rate constants are $A_0 = 0.01,\ I_0 = 0$, the activation potency rate constants are $G_A = 0.08,\ G_I = 0.12$, the production potency: $\gamma = 5 \times 10^{-3}$, the degrade rate $\delta = 10^{-2}$, and the transport rate $trcv = 0.5$ at pH$= 5$. The initial concentration of the activator is $1M$, and that of the inhibitor is $0M$. The spatial domain is $0 \leq x, y \leq 50$. The time step for the simulation was 0.01 seconds, and the spatial step size was $50/256$. The largest association numbers for A^-, A, AH^+, and $A \cdot AH^+$ are $10, 200, 200, 120$, respectively.

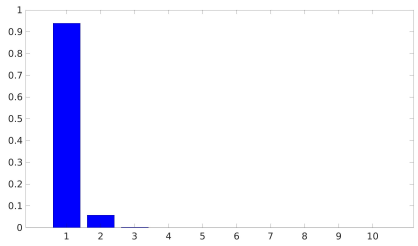

(a) A^- distribution up to 10th mer at the Max BC.

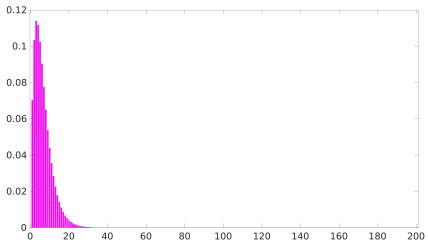

(b) A distribution up to 200th mer at the Max BC.

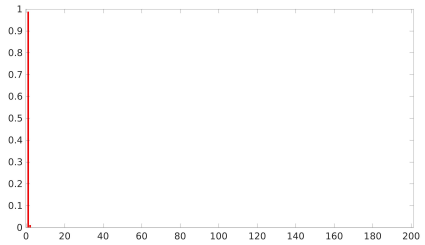

(c) AH^+ distribution up to 200th mer at the Max BC.

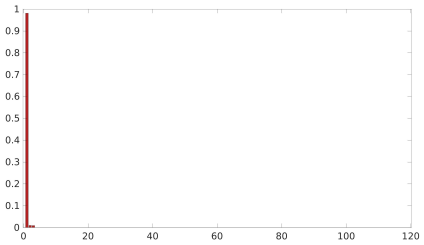

(d) $A \cdot AH^+$ distribution up to 120th mer at the Max BC.

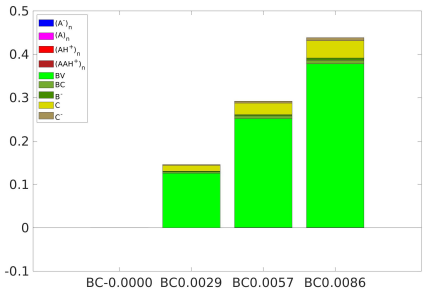

(e) Species distribution in different BC.

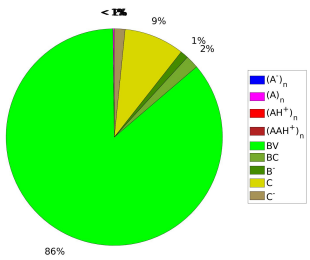

(f) Species distribution at the Max BC.

Figure 2.42: Anthocyanin species at time 2×10^4 seconds, resulting from simulations of the system (Eq. 2.165 to Eq. 2.168 and the association scheme Eq. 2.2 to Eq. 2.8) with parameter values as follows: The diffusion coefficients are $D_A = 0.01, D_I = 0.5$, the degradation rate constants are $U_A = 0.03,\ U_I = 0.03$, the background production rate constants are $A_0 = 0.01,\ I_0 = 0$, the activation potency rate constants are $G_A = 0.08,\ G_I = 0.12$, the production potency: $\gamma = 5 \times 10^{-3}$, the degrade rate $\delta = 10^{-2}$, and the transport rate $trcv = 0.5$ at pH$= 6$. The initial concentration of the activator is $1M$, and that of the inhibitor is $0M$. The spatial domain is $0 \leq x, y \leq 50$. The time step for the simulation was 0.01 seconds, and the spatial step size was $50/256$. The largest association numbers for A^-, A, AH^+, and $A \cdot AH^+$ are $10, 200, 200, 120$, respectively.

2.6.5 Binning method

Because we will have a large number of ordinary differential equations to to solve in order to simulate more realistic results for large association constants, we will employ a binning method to reduce the total number of the equations. Essentially, we group several m-mers together into a "bin" and assume that each mer in a bin has the same concentration. For $(A^-)_n$, $(A)_n$, $(AH^+)_n$, we set the monomer to be the first bin group, denoted by $(A^-)Bin_1$, $(A)Bin_1$, and $(AH^+)Bin_1$, respectively. Assume the size of other bin groups is n, which is an even number, we have the ℓth group is binning from $[(\ell-2)\times n+2]$mer to $[(\ell-1)\times n+1]$mer, denoted by Bin_ℓ. For the $A\cdot AH^+$, the first bin group is binning from $A\cdot AH^+$ to $(A)_{\frac{n}{2}}\cdot(AH^+)_{\frac{n}{2}}{}^+{}_1$, and its ℓth group is binning from $(A)_{\frac{(\ell-1)n}{2}+1}\cdot(AH^+)_{\frac{(\ell-1)n}{2}+1}$ to $(A)_{\frac{\ell n}{2}}\cdot(AH^+)_{\frac{\ell n}{2}+1}$. Also assume $j_{i,\pm2}=j_{i,\pm3}=\cdots=j_{i,\pm(n+1)}\doteq\widetilde{j_{i,\pm2}},\cdots,j_{i,\pm((\ell-2)\times n+2)}=\cdots=j_{i,\pm((\ell-1)\times n+1)}\doteq\widetilde{j_{i,\pm\ell}}$, for $i=1,2,3$ and $\ell=3,4,\cdots,m_i$ if the number of the binning group is m_i. For $A\cdot AH^+$ association, we assume $j_{4,\pm2}=j_{4,\pm3}=\cdots=j_{4,\pm(n+1)}\doteq\widetilde{j_{4,\pm1}},\cdots,j_{4,\pm((\ell-1)\times n+2)}=\cdots=j_{4,\pm((\ell)\times n+1)}\doteq\widetilde{j_{4,\pm\ell}}$, for $\ell=2,3,\cdots,m$ if the number of the binning group is m_4.

Then Eq. 2.33 to Eq. 2.35 become

$$
\begin{aligned}
\frac{d}{dt}[(A^-)Bin_1] =& \{-k_{-1}[(A^-)Bin_1][H^+] + k_1[(A)Bin_1]\} \\
&+ 2\{-j_{1,2}[(A^-)Bin_1][(A^-)Bin_1] + j_{1,-2} \times \frac{1}{n}[(A^-)Bin_2]\} \\
&+ \{-j_{1,3}[(A^-)Bin_1]\frac{1}{n}[(A^-)Bin_2] + j_{1,-3} \times \frac{1}{n}[(A^-)Bin_2]\} \\
&+ \cdots \\
&+ \{-j_{1,(m_1-1)n+1}[(A^-)Bin_1]\frac{1}{n}[(A^-)Bin_{m_1}] \\
&+ j_{1,-((m_1-1)n+1)}\frac{1}{n}[(A^-)Bin_{m_1}]\} \\
&- \delta[(A^-)Bin_1] \\
=& \{-k_{-1}[(A^-)Bin_1][H^+] + k_1[(A)Bin_1]\} \\
&+ 2\{-\widetilde{j_{1,2}}[(A^-)Bin_1][(A^-)Bin_1] + \widetilde{j_{1,-2}} \times \frac{1}{n}[(A^-)Bin_2]\} \\
&- [(A^-)Bin_1]\left(\sum_{\ell=2}^{m_1}\frac{n-1}{n}\widetilde{j_{1,\ell}}[(A^-)Bin_\ell] + \sum_{\ell=2}^{m_1-1}\frac{1}{n}\widetilde{j_{1,(\ell+1)}}[(A^-)Bin_\ell]\right) \\
&+ \sum_{\ell=2}^{m_1}\widetilde{j_{1,-\ell}}[(A^-)Bin_\ell] - \frac{1}{n}\widetilde{j_{1,-2}}[(A^-)Bin_2] - \delta[(A^-)Bin_1] \\
\frac{d}{dt}[(A^-)Bin_2] =& -\{-\widetilde{j_{1,2}}[(A^-)Bin_1][(A^-)Bin_1] + \widetilde{j_{1,-2}}\frac{1}{n}[(A^-)Bin_2]\} \\
&+ \{-\widetilde{j_{1,3}}[(A^-)Bin_1]\frac{1}{n}[(A^-)Bin_2] + \widetilde{j_{1,-3}}\frac{1}{n}[(A^-)Bin_3]\} \\
&- \delta[(A^-)Bin_2] \\
&\vdots \\
\frac{d}{dt}[(A^-)Bin_\ell] =& -\{-\widetilde{j_{1,\ell}}[(A^-)Bin_1]\frac{1}{n}[(A^-)Bin_{(\ell-1)}] + \widetilde{j_{1,-\ell}}\frac{1}{n}[(A^-)Bin_\ell]\} \\
&+ \{-\widetilde{j_{1,(\ell+1)}}[(A^-)Bin_1]\frac{1}{n}[(A^-)Bin_\ell] + \widetilde{j_{1,-(\ell+1)}}\frac{1}{n}[(A^-)Bin_{(\ell+1)}]\} \\
&- \delta[(A^-)Bin_\ell] \\
&\vdots \\
\frac{d}{dt}[(A^-)Bin_{m_1}] =& -\{-\widetilde{j_{1,m_1}}[(A^-)Bin_1]\frac{1}{n}[(A^-)Bin_{(m_1-1)}] + \widetilde{j_{1,-m_1}}\frac{1}{n}[(A^-)Bin_{m_1}]\} \\
&- \delta[(A^-)Bin_{m_1}].
\end{aligned}
$$

Eq. 2.37 becomes

$$
\begin{aligned}
\frac{d}{dt}[(A)Bin_1] = &- \{-k_{-1}[(A^-)Bin_1][H^+] + k_1[(A)Bin_1]\} \\
&+ \{-k_{-2}[(A)Bin_1][H^+] + k_2[(AH^+)Bin_1]\} \\
&+ 2\{-\widetilde{j_{2,2}}[(A)Bin_1][(A)Bin_1] + \widetilde{j_{2,-2}}\frac{1}{n}[(A)Bin_2]\} \\
&- [(A)Bin_1]\left(\sum_{\ell=2}^{m_2}\frac{n-1}{n}\widetilde{j_{2,\ell}}[(A)Bin_\ell] + \sum_{\ell=2}^{m_2-1}\frac{1}{n}\widetilde{j_{2,(\ell+1)}}[(A)Bin_\ell]\right) \\
&+ \sum_{\ell=2}^{m_2}\widetilde{j_{2,-\ell}}[(A)Bin_\ell] - \widetilde{j_{2,-2}}\frac{1}{n}[(A)Bin_2] \\
&+ \{-\widetilde{j_{4,2}}[(A)Bin_1][(AH^+)Bin_1] + j_{4,-2}\frac{1}{n}[(A\cdot AH^+)Bin_1]\} \\
&+ \{-j_{4,4}[(A)Bin_1]\frac{1}{n}[(A\cdot AH^+)Bin_1] + j_{4,-4}\frac{1}{n}[(A\cdot AH^+)Bin_1]\} \\
&+ \cdots \\
&+ \{-j_{4,(m_4)n}[(A)Bin_1]\frac{1}{n}[(A\cdot AH^+)Bin_{m_4}] \\
&+ j_{4,-((m_4)n)}[\frac{1}{n}[(A\cdot AH^+)Bin_{m_4}]\} \\
&- \delta[(A)Bin_1].
\end{aligned}
$$

That is,

$$
\begin{aligned}
\frac{d}{dt}[(A)Bin_1] = & -\{-k_{-1}[(A^-)Bin_1][H^+] + k_1[(A)Bin_1]\} \\
& + \{-k_{-2}[(A)Bin_1][H^+] + k_2[(AH^+)Bin_1]\} \\
& + 2\{-\widetilde{j_{2,2}}[(A)Bin_1][(A)Bin_1] + \widetilde{j_{2,-2}}\frac{1}{n}[(A)Bin_2]\} \\
& - [(A)Bin_1]\times \\
& \left(\sum_{\ell=2}^{m_2}\frac{n-1}{n}\widetilde{j_{2,\ell}}[(A)Bin_\ell] + \sum_{\ell=2}^{m_2-1}\frac{1}{n}\widetilde{j_{2,(\ell+1)}}[(A)Bin_\ell]\right) \\
& + \sum_{\ell=2}^{m_2}\widetilde{j_{2,-\ell}}[(A)Bin_\ell] - \widetilde{j_{2,-2}}\frac{1}{n}[(A)Bin_2] \\
& - \widetilde{j_{4,2}}[(A)Bin_1][(AH^+)Bin_1] \\
& - [(A)Bin_1]\times \\
& \left(\sum_{\ell=1}^{m_4}(\frac{1}{2}-\frac{1}{n})\widetilde{j_{4,\ell}}[(A\cdot AH^+)Bin_\ell] + \sum_{\ell=2}^{m_4}\frac{1}{n}\widetilde{j_{4,\ell}}[(A\cdot AH^+)Bin_{(\ell-1)}]\right) \\
& + \sum_{\ell=1}^{m_4}\frac{1}{2}\widetilde{j_{4,-\ell}}[(A\cdot AH^+)Bin_\ell] \\
& - \delta[(A)Bin_1].
\end{aligned}
$$

Eq. 2.38 to Eq. 2.39 become

$$\begin{aligned}
\frac{d}{dt}[(A)Bin_2] =& -\{-\widetilde{j_{2,2}}[(A)Bin_1][(A)Bin_1] + \widetilde{j_{2,-2}}\frac{1}{n}[(A)Bin_2]\} \\
&+\{-\widetilde{j_{2,3}}[(A)Bin_1]\frac{1}{n}[(A)Bin_2] + \widetilde{j_{2,-3}}\frac{1}{n}[(A)Bin_3]\} - \delta[(A)Bin_2] \\
&\vdots \\
\frac{d}{dt}[(A)Bin_\ell] =& -\{-\widetilde{j_{2,\ell}}[(A)Bin_1]\frac{1}{n}[(A)Bin_{(\ell-1)}] + \widetilde{j_{2,-\ell}}\frac{1}{n}[(A)Bin_\ell]\} \\
&+\{-\widetilde{j_{2,\ell+1}}[(A)Bin_1]\frac{1}{n}[(A)Bin_\ell] + \widetilde{j_{2,-(\ell+1)}}\frac{1}{n}[(A)Bin_{(\ell+1)}]\} \\
&-\delta[(A)Bin_\ell] \\
&\vdots \\
\frac{d}{dt}[(A)Bin_{m_2}] =& -\{-\widetilde{j_{2,m_2}}[(A)Bin_1]\frac{1}{n}[(A)Bin_{(m_2-1)}] + \widetilde{j_{2,m_2}}\frac{1}{n}[(A)Bin_{m_2}]\} \\
&-\delta[(A)Bin_{m_2}].
\end{aligned}$$

Eq. 2.41 becomes

$$\begin{aligned}
\frac{d}{dt}[(AH^+)Bin_1] = &- \{-k_{-2}[(A)Bin_1][H^+] + k_2[(AH^+)Bin_1]\} \\
&+ \{-k_3[(AH^+)Bin_1] + k_{-3}[B][H^+]\} \\
&+ 2\{-\widetilde{j_{3,2}}[(AH^+)Bin_1][(AH^+)Bin_1] + \widetilde{j_{3,-2}}\frac{1}{n}[(AH^+)Bin_2]\} \\
&- [(AH^+)Bin_1]\times \\
&\left(\sum_{\ell=2}^{m_3}\frac{n-1}{n}\widetilde{j_{3,\ell}}[(AH^+)Bin_\ell] + \sum_{\ell=2}^{m_3-1}\frac{1}{n}\widetilde{j_{3,(\ell+1)}}[(AH^+)Bin_\ell]\right) \\
&+ \sum_{\ell=2}^{m_3}\widetilde{j_{3,-\ell}}[(AH^+)Bin_\ell] - \widetilde{j_{3,-2}}\frac{1}{n}[(AH^+)Bin_2] \\
&- \widetilde{j_{4,2}}[(A)Bin_1][(AH^+)Bin_1] + \widetilde{j_{4,-2}}\frac{1}{n}[(A\cdot AH^+)Bin_1] \\
&- [(AH^+)Bin_1]\sum_{\ell=1}^{m_4}\frac{1}{2}\widetilde{j_{4,\ell}}[(A\cdot AH^+)Bin_\ell] \\
&+ \sum_{\ell=1}^{m_4}\frac{1}{2}\widetilde{j_{4,-\ell}}[(A\cdot AH^+)Bin_\ell] \\
&- \delta[(AH^+)Bin_1].
\end{aligned}$$

Eq. 2.42 to Eq. 2.43 become

$$
\begin{aligned}
\frac{d}{dt}[(AH^+)Bin_2] =& -\{-\widetilde{j_{3,2}}[(AH^+)Bin_1][(AH^+)Bin_1] + \widetilde{j_{3,-2}}\frac{1}{n}[(AH^+)Bin_2]\} \\
&+\{-\widetilde{j_{3,3}}[(AH^+)Bin_1]\frac{1}{n}[(AH^+)Bin_2] + \widetilde{j_{3,-3}}\frac{1}{n}[(AH^+)Bin_3]\} \\
&-\delta[(AH^+)Bin_2] \\
&\vdots \\
\frac{d}{dt}[(AH^+)Bin_\ell] =& -\{-\widetilde{j_{3,\ell}}[(AH^+)Bin_1]\frac{1}{n}[(AH^+)Bin_{(\ell-1)}] + \widetilde{j_{3,-\ell}}\frac{1}{n}[(AH^+)Bin_\ell]\} \\
&+\{-\widetilde{j_{3,(\ell+1)}}[(AH^+)Bin_1]\frac{1}{n}[(AH^+)Bin_\ell] + \widetilde{j_{3,-(\ell+1)}}\frac{1}{n}[(AH^+)Bin_{(\ell+1)}]\} \\
&-\delta[(AH^+)Bin_\ell] \\
&\vdots \\
\frac{d}{dt}[(AH^+)Bin_{m_3}] =& -\{-\widetilde{j_{3,m_3}}[(AH^+)Bin_1]\frac{1}{n}[(AH^+)Bin_{(m_3-1)}] + \widetilde{j_{3,-m_3}}\frac{1}{n}[(AH^+)Bin_{m_3}]\} \\
&-\delta[(AH^+)Bin_{m_3}].
\end{aligned}
$$

Eq. 2.45 to Eq. 2.48 become

$$
\begin{aligned}
\frac{d}{dt}[(A\cdot AH^+)Bin_1] =& -\{-\widetilde{j_{4,1}}[(A)Bin_1][(AH^+)Bin_1] + \widetilde{j_{4,-1}}\frac{1}{n}[(A\cdot AH^+)Bin_1]\} \\
&+\{-\widetilde{j_{4,2}}\frac{1}{n}[(A\cdot AH^+)Bin_1][(AH^+)Bin_1] + \widetilde{j_{4,-2}}\frac{1}{n}[(A\cdot AH^+)Bin_2]\} \\
&-\delta[(A\cdot AH^+)Bin_1] \\
&\vdots \\
\frac{d}{dt}[(A\cdot AH^+)Bin_\ell] =& -\{-\widetilde{j_{4,\ell}}\frac{1}{n}[(A)Bin_1][(A\cdot AH^+)Bin_{(\ell-1)}] + \widetilde{j_{4,-\ell}}[(A\cdot AH^+)Bin_\ell]\} \\
&+\{-\widetilde{j_{4,(\ell+1)}}\frac{1}{n}[(A)Bin_1][(A\cdot AH^+)Bin_\ell] \\
&+\widetilde{j_{4,-(\ell+1)}}\frac{1}{n}[(A\cdot AH^+)Bin_{(\ell+1)}]\} \\
&-\delta[(A\cdot AH^+)Bin_\ell] \\
&\vdots \\
\frac{d}{dt}[(A\cdot AH^+)Bin_{m_4}] =& -\{-\widetilde{j_{4,m_4}}\frac{1}{n}[(A)Bin_1][(A\cdot AH^+)Bin_{(m_4-1)}] \\
&+\widetilde{j_{4,-m_4}}\frac{1}{n}[(A\cdot AH^+)Bin_{m_4}]\} \\
&-\delta[(A\cdot AH^+)Bin_{m_4}] \\
&.
\end{aligned}
$$

Using this method, we can compute an approximation of the m-mer distribution even with the largest m-mer being large, on the order of a thousand-mer. Sample populations size distributions are shown in Figure 2.43 and Figure 2.44.

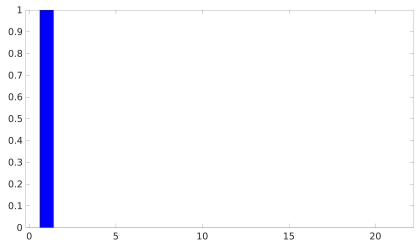

(a) A^- distribution up to 40th mer at the Max BC.

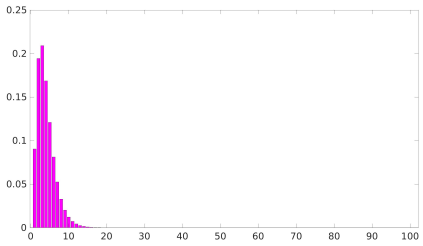

(b) A distribution up to 200th mer at the Max BC.

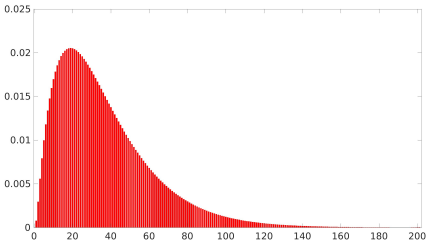

(c) AH^+ distribution up to 400th mer at the Max BC.

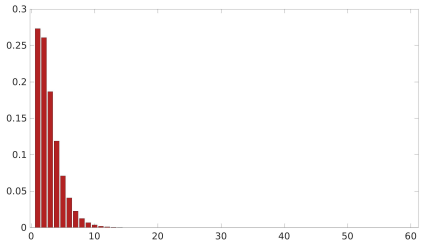

(d) $A \cdot AH^+$ distribution up to 120th mer at the Max BC.

Figure 2.43: Anthocyanin species at time 2×10^4 seconds, resulting from simulations of the system given by Eqns. 2.165 to 2.168 and the association scheme given by Eqns. 2.2 to 2.8) with parameter values as follows: The binning size:2, the diffusion coefficients are $D_A = 0.01, D_I = 0.5$, the degradation rate constants are $U_A = 0.03,\ U_I = 0.03$, the background production rate constants are $A_0 = 0.01,\ I_0 = 0$, the activation potency rate constants are $G_A = 0.08,\ G_I = 0.12$, the production potency: $\gamma = 5 \times 10^{-3}$, the degrade rate $\delta = 10^{-2}$, and the transport rate $trcv = 0.5$ at pH= 3.5. The initial concentration of the activator is $1M$, and that of the inhibitor is $0M$. The spatial domain is $0 \leq x, y \leq 50$. The time step for the simulation was 0.01 seconds, and the spatial step size was $50/256$. The largest association numbers for A^-, A, AH^+, and $A \cdot AH^+$ are $10, 200, 400, 120$, respectively.

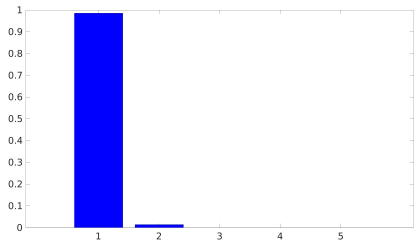

(a) A^- distribution up to 40th mer at the Max BC.

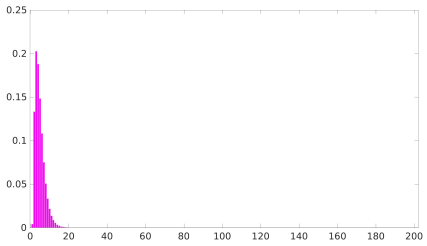

(b) A distribution up to 2000th mer at the Max BC.

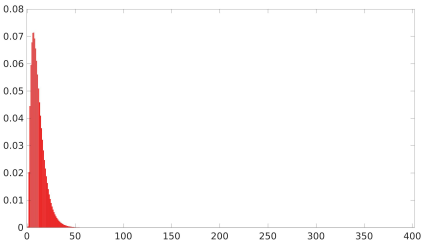

(c) AH^+ distribution up to 4000th mer at the Max BC.

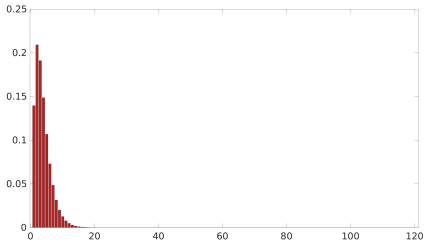

(d) $A \cdot AH^+$ distribution up to 1200th mer at the Max BC.

Figure 2.44: Anthocyanin species at time 2×10^4 seconds, resulting from simulations of the system (Eq. 2.165 to Eq. 2.168 and the association scheme Eq. 2.2 to Eq. 2.8) with parameter values as follows: The binning size:10, the diffusion coefficients are $D_A = 0.01, D_I = 0.5$, the degradation rate constants are $U_A = 0.03,\ U_I = 0.03$, the background production rate constants are $A_0 = 0.01,\ I_0 = 0$, the activation potency rate constants are $G_A = 0.08,\ G_I = 0.12$, the production potency: $\gamma = 5 \times 10^{-3}$, the degrade rate $\delta = 10^{-2}$, and the transport rate $trcv = 0.5$ at pH$= 3.5$. The association constants are 10 times the original association constants 2.32. The initial concentration of the activator is $1M$, and that of the inhibitor is $0M$. The spatial domain is $0 \leq x, y \leq 50$. The time step for the simulation was 0.01 seconds, and the spatial step size was $50/256$. The largest association numbers for A^-, A, AH^+, and $A \cdot AH^+$ are $40, 2000, 4000, 1200$, respectively.

2.7 Conclusions and Further Work

The Gierer-Meinhardt model has long been applied to study pattern formation in biological systems [41]. Some studies have analyzed the stability of those models [39, 58, 59]. Our focus in this dissertation has been the modified Gierer-Meinhardt model, proposed in [31], which allows the inhibitor to be zero as the initial condition. Our analysis of the modified Gierer-Meinhardt model has revealed well-ordered patterns of rolls, up- and down-hexagons, as well as transient squares. The nonlinear amplitude equation analysis in Section 2.6 has probed the competition between rolls and up- and down-hexagons when the parameters determining a cubic coefficient γ_1 in the amplitude equations is positive. Further work, described at the end of Section 2.6, will further investigate the roll-hexagon-square competition if $\gamma_1 < 0$.

The modified Gierer-Meinhardt model [31] only deals with the activator and inhibitor. We extend this model to activate the anthocyanin synthesis. By [40], the dependence of production rate on activator production typically follows a sigmoidal relationship $u_{act}(A; n, \tau) = \frac{A^n}{A^n+\tau^n}$. We adopt this relation and assume the activator activate the Hemiketal B in the cytoplasm, and we also allow B in the cytoplasm to diffuse with the same rate as the activator. The Hemiketal B can transport across the vacuolar membrane into the vacuole. Once the anthocyanins are in the vacuole, they will follow the pH-dependent scheme 2.1 with self associations 2.30 and 2.31.

Chapter 3

Surfaces of prescribed mean curvature: A hodograph approach to the mean-curvature equation

3.1 Introduction and outline

Having developed and analyzed models for anthocyanin association in Chapter 2, we are heading towards using these models as part of a method for determining absorptivities of anthocyanin monomers, dimers, and trimers that will be the focus of our attention in Chapter 4. As outlined in Chapter 1 and described in more detail in Section 3.2 and Chapter 4, our method requires sufficient numbers of measurements of absorbance spectra of anthocyanin solutions at low concentrations. As described in more detail in Section 3.2, this chapter is connected with that aim through a proposed method of using the mean curvature of a droplet of anthocyanin solution resting on a surface to help determine the concentration of anthocyanin in the solution.

A surface embedded in $\mathbb{R}^3 = \{(x_1, x_2, x_3) \ : \ x_i \in \mathbb{R}\}$ may locally be described as a graph

$$(x_1, x_2, h(x_1, x_2)) \tag{3.1}$$

of a function $h(x_1, x_2)$ over the (x_1, x_2)-plane. In this section, we study the following problem: Given a function $H(x_1, x_2)$, find a function $h(x_1, x_2)$ for which the surface given by Eq. 3.1 has mean curvature $H(x_1, x_2)$. This problem is linked to the theme of this thesis, namely mathematical modeling of topics in anthocyanin chemistry, through the fact that the surface tension of a liquid droplet is proportional to the mean curvature of that droplet, and that droplet may be an anthoycanin solution.

This chapter is organized as follows: Motivation for studying the mean curvature of droplets in the context of this thesis is described in more detail in Section 3.2. In Section 3.3, we derive the mean-curvature equation (MCE). This is the following nonlinear partial differential equation for

the function $h(x_1, x_2)$:

$$\frac{1}{2}\frac{h_{x_1x_1}(h_{x_2}^2+1) - 2h_{x_1x_2}h_{x_1}h_{x_2} + h_{x_2x_2}(h_{x_1}^2+1)}{(h_{x_1}^2+h_{x_2}^2+1)^{\frac{3}{2}}} = H(x_1, x_2), \tag{3.2}$$

where $H(x_1, x_2)$ is the mean curvature of the surface given by Eq. 3.1. In Section 3.4, we develop a new approach to solving the mean-curvature equation that consists of first performing a hodograph transformation (which interchanges the independent and dependent variables) and then making use of the fact that the resulting equation separates – well, in general, almost separates– in polar coordinates. This approach has the potential to provide formulas for large classes of equations of prescribed mean curvature, but in this thesis we restrict to the case of finding surfaces of revolution for which the prescribed mean curvature $H(x_1, x_2) = H(r = x_1^2 + x_2^2)$ is a function of radius alone and the transformed equation does completely separate in polar coordinates. We show that the method we propose allows for the finding conformal parameterizations of these surfaces. A surface $\vec{r}(u_1, u_2) : \Omega \subset \mathbb{R}^2 \to \mathbb{R}^3$ is *conformally parameterized* if it satisfies the conditions that it be orthogonally parameterized ($\vec{r}_{u_1} \cdot \vec{r}_{u_2} = 0$) and that locally the stretching in both directions of parameterization are equal ($\vec{r}_{u_1} \cdot \vec{r}_{u_1} = \vec{r}_{u_2} \cdot \vec{r}_{u_2}$).

3.2 Motivation: Droplets of anthocyanin solution

Recent work by S. Thompson has convinced us to interpret the self associative behavior of anthocyanins to be that of lyotropic chromonic mesogens (liquid crystals) [60]- [61]. Mesogens are molecules with a hydrophobic component (for anthocyanins, the three-ring chromophore of the flavylium cation) together with hydrophilic groups (for anthocyanins, the sugar group additions). The hydrophobic aromatic chromophore with an ether link (-O-) to hydrophilic glucose gives unusual fluid-flow arrangements in a protic solvent. Surface activity, rheological experiments, and the deposition and drying dynamics of anthoyanin solution droplets at different concentrations and pH values all point to mesogenic carbohydrate features. The evaporative drying of 2-50 μL drops placed on FEP film on a temperature-control device placed on the stage of a LED and fluorescence

microscope (with illumination from below and above and a variety of accessory polarizers) gave very unusual, complex color and deposition patterns. The phase behavior, morphological arrangements, spatial and temporal color changes and fluorescence were all characteristics typical of those observed on drying chromonic liquid crystal droplets [62]. Experiments carried out at different pH values show dramatic nucleation and growth (association) patterns which are different for each of the species in the scheme and different for added copigments and solvents. The kinetics of the (slow) conversion of chalcones and hemiketals B to AH^+ and A was accelerated as the anthocyanin concentrations increased during the evaporative drying.

Coarse-grained models of intramolecular interactions in a chromonic liquid crystal in water show that a correct hydrophobic-hydrophilic balance is essential for association of monomers and their self-organization into liquid-crystal phases to occur [63].

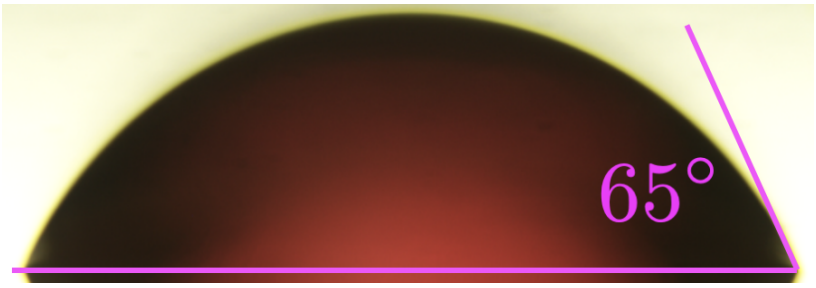

Figure 3.1: Droplet of aqueous *Mallow sylvestris* anthocyanin extract.

The addition of information about phase change processes to the mathematical analysis of the anthocyanin scheme is a fundamental way to make sense of the incredible variety of optical properties and biological functioning of plant systems. The mesogenic properties of anthocyanin monomers and associated species induce changes in interfacial free energies that also have potential consequences for their biological functioning. These considerations motivate us to pursue a geometric method to obtain information on interfacial free-energy changes by observing the shapes of droplets of anthocyanin solutions on surfaces or suspended between two surfaces (liquid bridges [64]). Preliminary experiments by S. Thompson on contact angles of anthocyanin solutions on surfaces have been carried out with a stereomicroscope optics held at 90° to the drop sample.

Figure 3.1 shows a droplet of an anthocyanin extract from mallow flowers on an FEP (fluorinated ethylene propylene) surface. The contact angle (marked in the figure) is $65°$, much less than the *ca.* $110°$ angle of a water droplet on FEP. The Young-Laplace equation relates the interfacial energies γ_{ij}, $i, j \in \{S, V, L\}$ between the solid (S), liquid (L) and surrounding vapor (V) to the contact angle θ of a liquid droplet on a solid surface by $\cos(\theta) = (\gamma_{SV} - \gamma_{SL})/\gamma_{LV}$. The reduced contact angle in Figure 3.1 results from the decreased surface tension as the mesogenic anthocyanins act similarly to soap in water.

The shape of a liquid droplet, assuming that the effect of gravity is negligible (a good assumption for small droplets [65]), is spheroidal. The spheroidal shape may be seen mathematically as a solution to the mean-curvature equation: Let the surface of the droplet be the graph of a function $h(x_1, x_2)$ over the solid surface. Then, $h(x_1, x_2)$ satisfies the mean-curvature equation, where the mean curvature of the droplet is proportional to the surface tension. The surface tension ν is typically considered to be constant, so that the function $H(x_1, x_2)$ in Eq. 3.2 is constant. The same equation applies in the case of liquid bridges, in which a liquid is suspended between two plates [64]. Fig. 3.2 (a,b) shows diagrams of liquid bridges from Ref. [64]. The shape of the liquid bridge depends on the volume of liquid, the surface tension, and the distance between the plates. But, in general, it is a surface of revolution of constant mean curvature. The surfaces in Fig. 3.2 (a,b) are portions of a class of such surfaces called *unduloids*. We will meet unduloids and their relatives (the so-called *Delaunay surfaces*) more intimately in Sec. 3.4.

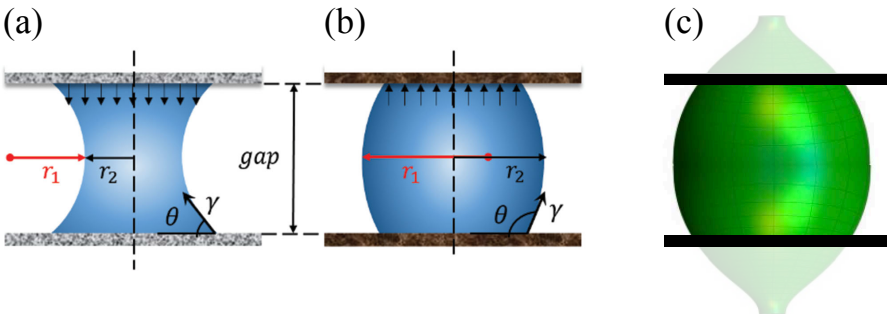

Figure 3.2: Liquid bridges as suspensions of liquid between two plates: Panels (a) and (b) are diagrams of liquid bridges from Ref. [64]. Panel (c) shows how these liquid bridges are portions of a class of surface of revolution of constant mean curvature, the *unduloid*, graphed in green.

In the case of an evaporating anthocyanin solution, we expect that self association occurring at the solid-liquid interface if the solid is, for example, glass, will lead to the quicker formation of associated species at the liquid surface near the contact with the solid. This may induce a spatially-dependent surface tension ν and therefore a spatially-dependent mean curvature H. The long-term goal is to combine information from components of this thesis, namely simulations of our equations for anthocyanin association, and insights from solutions to the mean-curvature equation, with observations of shapes of anthocyanin solution droplets at various concentrations and pH values, in order to infer information regarding anthocyanin association from shapes of anthocyanin droplets. We have made attempts at the relevant experimental observations. An example, in which we create a nonuniform surface tension by combing a droplet of water and a droplet of water with glycerin, is shown in Fig. 3.3. We learned that obtaining accurate experimental observations is difficult!: For example, to realize our goal, we need to be able to more carefully control for the volume of the droplets and be able to create plates that are nearly parallel. Therefore, we are not able to provide the final combination of theory and experimental results in this thesis. For the dynamically changing shapes of evaporating anthocyanin droplets, we expect to need to also account for mechanisms of solute transport in the droplet as the solution evaporates [66].

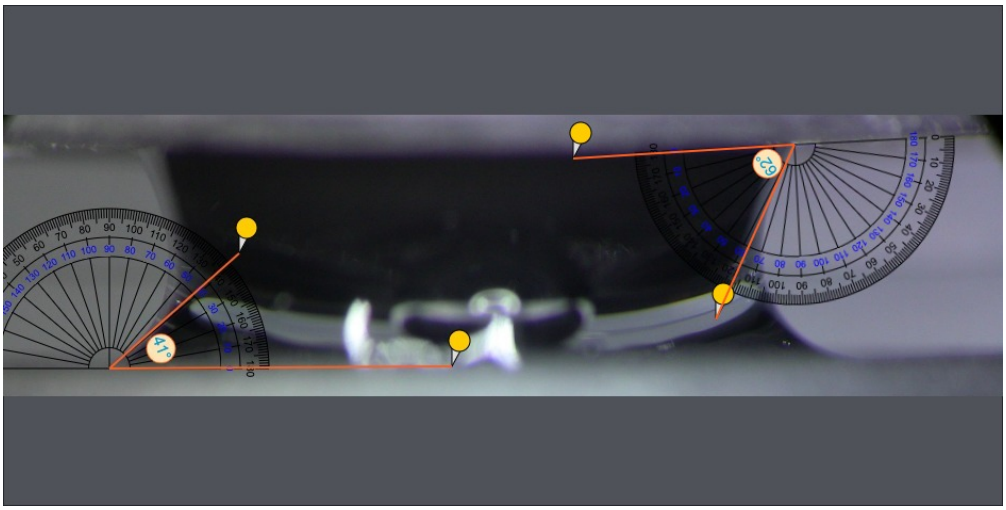

Figure 3.3: Liquid bridge which has a solution of water with glycerin at the top and water on the bottom. This is prototype of the type of experiment described in the the text.

3.3 Derivation of the Mean-curvature Equation

Writing $\mathbb{R}^2 = \{(x_1, x_2) \ : \ x_i \in \mathbb{R}\}$, and $\mathbb{R}^3 = \{(u_1, u_2, u_3) \ : \ u_i \in \mathbb{R}\}$, the problem of interest is to find, given a function $H(x_1, x_2)$, a surface $\vec{r} : \Omega \subset \mathbb{R}^2 \to \mathbb{R}^3$ embedded in $\mathbb{R}^3$ with mean curvature $H(x_1, x_2)$. We assume the surface to be a graph

$$\vec{r}(x_1, x_2) = (u_1 = x_1, u_2 = x_2, u_3 = h(x_1, x_2)) \tag{3.3}$$

of a function $h(x_1, x_2)$ over the (x_1, x_2)-plane. The mean curvature of the surface Eq. 3.1 may be written as a nonlinear partial differential equation (PDE) for $h(x_1, x_2)$, the mean-curvature equation, stated above as Eq. 3.2. The purpose of this section is to derive that equation.

The mean curvature of a surface is defined in terms of the first and second fundamental forms. The first fundamental form I allows for the measurement of distances and angles on a surface and is defined by

$$\begin{aligned} I &= \begin{pmatrix} dx_1 & dx_2 \end{pmatrix} \begin{pmatrix} E & F \\ F & G \end{pmatrix} \begin{pmatrix} dx_1 \\ dx_2 \end{pmatrix} \\ &= \begin{pmatrix} dx_1 & dx_2 \end{pmatrix} \begin{pmatrix} < \vec{r}_{x_1}, \vec{r}_{x_1} > & < \vec{r}_{x_1}, \vec{r}_{x_2} > \\ < \vec{r}_{x_1}, \vec{r}_{x_2} > & < \vec{r}_{x_2}, \vec{r}_{x_2} > \end{pmatrix} \begin{pmatrix} dx_1 \\ dx_2 \end{pmatrix}. \end{aligned} \tag{3.4}$$

For the surface given by Eq. 3.3, the first fundamental form is

$$I = \begin{pmatrix} dx_1 & dx_2 \end{pmatrix} \begin{pmatrix} 1 + h_{x_1}^2 & h_{x_1} h_{x_2} \\ h_{x_1} h_{x_2} & 1 + h_{x_2}^2 \end{pmatrix} \begin{pmatrix} dx_1 \\ dx_2 \end{pmatrix}. \tag{3.5}$$

The second fundamental form measures the deviation of the surface from being planar. Denoting the normal vector field to the surface by $\vec{n}(x_1, x_2)$, the second fundamental form is defined by

$$\begin{aligned} II &= \begin{pmatrix} dx_1 & dx_2 \end{pmatrix} \begin{pmatrix} L & M \\ M & N \end{pmatrix} \begin{pmatrix} dx_1 \\ dx_2 \end{pmatrix} \\ &= \begin{pmatrix} dx_1 & dx_2 \end{pmatrix} \begin{pmatrix} < \vec{r}_{x_1x_1}, \vec{n} > & < \vec{r}_{x_1x_2}, \vec{n} > \\ < \vec{r}_{x_1x_2}, \vec{n} > & < \vec{r}_{x_2x_2}, \vec{n} > \end{pmatrix} \begin{pmatrix} dx_1 \\ dx_2 \end{pmatrix}. \end{aligned} \tag{3.6}$$

For the surface given by Eq. 3.3, choosing the unit normal vector field

$$\vec{n} = \frac{(h_{x_1}, h_{x_2}, -1)}{(h_{x_1}^2 + h_{x_2}^2 + 1)^{\frac{1}{2}}}, \tag{3.7}$$

the second fundamental form is given by

$$II = \frac{1}{(h_{x_1}^2 + h_{x_2}^2 + 1)^{\frac{1}{2}}} \begin{pmatrix} dx_1 & dx_2 \end{pmatrix} \begin{pmatrix} h_{x_1x_1} & h_{x_1x_2} \\ h_{x_1x_2} & h_{x_2x_2} \end{pmatrix} \begin{pmatrix} dx_1 \\ dx_2 \end{pmatrix}. \tag{3.8}$$

In terms of the first and second fundamental forms, the mean curvature is defined by

$$H = \frac{1}{2}\text{tr}\left(II \cdot I^{-1}\right) = \frac{1}{2}\text{tr}\left[\begin{pmatrix} L & M \\ M & N \end{pmatrix} \frac{1}{EG - F^2} \begin{pmatrix} G & -F \\ -F & E \end{pmatrix}\right].$$

For the surface given by Eq. 3.3, using the expressions given by Eq. 3.5 for the first fundamental form and Eq. 3.8 for the second fundamental form, the mean curvature is

$$\begin{aligned} H &= \frac{1}{2}\text{tr}\left[\frac{1}{(h_{x_1}^2 + h_{x_2}^2 + 1)^{\frac{1}{2}}} \begin{pmatrix} h_{x_1x_1} & h_{x_1x_2} \\ h_{x_1x_2} & h_{x_2x_2} \end{pmatrix} \frac{1}{h_{x_1}^2 + h_{x_2}^2 + 1} \begin{pmatrix} 1 + h_{x_2}^2 & -h_{x_1}h_{x_2} \\ -h_{x_1}h_{x_2} & 1 + h_{x_1}^2 \end{pmatrix}\right] \\ &= \frac{1}{2}\text{tr}\left[\begin{pmatrix} h_{x_1x_1} & h_{x_1x_2} \\ h_{x_1x_2} & h_{x_2x_2} \end{pmatrix} \frac{1}{(h_{x_1}^2 + h_{x_2}^2 + 1)^{\frac{3}{2}}} \begin{pmatrix} (1 + h_{x_2}^2) & -h_{x_1}h_{x_2} \\ -h_{x_1}h_{x_2} & (1 + h_x^2) \end{pmatrix}\right] \end{aligned}$$

$$= \frac{1}{2}\frac{h_{x_1x_1}(h_{x_2}^2+1) - 2h_{x_1x_2}h_{x_1}h_{x_2} + h_{x_2x_2}(h_{x_1}^2+1)}{(h_{x_1}^2+h_{x_2}^2+1)^{\frac{3}{2}}}.$$

In summary, we have arrived at the mean-curvature equation, Eq. 3.2, which we repeat for convenience here:

$$\frac{1}{2}\frac{h_{x_1x_1}(h_{x_2}^2+1) - 2h_{x_1x_2}h_{x_1}h_{x_2} + h_{x_2x_2}(h_{x_1}^2+1)}{(h_{x_1}^2+h_{x_2}^2+1)^{\frac{3}{2}}} = H(x_1,x_2). \tag{3.9}$$

The mean-curvature equation may be written as the divergence of the projection

$$\vec{n}_{||} = \frac{(h_{x_1},h_{x_2})}{(h_{x_1}^2+h_{x_2}^2+1)^{\frac{1}{2}}} \tag{3.10}$$

of the unit normal vector Eq. 3.7 to the (x_1,x_2)-plane as follows: Write

$$\vec{k} \doteq (h_{x_1},h_{x_2}) \doteq (f,g), \quad k^2 \doteq \vec{k}\begin{pmatrix} 1 & 0 \\ 0 & 1 \end{pmatrix}\vec{k}^{\mathrm{t}} = f^2+g^2,$$

$$\vec{\kappa} = \begin{pmatrix} 1 & 0 \\ 0 & 1 \end{pmatrix}\vec{k}^{\mathrm{t}} = (f,g)\,,$$

and

$$B(k^2) \doteq \frac{1}{2}(k^2+1)^{-\frac{1}{2}} = \frac{1}{2}(f^2+g^2+1)^{-\frac{1}{2}} = \frac{1}{2}(h_{x_1}^2+h_{x_2}^2+1)^{-\frac{1}{2}}.$$

Then, for $\nabla = \left(\frac{\partial}{\partial x_1},\frac{\partial}{\partial x_2}\right)$, Eq. 3.9 is

$$\nabla\cdot\frac{1}{2}\vec{n}_{||} = \nabla\cdot\left(\vec{\kappa}B(k^2)\right) = \frac{1}{2}\frac{h_{x_1x_1}(h_{x_2}^2+1) - 2h_{x_1x_2}h_{x_1}h_{x_2} + h_{x_2x_2}(h_{x_1}^2+1)}{(h_{x_1}^2+h_{x_2}^2+1)^{\frac{3}{2}}} = H. \tag{3.11}$$

The method that we apply to find solutions to the mean-curvature equation may be applied more generally to equations of the general form given by Eq. 3.11, and in the following, we will derive to an extent results for this general from.

3.4 Surfaces via the hodograph transform

3.4.1 The hodograph transform

Equation 3.9 contains cubic products such as $h_{x_1x_1}h_{x_2}^2$ as well as a denominator that involves quadratic terms and a $\frac{3}{2}$ root. It is nonlinear. However, the equation is linear in the highest-order (second-order) derivatives. This suggests to rewrite Eq. 3.9 in terms of the *hodograph transform* of $h(x_1, x_2)$. The hodograph transform of $h(x_1, x_2)$ is a function $\hat{h}(f, g)$ of the gradient $(f, g) = \nabla h = (h_{x_1}, h_{x_2})$.

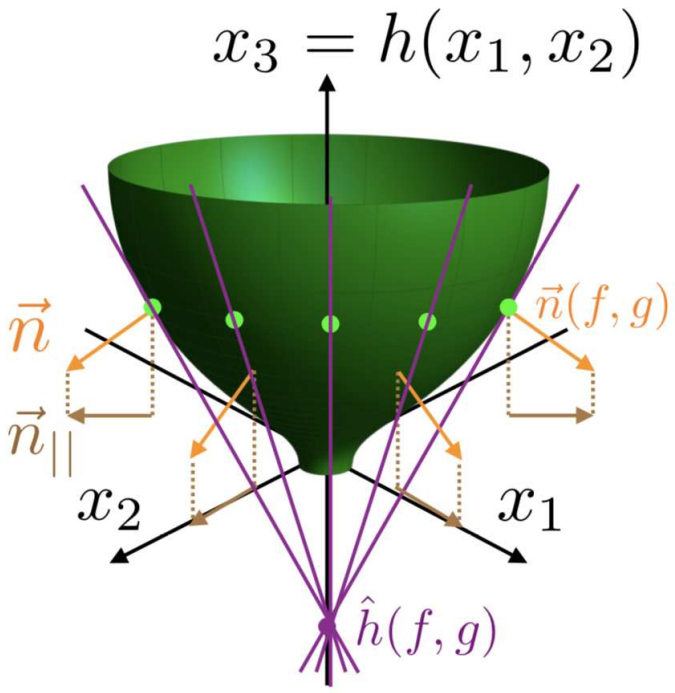

Figure 3.4: Illustration of the hodograph transform $\hat{h}(f, g)$ of a function $h(x_1, x_2)$.

Fig. 3.4 illustrates the hodograph transformation, which is defined as follows: The function $h(x_1, x_2) = h(\vec{x})$ and its hodograph transform $\hat{h}(f, g) = \hat{h}(\vec{k})$ are related by

$$h(\vec{x}) + \hat{h}(\vec{k}) = \vec{k} \cdot \vec{x} = fx_1 + gx_2;$$

$$\nabla_{\vec{x}} h = (h_{x_1}, h_{x_2}) = \vec{k}, \;\; \nabla_{\vec{k}} \hat{h} = \left(\hat{h}_f, \hat{h}_g\right) = \vec{x}.$$

The second derivatives are related by

$$\begin{pmatrix} h_{x_1x_1} & h_{x_1x_2} \\ h_{x_2x_1} & h_{x_2x_2} \end{pmatrix} = \begin{pmatrix} f_{x_1} & f_{x_2} \\ g_{x_1} & g_{x_2} \end{pmatrix} = \begin{pmatrix} (\hat{h_f})_f & (\hat{h_g})_f \\ (\hat{h_f})_g & (\hat{h_g})_g \end{pmatrix}^{-1} = J^{-1} \begin{pmatrix} \hat{h}_{gg} & -\hat{h}_{fg} \\ -\hat{h}_{fg} & \hat{h}_{ff} \end{pmatrix},$$

where

$$J = \left|\frac{\partial \vec{x}}{\partial \vec{k}}\right| = \hat{h}_{ff}\hat{h}_{gg} - \hat{h}_{fg}^2.$$

In hodograph variables, Eq. 3.11 for general $B(k^2)$, namely

$$\nabla \cdot \left(\vec{\kappa} B(k^2)\right) = H, \tag{3.12}$$

is

$$\left(B + 2\frac{dB}{dk^2} f^2\right) \hat{h}_{gg} - 4\frac{dB}{dk^2} fg \hat{h}_{fg} + \left(B + 2\frac{dB}{dk^2} g^2\right) \hat{h}_{ff} = HJ. \tag{3.13}$$

This has the form of a *Monge-Ampere equation*. The general form of a Monge-Ampere equation for a function $u(x, y)$ is

$$C_1 u_{xx} + 2C_2 u_{xy} + C_3 u_{yy} + C_4(u_{xx}u_{yy} - u_{xy}^2) + C_5 = 0,$$

where the coefficients C_j are functions of x, y, u, u_x,and u_y only [67].

3.4.2 Separation of variables

We convert the hodograph transform of the MCE, Eq. 3.13, to a polar coordinate system and find that some solutions may be obtained by separation of variables. In accordance with the definition

$k^2 = f^2 + g^2$, we write polar coordinates as

$$(f, g) = (k\cos\phi, k\sin\phi)\,. \tag{3.14}$$

In this coordinate system, Eq. 3.13 reads

$$\frac{1}{k^2}(kB)_k\hat{h}_{\phi\phi} + \frac{1}{k}(kB)_k\hat{h}_k + B\hat{h}_{kk} = HJ; \tag{3.15}$$

$$\frac{1}{k^2}(kB)_k\hat{h}_{\phi\phi} + \frac{1}{k}\left\{(kB)\hat{h}_k\right\}_k = HJ, \tag{3.16}$$

where

$$J = \frac{1}{k^2}\hat{h}_{kk}(\hat{h}_{\phi\phi} + k\hat{h}_k) - \frac{1}{k^4}(\hat{h}_\phi - k\hat{h}_{k\phi})^2. \tag{3.17}$$

From solutions $\hat{h}(k, \phi)$, we obtain surfaces

$$\vec{r}(k, \phi) = (x(k, \phi), y(k, \phi), h(k, \phi)) = \left(\hat{h}_f, \hat{h}_g, k\hat{h}_k - \hat{h}\right) \tag{3.18}$$

parameterized by k and ϕ.

The expressions for $x(k, \phi)$ and $y(k, \phi)$ are

$$x(k, \phi) = \frac{\partial\hat{h}}{\partial f} = \frac{\partial\hat{h}}{\partial k}\frac{\partial k}{\partial f} + \frac{\partial\hat{h}}{\partial\phi}\frac{\partial\phi}{\partial f} = \frac{\partial\hat{h}}{\partial k}\cos\phi + \frac{\partial\hat{h}}{\partial\phi}\left(-\frac{\sin\phi}{k}\right) \tag{3.19}$$

and

$$y(k, \phi) = \frac{\partial\hat{h}}{\partial g} = \frac{\partial\hat{h}}{\partial k}\frac{\partial k}{\partial g} + \frac{\partial\hat{h}}{\partial\phi}\frac{\partial\phi}{\partial g} = \frac{\partial\hat{h}}{\partial k}\sin\phi + \frac{\partial\hat{h}}{\partial\phi}\left(\frac{\cos\phi}{k}\right) \tag{3.20}$$

We apply separation of variables to Eq. 3.15 by making the Ansatz

$$\hat{h}(k, \phi) = F_n(k)\cos(n\phi + \phi_0), \tag{3.21}$$

under which Eq. 3.15 becomes

$$\left[k^2 BF_{n,kk} + k(kB)_k F_{n,k} - n^2 (kB)_k F_n\right] \cos(n\phi + \phi_0) = k^2 HJ, \tag{3.22}$$

where

$$k^4 J = -n^2 (kF_{n,k} - F_n)^2 - \cos^2(n\phi) \left[n^2 k^2 (F_n F_{n,kk} - F_{n,k}^2) + 2n^2 k F_n F_{n,k} - n^2 F_n^2 - k^3 F_{n,k} F_{n,kk}\right]. \tag{3.23}$$

3.4.3 Surfaces of revolution

In this section, we specialize in two ways: First, consider the case $n = 0$. Secondly, we assume that the mean curvature is a function of radius alone; $H(x_1, x_2) = H(r)$.

The case $n = 0$ corresponds to surfaces of revolution

$$(x, y, h(x, y)) = (r\cos(\phi), r\sin(\phi), h(r)).$$

Indeed,

$$x = \frac{\partial \hat{h}}{\partial f} = \frac{\partial \hat{h}}{\partial k}\frac{\partial k}{\partial f} + \frac{\partial \hat{h}}{\partial \phi}\frac{\partial \phi}{\partial f} = \frac{\partial \hat{h}}{\partial k}\cos\phi + 0\left(-\frac{\sin\phi}{k}\right) = \frac{\partial \hat{h}}{\partial k}\cos\phi,$$

and similarly

$$y = \frac{\partial \hat{h}}{\partial k}\sin\phi.$$

Hence, $r = (x^2 + y^2)^{\frac{1}{2}} = |\frac{\partial \hat{h}}{\partial k}|$. Furthermore,

$$h_x = h_r r_x = h_r \frac{x}{r}, \;\; h_y = h_r r_y = h_r \frac{y}{r}; \;\; k = (h_x^2 + h_y^2)^{\frac{1}{2}} = \left(h_r^2 \frac{x^2}{r^2} + h_r^2 \frac{y^2}{r^2}\right)^{\frac{1}{2}} = h_r. \tag{3.24}$$

The separation of variables Ansatz, Eq. 3.21, for $n = 0$ is

$$\hat{h} = F_0(k),$$

and from Eq. 3.23,

$$J = \frac{1}{k} F_{0,k} F_{0,kk}.$$

Eq. 3.22 for $n = 0$ is therefore

$$(kBF_{0,kk} + (kB)_k F_{0,k}) \cos\phi_0 = H(r) F_{0,kk} F_{0,k}.$$

For $\phi_0 = 0$,

$$F_{0,kk} = \frac{(kB)_k F_{0,k}}{H(r) F_{0,k} - kB}. \tag{3.25}$$

Writing $r \doteq F_{0,k}$,

$$\frac{dr}{dk} = \frac{(kB)_k r}{H(r) r - kB}. \tag{3.26}$$

Eq. 3.26 has the general solution

$$\int r H(r)\, dr - rkB(k) + \frac{1}{2} C = 0, \tag{3.27}$$

where C is a constant of integration. For the MCE, $B(k^2) = -\frac{1}{2}(k^2+1)^{-\frac{1}{2}}$, and Eq. 3.26 reads

$$\frac{dr}{dk} = \frac{-1}{k^2+1} \frac{r}{2H(r)(k^2+1)^{\frac{1}{2}} r + k}. \tag{3.28}$$

The general solution for Eq. 3.28 is

$$\int r H(r)\, dr + \frac{1}{2} rk(k^2+1)^{-\frac{1}{2}} + \frac{1}{2} C = 0, \tag{3.29}$$

where again C is a constant of integration. This last expression may be solved for k, which we recall, from (3.24), is equal to dh/dr. Writing

$$Q(r) \doteq \int r H(r)\, dr,$$

we have that

$$k = \frac{dh}{dr} = \pm \frac{Q(r) + C}{(r^2 - Q^2(r) - 2CQ(r) - C^2)^{\frac{1}{2}}}, \tag{3.30}$$

and finally

$$h(r) = \int \frac{dh}{dr}\, dr = \pm \int \frac{Q(r) + C}{(r^2 - Q^2(r) - 2CQ(r) - C^2)^{\frac{1}{2}}}\, dr. \tag{3.31}$$

3.4.4 Surfaces of constant mean curvature

In this subsection, we further specialize to assume that $H(r) = H$ is constant. Under this assumption, the general solution Eq. 3.29 is

$$Hr^2 + \frac{kr}{(k^2+1)^{\frac{1}{2}}} + C = 0. \tag{3.32}$$

For example, if $C = 0$,

$$\frac{dh}{dr} = k = -Hr(1 - H^2r^2)^{-\frac{1}{2}},$$

so that

$$h(r) = (R^2 - r^2)^{\frac{1}{2}}.$$

The resulting surface is the upper hemisphere

$$(r\cos(\phi), r\sin(\phi), h(r) = (R^2 - r^2)^{\frac{1}{2}})$$

of radius $R = 1/H$. Fig. 3.5 illustrates this solution: plotted are the phase plane for the system

$$\begin{aligned} \frac{dr}{dt} &= -r \\ \frac{dk}{dt} &= 2(k^2+1)^{\frac{3}{2}}r + k(k^2+1). \end{aligned} \tag{3.33}$$

associated to Eq. 3.28 for $H(r) \equiv 1$ constant, the trajectory $k = \frac{dh}{dr}$ in the phase plane corresponding to the choice $C = 0$, the curve $h(r)$, and (below all of this), the surface of revolution.

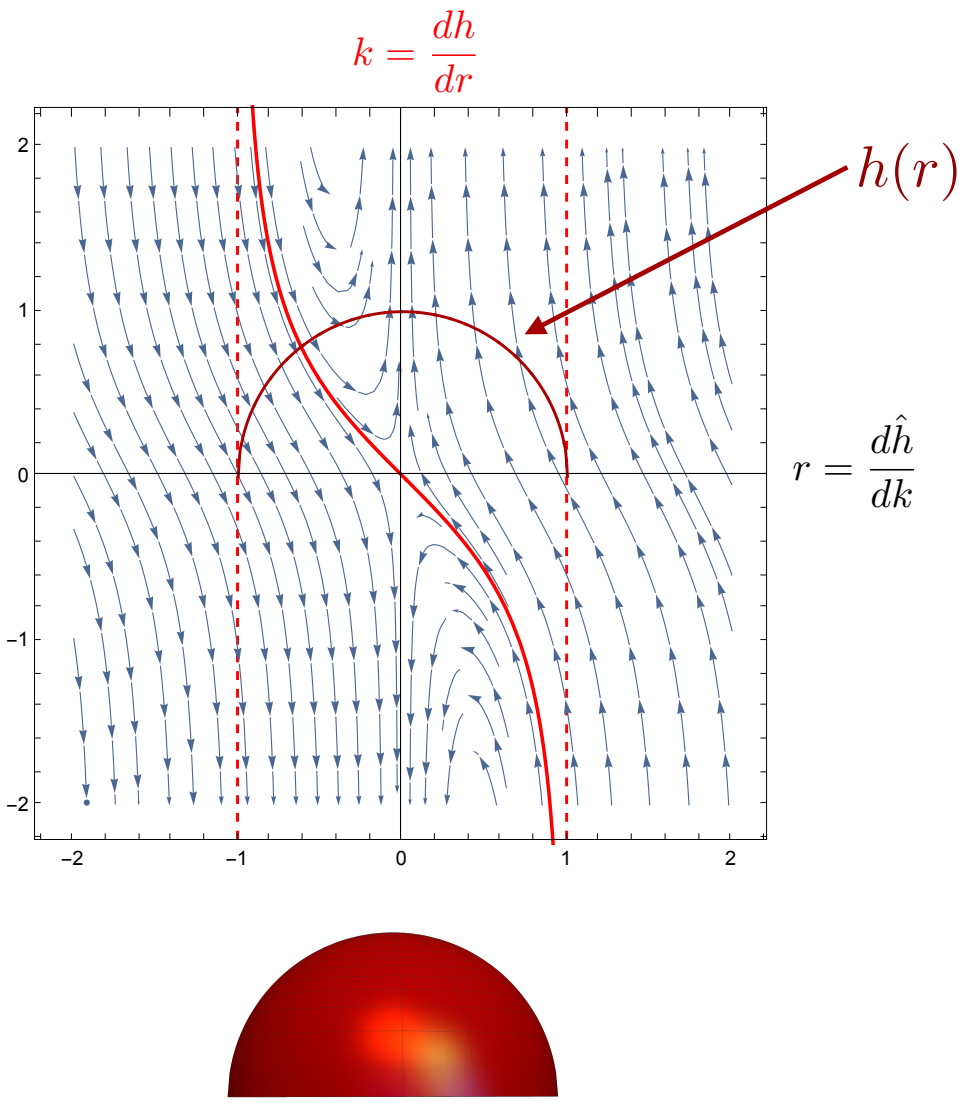

Figure 3.5: The phase plane for the system, the trajectory $k = \frac{dh}{dr}$ in the phase plane corresponding to the choice $C = 0$, the curve $h(r)$, and (below), the surface of revolution $(r\cos(\phi), r\sin(\phi), h(r))$.

For general C,

$$\frac{dh}{dr} = \pm\frac{Hr^2 + C}{(-H^2r^4 + (1-2HC)r^2 - C^2)^{\frac{1}{2}}} = \pm\frac{Hr^2 + C}{(r^2 - (Hr^2 + C)^2)^{\frac{1}{2}}}. \tag{3.34}$$

This last equation may be written as

$$\frac{dh}{dr} = \pm\frac{Hr^2 + C}{[-(Hr^2 + r + C)(Hr^2 - r + C)]^{\frac{1}{2}}} = \pm\frac{Hr^2 + C}{[-(r+\xi_+)(r-\xi_+)(r+\xi_-)(r-\xi_-)]^{\frac{1}{2}}},$$

where

$$\xi_\pm = \frac{1 \pm (1-4HC)^{\frac{1}{2}}}{2H}.$$

The resulting solution

$$h(r) = \pm\int \frac{Hr^2 + C}{[-(r+\xi_+)(r-\xi_+)(r+\xi_-)(r-\xi_-)]^{\frac{1}{2}}}\, dr$$

is an elliptic integral. An *elliptic integral* is defined as a function $E(r)$ that has the from

$$E(r) = \int_{r_0}^{r} R(\hat{r}, \hat{s})\, d\hat{r},$$

where R is a rational function (ratio of one polynomial to another) of its two arguments, and the variables $\hat{r}$ and $\hat{s}$ are related by $\hat{s}^2 = P(\hat{r})$, where $P(\hat{r})$ is a polynomial of degree 3 or 4 that has no repeated roots. In our case,

$$R(\hat{r}, \hat{s}) = \frac{H\hat{r}^2 + C}{\hat{s}},$$

and $P(\hat{r})$ is the quartic polynomial

$$P(\hat{r}) = -(\hat{r}+\xi_+)(\hat{r}-\xi_+)(\hat{r}+\xi_-)(\hat{r}-\xi_-).$$

The expression Eq. 3.34 for $\frac{dh}{dr}(r)$ and (dropping the hat notation) the polynomial $P(r)$ are plotted in Figure 3.6. The intervals in which $P(r)$ is positive determine the intervals in which Eq. 3.34 is

real and may be integrated to obtain $h(r)$. For $C < 0$, $P(r)$ is positive for $-\xi_- < r < \xi_+$. For $C = 0$, $P(r)$ is positive for $-\xi_- = \xi_- = 0 < r < \xi_+ = \frac{1}{H}$. For $0 < C < \frac{1}{4H}$, $P(r)$ is positive for $\xi_- < r < \xi_+$. For $C > \frac{1}{4H}$, $P(r)$ is negative for all r.

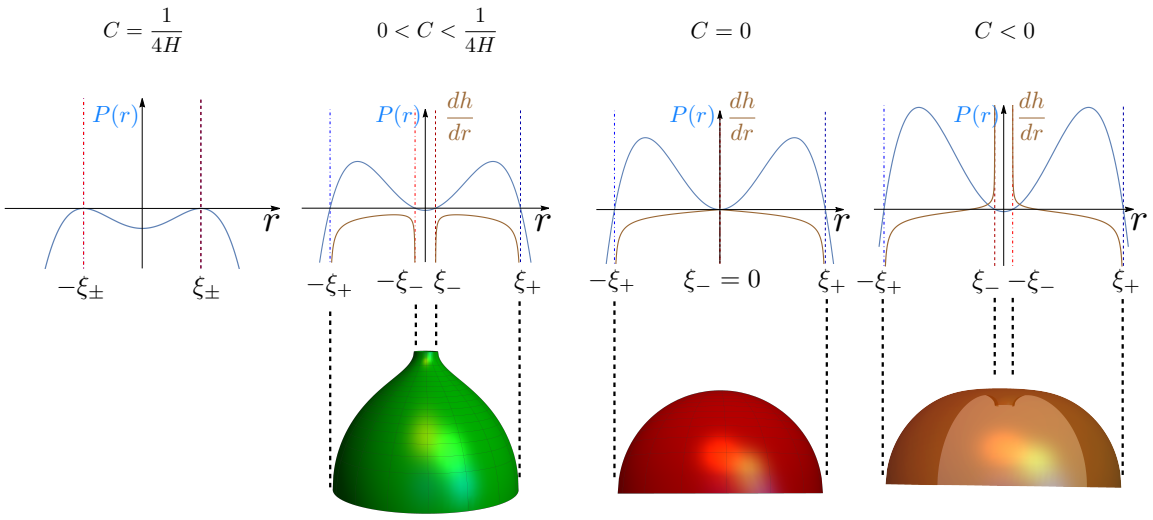

Figure 3.6: The quartic polynomial $P(r) = -(r+\xi_+)(r-\xi_+)(r+\xi_-)(r-\xi_-)$ in the denominator of Eq. 3.34 and the function $\frac{dh}{dr}$ given by Eq. 3.34 for $H = 1$ and values of C in the four intervals of interest described in the text. Also shown are the surfaces of revolution $(r\cos\phi, r\sin\phi, h(r))$.

The surfaces of revolution obtained from these solutions are the well-known Delaunay surfaces: These are all the surfaces of revolution of constant mean curvature and were found by Delaunay in 1841 [68, 69]. The Delaunay surfaces are the catenoid (the only minimal surface of revolution and not contained in the formulas derived here since $H = 0$), the cylinder, the sphere, unduloids, and nodoids. Each of these surfaces is the surface of revolution of a roulette of a conic, namely a curve in the plane formed by finding the trace of the focus of a conic section as it rolls on a line. Unduloids are formed by revolving undularies, which are roulettes of ellipses, and nodoids are formed by revolving nodaries, which are roulettes of hyperbolas. In our setup, we obtain the unduloid for $0 < C < \frac{1}{4H}$, the sphere for $C = 0$, and the nodoid for $C < 0$. In Fig. 3.6 we show portions of these surfaces that are graphs over the plane. The full surfaces are periodic, as shown in Fig. 3.7.

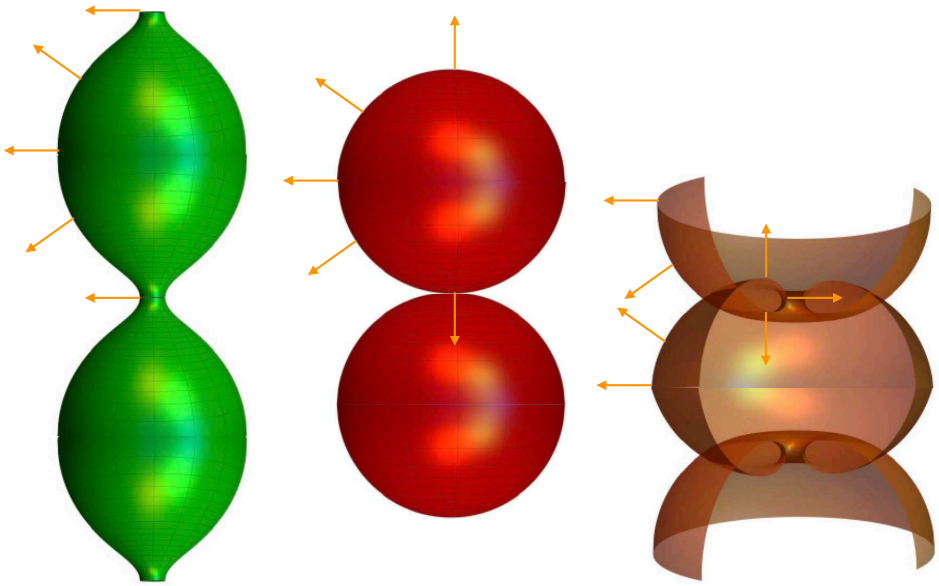

Figure 3.7: Delaunay surfaces: The unduloid (green), the sphere (red), and the nodoid (brown).

3.4.5 Conformal parameterizations of Delaunay surfaces

The literature gives various parameterizations of Delaunay surfaces in the form

$$(r(u)\cos v, r(u)\sin v, h(r(u)) = \Psi(u))\,.$$

For example, Ref. [70] provides parameterizations of Delaunay surfaces, starting from the surfaces as revolutions of roulettes of conics. An unduloid formed as the roulette of an ellipse with major axis a, minor axis b, and $c \doteq (a^2 - b^2)^{\frac{1}{2}}$ may be parameterized as

$$\begin{cases} r(u) = (m\sin(\mu u) + n)^{\frac{1}{2}}, \\ \Psi(u) = aF_1\left(\dfrac{\mu u}{2} - \dfrac{\pi}{4}|k\right) + cE_2\left(\dfrac{\mu u}{2} - \dfrac{\pi}{4}|k\right), \end{cases}$$

where

$$\mu = \frac{2}{a+c},\ k^2 = \frac{c^2-a^2}{c^2},\ m^2 = \frac{c^2-a^2}{2},\ n^2 = \frac{c^2+a^2}{2},$$

$F_1(z|k)$ and $E_2(z|k)$ are the normal elliptic integral of the first and second kind, respectively [70]. The first fundamental form is

$$I = du^2 + \frac{1}{2}\left(a^2 + c^2 + (c^2 - a^2)\sin\left(\frac{2u}{a+c}\right)\right)dv^2.$$

Note that these parameterizations are not conformal. That is, the first fundamental form is not diagonal (it does not have the form $I = E(u,v)(du^2 + dv^2)$).

With the aid of Eq. 3.34, we conformally parameterize Delaunay surfaces. We can write a surface of revolution as

$$\vec{r}(u,v) = (r(u)\cos v, r(u)\sin v, \Psi(u) = h\left(r(u)\right)). \tag{3.35}$$

This surface of revolution is orthogonally parameterized for any $r(u)$ and $h(r)$. It is conformally parameterized if $\vec{r}_u \cdot \vec{r}_u = \vec{r}_v \cdot \vec{r}_v$. We evaluate

$$\vec{r}_u \cdot \vec{r}_u = r_u^2 + \Psi_u^2 = r_u^2 + \left(\frac{dh}{dr}\frac{dr}{du}\right)^2 = r_u^2\left(1 + \left(\frac{dh}{dr}\right)^2\right),$$

and

$$\vec{r}_v \cdot \vec{r}_v = r(u)^2.$$

The condition for conformality is therefore

$$r_u^2\left(1 + \left(\frac{dh}{dr}\right)^2\right) = r^2. \tag{3.36}$$

Using expression Eq. 3.34 for $\frac{dh}{dr}$, this condition becomes

$$r_u^2 = r^2 - (Hr^2 + C)^2 = -(Hr^2 + C - r)(Hr^2 + C + r). \tag{3.37}$$

That is,

$$\int \frac{1}{(r^2-(Hr^2+C)^2)^{\frac{1}{2}}}dr = \int du; \tag{3.38}$$

We have come across another elliptic integral! The function $u(r)$ is an elliptic integral, but we are aiming to find its inverse, $r(u)$. The inverse of an elliptic integral is called an *elliptic function*. If we find $r(u)$ and, from Eq. 3.34, the elliptic integral $h(r)$, we have a conformal parameterization Eq. 3.35 for a Delaunay surface. The first fundamental form for this parameterization is

$$I = r(u)^2(du^2+dv^2).$$

To find $r(u)$, we need to be mindful of the intervals in r for which the denominator $P(r)$ in the integral Eq. 3.38 is positive, as described above and depicted in Fig. 3.6.

For example, numerically solving Eq. 3.37 with the initial condition $r(0) = \frac{\xi_- + \xi_+}{2} = \frac{1}{2H}$ for the choice $H = 1$ yields the function $r(u)$ and coefficient of the first fundamental form $r(u)^2$ plotted in Figure 3.8.

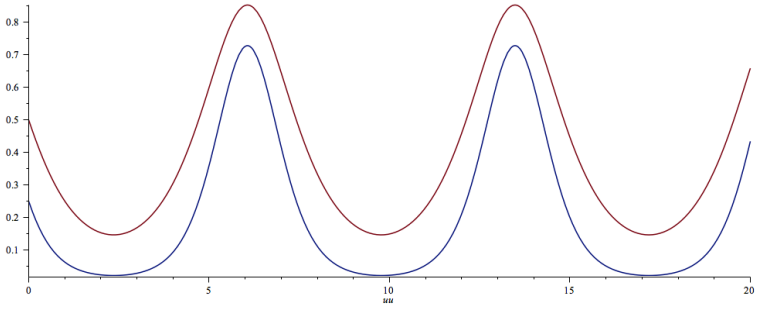

Figure 3.8: For $H = 1$ and $C = \frac{1}{8}$, and the initial condition $r(0) = \frac{1}{2}$, the solution $r(u)$ (in red) and the coefficient $r^2(u)$ of the first fundamental form (in blue).

The $C = 0$ case may be solved for simply: For $C = 0$, Eq. 3.37 is

$$r_u^2 = r^2(1-H^2r^2).$$

This has the solution

$$r(u) = \frac{1}{H}\text{sech}(u).$$

Recall that the solution for $h(r)$ to Eq. 3.34 in the case $C = 0, H = 1$ is

$$h(r) = (1 - r^2)^{\frac{1}{2}},$$

so that

$$\Psi(u) = h(r(u)) = \text{tanh}(u).$$

The resulting surface of revolution

$$\vec{r}(u, v) = (\text{sech}u \cos v, \text{sech}u \sin v, \text{tanh}u)$$

is the Mercator projection of the sphere with first fundamental form

$$I = \text{sech}^2 u(du^2 + dv^2).$$

The function $G(u) = \ln(\text{sech}(u))$ satisfies the ODE

$$G_{uu} + \text{e}^{2G(u)} = 0.$$

We have solutions to this equation from Eq. 3.38, using $G = \ln(r(u))$.

3.4.6 Radially dependent mean curvature

We now relax the assumption that the mean curvature is constant to allow the mean curvature to be a function of the radius; that is, we return to Eq. 3.30, which we repeat here for convenience: For

$$Q(r) \doteq \int rH(r)\, dr,$$

$$k = \frac{dh}{dr} = \pm \frac{Q(r) + C}{(r^2 - Q^2(r) - 2CQ(r) - C^2)^{\frac{1}{2}}}. \tag{3.39}$$

The condition for a reparameterization $r(u)$ that results in a conformal parameterization, namely Eq. 3.36, becomes

$$r_u^2 = r^2 - (Q(r) + C)^2 = -(Q(r) + r + C)(Q(r) - r + C). \tag{3.40}$$

We start with an example for which the antiderivative of Eq. 3.39 is easily computed: For $H(r) = \frac{a}{r}$,

$$k = \frac{dh}{dr} = \pm \frac{ar + C}{((1 - a^2)r^2 - 2Car - C^2)^{\frac{1}{2}}}. \tag{3.41}$$

For $C = 0$, Eq. 3.41 becomes

$$k = \frac{dh}{dr} = \frac{a}{(1 - a^2)^{\frac{1}{2}}},$$

and

$$h(r) = \frac{a}{(1 - a^2)^{\frac{1}{2}}} r.$$

The resulting surface of revolution is the cone!

More generally, choosing the positive sign in Eq. 3.41 antidifferentiation yields

$$\begin{aligned} h(r) =& \frac{a}{1 - a^2} \sqrt{(1 - a^2)r^2 - 2Car - C^2} \\ &+ \frac{C}{(a^2 - 1)^{\frac{3}{2}}} \arctan\left(\frac{(a^2 - 1)r + aC}{\sqrt{a^2 - 1}\sqrt{(1 - a^2)r^2 - 2Car - C^2}} \right) \end{aligned} \tag{3.42}$$

Choosing, for example, $a = 2$ and $C = -3$, we have

$$h(r) = \frac{\sqrt{3}}{3}\text{arctan}\left(\sqrt{3}\frac{r-2}{\sqrt{-3r^2+12r-9}}\right) - \frac{2}{3}\sqrt{-3r^2+12r-9}.$$

The corresponding surface of revolution is shown in Fig. 3.9. Solving Eq. 3.40 with $Q(r) = ar$ yields the reparameterization

$$r(u) = \frac{C}{a^2-1}\left(\sin(\sqrt{a^2-1}u) + a\right)$$

that provides a conformal paramterization.

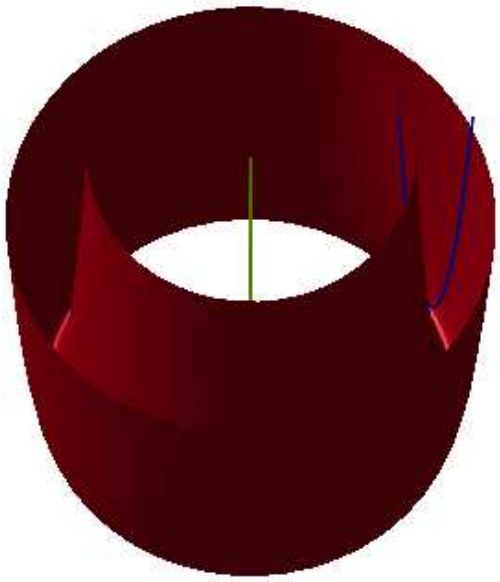

Figure 3.9: Surface of revolution with radially-dependent mean curvature $H(r) = \frac{2}{r}$.

For $Q(r) = r^m$, where $m \in \mathbb{N}$, the solution $h(r)$ is a hyperelliptic integral. A *hyperelliptic integral* is defined as a function $H(r)$ that has the from

$$H(r) = \int_{r_0}^{r} R(\hat{r}, \hat{s})\, d\hat{r},$$

where R is a rational function of its two arguments, and the variables $\hat{r}$ and $\hat{s}$ are related by $\hat{s}^2 = P(\hat{r})$, where $P(\hat{r})$ is a polynomial of degree $n \geq 5$ that has no repeated roots.

3.4.7 The pendulum

Eq. 3.28 may be converted to a dynamical system related to that for the nonlinear pendulum. Define $\varphi \doteq \arctan(k)$, so that $1 + k^2 = \sec^2 \varphi$, and

$$\frac{dr}{d\varphi} = \frac{dk}{d\varphi}\frac{dr}{dk} = \frac{-r\cos\varphi}{2rH(r) + \sin\varphi}. \tag{3.43}$$

The general solution to Eq. 3.43 is

$$\int rH(r)\, dr + \frac{1}{2} r \sin\varphi + C = 0.$$

Eq. 3.43 may be written as the system

$$\frac{dr}{d\tau} = -r\cos\varphi,$$

$$\frac{d\varphi}{d\tau} = 2rH(r) + \sin\varphi. \tag{3.44}$$

The phase space for this system is shown in Fig. 3.10. It follows that

$$\frac{d^2\varphi}{d\tau^2} = -2r^2 H'(r)\cos\varphi + \frac{1}{2}\sin(2\varphi).$$

Setting $\theta \doteq 2\varphi - \pi$, this becomes

$$\frac{d^2\theta}{d\tau^2} = -4r^2 H'(r)\cos\left(\frac{1}{2}(\theta + \pi)\right) - \sin(\theta); \;\; \frac{d^2\theta}{d\tau^2} + \sin\theta = 4r^2 H'(r)\sin\left(\frac{1}{2}\theta\right).$$

For $H(r) = H$ constant, this equation is the pendulum equation

$$\frac{d^2\theta}{d\tau^2} + \sin\theta = 0.$$

The equation is also independent of r if $H(r) = \frac{a}{4r}$ for a constant a;

$$\frac{d^2\theta}{d\tau^2} + \sin\theta + a\sin\left(\frac{1}{2}\theta\right) = 0.$$

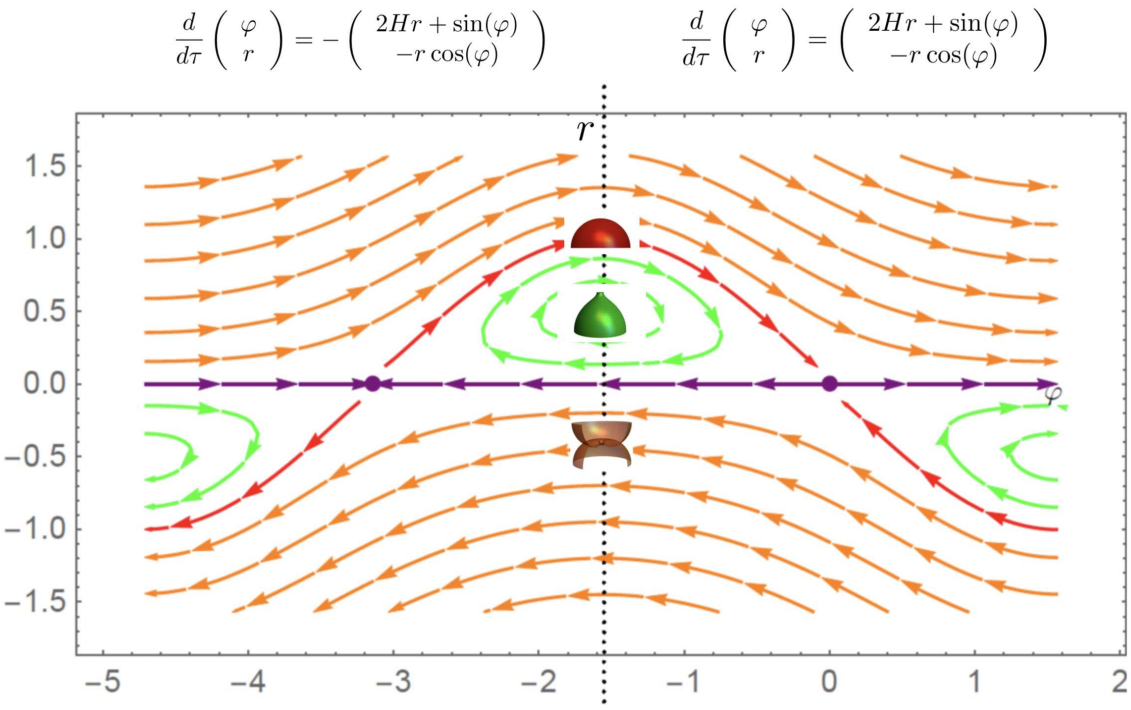

Figure 3.10: The phase space of Eq. 3.44 and corresponding surfaces for $C < 0$ (left panels), $C = 0$ (center panels) and $C > 0$ (right panels). The intervals corresponding to $\mathbb{R}^3$ give (parts of) an orange nodoid, a red sphere, and a green unduloid.

3.4.8 Conclusions and Further Work

The hodograph transformation applied to the mean-curvature equation has allowed us to find formulas surfaces of revolution with prescribed mean that depends on radius alone. In the case of constant mean curvature, we obtain the already well known Delaunay surfaces, are these are all the surfaces of revolution of constant mean curvature. However, we have achieved a new result even for this case: We have obtain conformal parameterizations of these surfaces in terms of elliptic integrals and elliptic functions.

These conformal parameterizations may be used to determine Weierstrass-Enneper representations for the surfaces. The classical Weierstrass-Enneper representation associates to any pair of holomorphic functions $\psi_1(z)$, $\psi_2(z) : \mathbb{C} \to \mathbb{C}$ a Euclidean minimal surface. This, as well as a generalization to surfaces of prescribed, but not necessarily everywhere equal to 0, mean curvature may be seen as follows [71]:

Via the mapping $(x, y, h) \to x\mathbf{i} + y\mathbf{j} + h\mathbf{k}$, isometrically identify $\mathbb{R}^3$ with the 3-dimensional real Lie algebra $\mathfrak{su}(2)$, with the Killing form $< X, Y >= -\frac{1}{2}\text{tr}(XY)$ and the orthogonal basis

$$\mathbf{i} = \begin{pmatrix} 0 & -i \\ -i & 0 \end{pmatrix}, \ \mathbf{j} = \begin{pmatrix} 0 & -1 \\ 1 & 0 \end{pmatrix}, \ \mathbf{k} = \begin{pmatrix} -i & 0 \\ 0 & i \end{pmatrix}.$$

By this identification, we can consider a surface $\vec{r}(\eta, \xi) : \Omega \subset \mathbb{R}^2 \to \mathbb{R}^3$, $\vec{r}(u, v) = (r_1(\eta, \xi), r_2(\eta, \xi), r_3(\eta, \xi))$ as a surface $\vec{r}(\eta, \xi) : \Omega \subset \mathbb{R}^2 \to \mathfrak{su}(2)$; $\vec{r}(u, v) = r_1(\eta, \xi)\mathbf{i} + r_2(\eta, \xi)\mathbf{j} + r_3(\eta, \xi)\mathbf{k}$.

Write $z = \eta + i\xi$. Given two holomorphic functions $\psi_1(z)$, $\psi_2(z) : \mathbb{C} \to \mathbb{C}$, define $q = \psi_1\bar{\psi}_2 + \psi_2\bar{\psi}_2$, and $\phi_{1,2} \doteq q^{-\frac{1}{2}}\psi_{1,2}$. Then, $\phi_1\bar{\phi}_1 + \phi_2\bar{\phi}_2 = 1$, and we have a function $\Phi : \mathbb{C} \to SU(2)$;

$$\Phi = \begin{pmatrix} \phi_1 & \phi_2 \\ -\bar{\phi}_2 & \bar{\phi}_1 \end{pmatrix}.$$

We use q and Φ to determine an orthogonal frame that we integrate to obtain a minimal surface $\vec{r}(\eta, \xi) : \Omega \subset \mathbb{R}^2 \to \mathfrak{su}(2)$. Define the frame by

$$\vec{r}_\eta = \Phi^{-1}q\mathbf{i}\Phi, \quad \vec{r}_\xi = \Phi^{-1}q\mathbf{j}\Phi, \quad \vec{n} = \Phi^{-1}\mathbf{k}\Phi. \tag{3.45}$$

The integrability condition is that $\vec{r}_{\eta\xi} = \vec{r}_{\xi\eta}$. The holomorphicity of $\psi_{1,2} = q^{\frac{1}{2}}\phi_{1,2}$ guarantees the satisfaction of this integrability condition and also that the mean curvature the surface $\vec{r}$ be equal to zero. The functions $\psi_{1,2}$ are the Weierstrass-Enneper representation of the surface, which has first fundamental form $I = q^2(d\eta^2 + d\xi^2)$.

More generally, the Weierstrass-Enneper representation of any conformally parameterized surface, with first fundamental form $I = q^2(d\eta^2 + d\xi^2)$, may defined by solving the integrability condition $\vec{r}_{\eta\xi} = \vec{r}_{\xi\eta}$ for the functions $\psi_{1,2} = q^{\frac{1}{2}}\phi_{1,2}$. Alternatively, if a conformal parameterization $\vec{r}(\eta, \xi)$ with first fundamental form $I = q^2(d\eta^2 + d\xi^2)$ is known, solving Eq. 3.45 for $\phi_{1,2}$ yields the Weierstrass-Enneper representation $\psi_{1,2} = q^{\frac{1}{2}}\phi_{1,2}$ of the surface.

It is worthy of note that Eq. 3.37, namely $r_u^2 = r^2 - (Hr^2 + C)^2$, may be rewritten in the following form: Define a function $G(u)$ via $r(u) \doteq \mathrm{e}^{G(u)}$. Then,

$$G_u^2 = -H^2\mathrm{e}^{2G} + (1 - 2CH) - \sigma_1 C^2\mathrm{e}^{-2G};$$

$$2G_u G_{uu} = -H^2\mathrm{e}^{2G}2G_u + C^2\mathrm{e}^{-2G}2G_u;$$

$$G_{uu} + H^2\mathrm{e}^{2G} - C^2\mathrm{e}^{-2G} = 0;$$

$$G_{uu} + \mathrm{e}^{2G}(H - C\mathrm{e}^{-2G})(H + C\mathrm{e}^{-2G}) = 0;$$

$$G_{uu} + \mathrm{e}^{2G}k_1k_2 = 0,$$

where $k_1 = H - C\mathrm{e}^{-2G}$ and $k_2 = H + C\mathrm{e}^{-2G}$ are the principal curvatures of the surface. For $C = H$, this is

$$G_{uu} + 2H^2\sinh(2G) = 0.$$

There are likely connections, to be explored in future work, to surfaces of constant mean curvature under the condition that lines of curvature lie on spheres, by Abresch [72] and Walter [73]. These authors consider solutions to the elliptic sinh-Gordon equation $\Delta G + \sinh(2G) = 0$. Similarly, the reduction of the Gauss equation to Painlevé III in Ref. [74] and Ref. [75], Chapter 5, Eq. (5.28) involves the elliptic sinh-Gordon equation.

Chapter 4

Estimating spectra through Bayesian Inversion

4.1 Deconstruction of Absorbance Spectra

The absorbance spectrum of a solution gives the absorbance $Abs(\lambda)$ as a function of the wavelength λ. An example absorbance spectrum of a solution of the anthocyanin is shown in Figure 4.1.

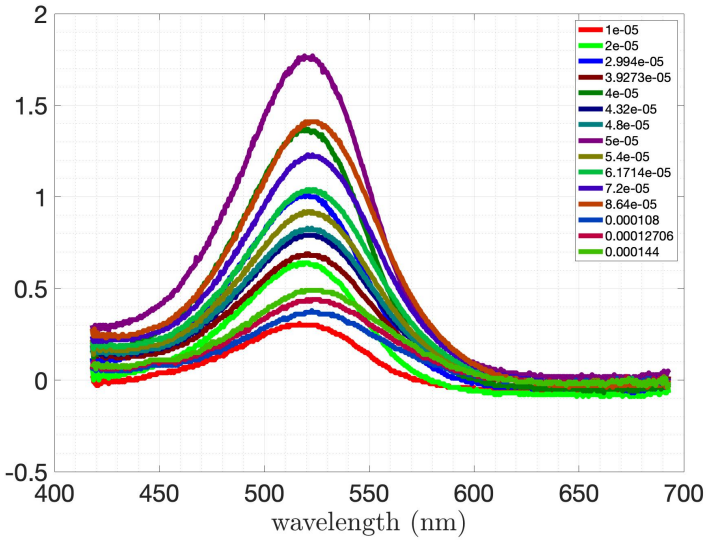

Figure 4.1: MSM (Malva sylvestris var. mauritiana) dried flower for concentrations from $1 \times 10^{-5}M$ to $1.44 \times 10^{-4}M$

An anthocyanin solution is comprised of a mixture of monomer, dimer, trimers, ... and large $j$mers, each of which has its own absorbance spectrum. The total measured absorbance depends on the wavelength-dependent absorbtivities $s_j(\lambda)$ of the $j$mers as well as the concentrations c_j of the $j$mers. According to the Beer–Lambert law, the absorbance expression

$$Abs = \ell \sum_j s_j c_j \tag{4.1}$$

where ℓ is the optical pathlength of the measured solution in the spectrometer.

Given an absorbance spectrum $Abs(\lambda)$ of a total concentration $T = \sum_j c_j$, we are interested in determining the absorbtivities $s_j(\lambda)$ of the various $j$mers. Recall from the introduction that association can potentially occur by stacking to form H associates or by joining molecules side-by-side to form J associates [24]. Comparing the wavelengths $\lambda_{max,j}$ at which the absorbtivities $s_j(\lambda)$ reach their maximum values provides a clue concerning the type of aggregation that occurs: If $\lambda_{max,1} < \lambda_{max,2}$ ($\lambda_{max,1} > \lambda_{max,2}$), we expect that dimers form via $H-$ ($J-$) association [24]. Given perfect data and a perfect model for association with known parameters, we could reconstruct the absorbtivities $s_j(\lambda)$ given $Abs_k(\lambda)$ at concentration T_k as follows: Using the Eq. 2.44 and $T_k = \sum_j c_j^k$ for c_j^k the concentration of $j$mers when the total concentration is T_k, we can rewrite Eq. 4.1 in the matrix form

$$\begin{pmatrix} Abs_1 \\ Abs_2 \\ \vdots \\ Abs_k \end{pmatrix} = \ell \begin{pmatrix} c_1^1 & c_2^1 & \cdots & c_j^1 \\ c_1^2 & c_2^2 & \cdots & c_j^2 \\ \vdots & \vdots & \ddots & \vdots \\ c_1^k & c_2^k & \cdots & c_j^k \end{pmatrix} \begin{pmatrix} s_1 \\ s_2 \\ \vdots \\ s_j \end{pmatrix}. \tag{4.2}$$

Hence, we can find the solution $(s_1\ s_2 \cdots s_j)^T$ of Eq. 4.2. This is what we called matrix method in finding s_j.

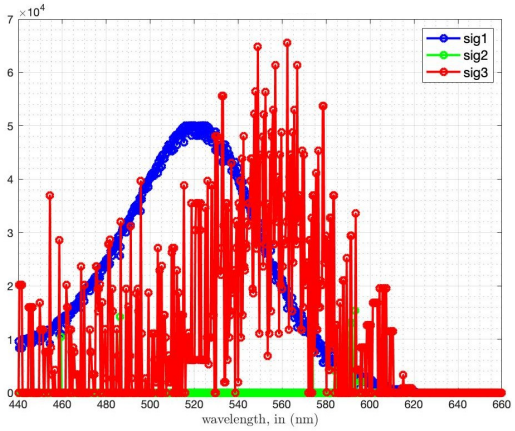

Figure 4.2: Matrix method in finding s_1,(blue curve) , s_2, (red curve) and s_3 (green curve) from part of the data in Figure 4.1.

The results Figure 4.2 in this example are not very convincing. We expect that $s_2 \approx 2s_1$. The reasons for the disappointing results are measurement errors in the spectra, the choice and measurement errors in the concentrations T_j, and sensitivity of the decomposition to these measurements. Another method to deconvolute the absorbance is to linear method, which is described in Section 4.3.2. Our goal is to develop an approach that allows us to report not only absorptivities $s_j(\lambda)$ constructed from a combination of our model, parameter choices in the model, and the data, but also let us report how certain we are of these absorptivities. Using a Bayesian inverse approach, we propose a method of determining a probability distribution for the absorptivties $s_j(\lambda)$. That is, for each j and λ, we give a probability distribution for the value $s_j(\lambda)$.

We will apply two methods in our Bayesian inversion approach. In the first, described in Section 4.2, we compute for each j and λ, a probability distribution for the value $s_j(\lambda)$. In the Second, we aim for probability distributions for the λ_{max} values for each $j$mers.

4.2 Bayesian Inversion

Given an absorbance spectrum $Abs_k(\lambda), 1 \leq k \leq N$, measured at total concentrations T_k, we assume that $Abs_k(\lambda) = \ell \sum_j s_j c_j^k$, where the concentrations c_j^k of the $j$mers obey the equilibrium solutions for isodesmic self association described, with association constant J, as studied in Section 2.4. Explicitly, we are using Eq. 2.30 and Eq. 2.31.

Recall that the c_j^k depend on the total concentration T_k. The goal is to find a posterior probability density (as functions of λ)

$$\sigma(\mathbf{m}(\lambda)|\mathbf{d})$$

for the parameters

$$\mathbf{m}(\lambda) = (s_i(\lambda))$$

for the given data $\mathbf{d} = \{(Abs_k(\lambda), T_k) : 1 \leq k \leq N\}$.

The Bayesian approach begins with Bayes' Theorem:

$$\sigma(\mathbf{m}|\mathbf{d}) \propto \underbrace{\rho_D(\mathbf{d}|\mathbf{m})}_{'likelihood'} \underbrace{\rho_M(\mathbf{m})}_{'prior'}, \tag{4.3}$$

where $\rho_D(\mathbf{d}|\mathbf{m})$ is the probability density, and $\rho_M(\mathbf{m})$ is known as the prior. $\rho_M(\mathbf{m})$ encodes what is known about the parameters a priori. In this case, we have, from experience with similar experimental measurements of absorbtivities, bounds on their values. We therefore take

$$\rho_M(\mathbf{m}) = \rho_M(s_1, s_2, \cdots, s_N) = \chi_{[v_{1,1},v_{1,2}]}(s_1)\chi_{[v_{2,1},v_{2,2}]}(s_2)\cdots\chi_{[v_{N,1},v_{N,2}]}(s_N), \tag{4.4}$$

where $v_{j,1}, v_{j,2}$ is the lower and upper bound of s_j, respectively, and χ is a characteristic function meaning $\chi_{[v_1,v_2]}(z) = 1$ if $z \in [v_1, v_2]$, and 0 otherwise. The likelihood $\rho_D(\mathbf{d}|\mathbf{m})$ describes how likely it would be to observe the measured data $\mathbf{d}$ given a set of parameter values $\mathbf{m}$. If we propose absorptivities s_j of different species, and write the parameter $\mathbf{m} = (s_j)$, then by the Eq. 4.1, we have the predicted absorbance $a(\mathbf{m})$. Taking a measure of uncertainty δ and using a probability density based on an inverted parabola from [76], we have the probability density

$$\rho_i(d_i|\mathbf{m}) = (1 - \frac{\mid d_i - a(\mathbf{m}) \mid^2}{\delta^2})\chi_{[a(\mathbf{m})-\delta, a(\mathbf{m})+\delta]}(d_i), \tag{4.5}$$

where χ is a characteristic function with the uncertainty parameter δ. Here, $\rho_i(d_i|\mathbf{m})$ describes the relative likelihood that predicted absorbance $a(\mathbf{m})$ for given fixed $\mathbf{m}$ is compatible with our experimental data d_i. Because we assume the measurement errors are statistically independent, the probability density that describes the collection of all measurements is a product of the densities for each measurement. That is,

$$\rho_D(\mathbf{d}|\ \mathbf{m}) = \prod_i \rho_i(d_i|\mathbf{m}). \tag{4.6}$$

Together with the prior $\rho_M(\mathbf{m})$, we find a posterior probability density

$$\sigma(\mathbf{m}|\mathbf{d}) = \kappa\rho_D(\mathbf{d}|\ \mathbf{m}) \times \rho_M(\mathbf{m}), \tag{4.7}$$

where κ is the normalization constant that makes $\int \sigma(\mathbf{m}|\mathbf{d}) = 1$.

4.2.1 Expected values and standard deviations

By Eq. 4.7, $\sigma(\mathbf{m}|\mathbf{d})$ can derive the maximum a posteriori

$$\mathbf{m}_{MAP} = arg\ \max_{\mathbf{m}} \sigma(\mathbf{m}|\mathbf{d}). \tag{4.8}$$

If we only consider two parameter s_1 and s_2, then the expected values are

$$\mathbf{E}(s_1) = \sum_{s_1\ grid} \sum_{s_2\ grid} s_1\sigma(\mathbf{m}|\mathbf{d}) \tag{4.9}$$

$$\mathbf{E}(s_2) = \sum_{s_1\ grid} \sum_{s_2\ grid} s_2\sigma(\mathbf{m}|\mathbf{d}). \tag{4.10}$$

Also, the standard deviations can be calculated by

$$std(s_1|\mathbf{d}) = \sqrt{\sum_{s_1\ grid} \sum_{s_2\ grid} (s_1 - \mathbf{E}(s_1))^2\sigma(\mathbf{m}|\mathbf{d})}, \tag{4.11}$$

$$std(s_2|\mathbf{d}) = \sqrt{\sum_{s_1\ grid} \sum_{s_2\ grid} (s_2 - \mathbf{E}(s_2))^2\sigma(\mathbf{m}|\mathbf{d})}. \tag{4.12}$$

Recall that the 68.26% and 90% confidence interval for s_j is $[\mathbf{E}(s_j) - std(s_j), \mathbf{E}(s_j) + std(s_j)]$, and $[\mathbf{E}(s_j) - 1.645 \times std(s_j), \mathbf{E}(s_j) + 1.645 \times std(s_j)]$, respectively. We will use expected values and standard deviations to find the confidence intervals for our deserved parameters.

4.2.2 Constructing *in silico* data

We can use *in silico* (made up) data to test our method. We assume the monomer, dimer, trimer, quadramer and 5-mer absorptivities to be Gaussian distributions $\exp(-\frac{1}{2}\frac{(\lambda-\lambda_{max})^2}{variance^2})$; see Figure 4.3a. The Beer-Lambert Law, Eq. 4.1, gives the (ideal) absorbance as a function of concentration given these assumed n-mer absorptivities. To mimic measurement error, we multiply the ideal absorbance by $1 \pm 0.07 \times rand$, where $rand$ are random numbers with the mean value 0 and the standard deviation 1. Hence, we can observe the absorbance data like Figure 4.3b. There aborbance data are the *in silico* data we used to test the Bayesian method.

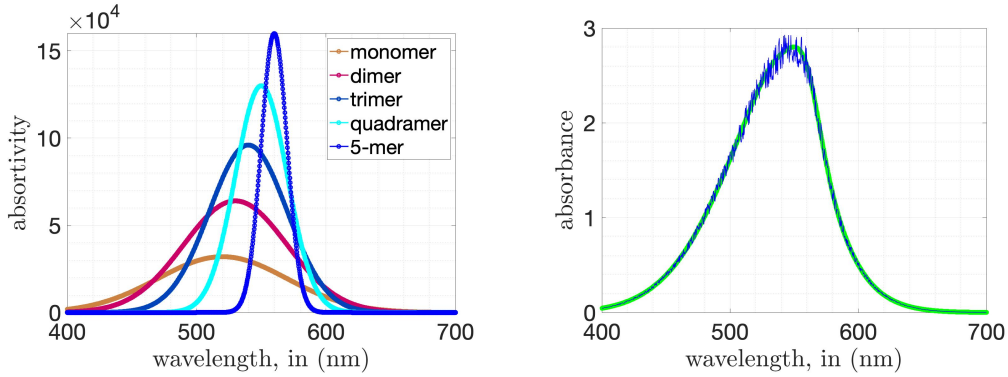

(a) *In silico* absorptivities. **(b)** *In silico* absorbance.

Figure 4.3: *In silico* absorptivities and absorbance data. (b) By the Beer–Lambert law Eq. 4.1, we can calculate the absorbance at the concentration 10^{-4}M, and we graph this ideal absorbance in green. Perturb this ideal absorbance by multiplying $1 \pm 0.07 \times rand$, where $rand$ are random numbers with the mean value 0 and the standard deviation 1, we observe *in silico* absorbance, which is graphed in blue.

First, we consider the absorptivity of wavelength 520 nm and assume there are only monomers and dimers in the compound by assuming that the spectra of all wavelengths are independent random variables. Preliminary experiments showed the monomer absorptivity s_1 of wavelength 520 nm is on the interval $[3 \times 10^4, 4 \times 10^4]$. By the fact that the maximum absorptivity of dimer being approximately to two times the maximum absorptivity of monomer, we assume that the dimer absorptivity s_2 on the same wavelength is on the interval $[0 \times 10^4, 8 \times 10^4]$.

If we have n_1 grid points in s_1 direction and n_2 in s_2, pick $\delta = 0.7$, and we have some *in silico* data pairs $\{(T_i, d_i)\}$ for the optical path length $\ell = 1$, where T_i is the total concentration and d_i

represents the absorbance measurement, then we use T_i to calculate predicted $a_i(\mathbf{m}) = \ell(s_1c_1 + s_2c_2/2)$ for each grid point by the relations $T_i = c_1 + c_2$ and $c_2 = 2J \times c_1^2$, where J is the association constant. Use Eq. 4.5 and measurement d_i to find out the probability density $\rho_i(d_i|\mathbf{m})$ for each data pair. Then a product through each pair $\{(T_i, d_i)\}$ is the probability density $\sigma(\mathbf{m}|\mathbf{d})$ for each grid point.

Here, we use the total concentrations from $5 \times 10^{-5} M$ to $3 \times 10^{-4} M$ of the *in silico* data, which has association constant $J = 5000$. We then put all these data pairs into the Bayesian method and graph the probability distribution of monomer and dimer absorptivities with the expected value E and the standard deviation Std as Figure 4.4, where we set the association constant to be $J = 15000$.

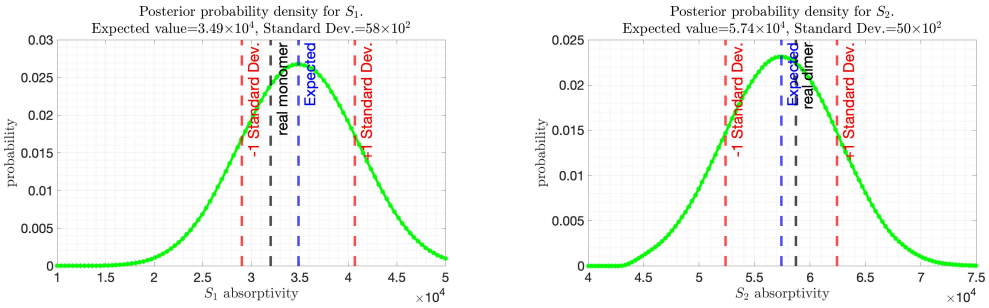

(a) Monomer. **(b)** Dimer.

Figure 4.4: The probability distribution of monomer and dimer absorptivities on one wavelength by Bayesian method.

We found that both of the real absorptivities are in the interval $[E - 1 \times Std, E + 1 \times Std]$. That is, 68.26% confidence intervals include the real monomer and dimer absorptivities, which means this method works for finding absorptivities when we only consider one wavelength even though we are using different association constants J.

Now, we would like to find the absorptivities at all wavelengths. Here we use the *in silico* data which are the ideal absorbance by multiplying $1 \pm 0.01 \times rand$, where $rand$ are random numbers with the mean value 0 and the standard deviation 1. We will use the Bayesian method in a very similar way as was done for one wavelength. But in this time, we just regard the data of the total

concentration $5 \times 10^{-6} M$ as the monomer absorptivity, because there should be only monomer in the this low concentration. See Figure 4.5.

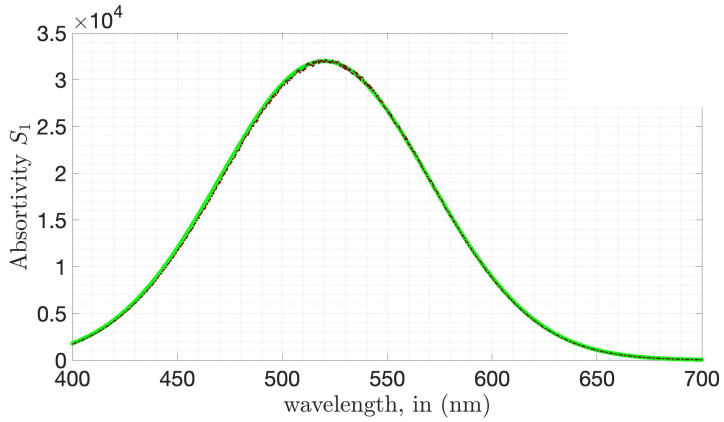

Figure 4.5: The actual value of monomer absorptivity, which is graphed in green. The ideal absorbance of 5×10^{-6}M multiplying $1 \pm 0.01 \times rand$, where $rand$ are random numbers with the mean value 0 and the standard deviation 1, and then divided by 5×10^{-6} (its concentration), which is graphed in red.

Applying the Bayesian inverse method to the *in silico* data of the concentrations $1 \times 10^{-5} M$, $5 \times 10^{-5} M$, $1 \times 10^{-4} M$, $1.5 \times 10^{-4} M$, $2 \times 10^{-4} M$, and $3 \times 10^{-4} M$, we find the dimer and trimer absorptivities of whole wavelengths when assuming the association constant $J = 15000$, shown in Figure 4.6. The blue curves are the real dimer and trimer absorptivities. We use green interval to represent ± 1 standard deviation from the expected values, which are represented as the red curves.

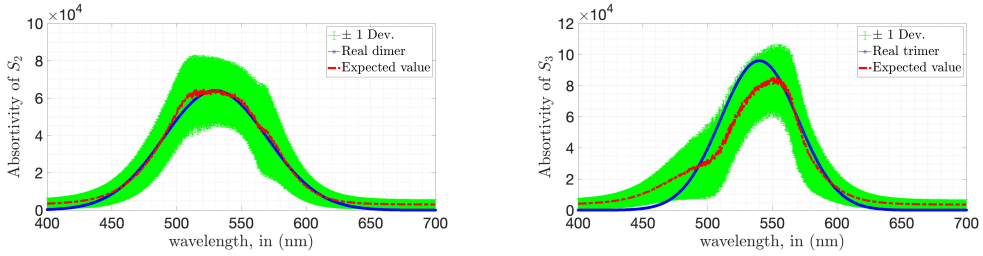

(a) Dimer. **(b)** Trimer.

Figure 4.6: The dimer and trimer absorptivities of all wavelengths by Bayesian method.

We realized that these 68.26% confidence intervals cover the real absorptivities of dimer and trimer of whole wavelengths. This provides evidence that this method is trustworthy.

4.2.3 Experimental data

In this subsection, we apply the Bayesian inverse method to experimental data measured by Dr. Thompson, which are exacted from plumbago at pH$= 1.31$. The data set consists of absorbance of anthocyanin solutions at various concentrations, namely $6.5 \times 10^{-6}M, 1.25 \times 10^{-5}M, 2.5 \times 10^{-5}M, 5 \times 10^{-5}M, 10^{-4}M$. Because the solutions were buffered to be at pH$= 1.31$, we can assume that the anthocyanins are in the form of AH^+ or its association forms. At the total concentration $6.5 \times 10^{-6}M$, we regard the data of absorbance as the monomer absorptivity of AH^+ since the concentration is not high enough to associate (assuming that our model and estimated equilibrium constants are correct). Then we used the data of the same pH value but different concentrations, which are $1.25 \times 10^{-5}M, 2.5 \times 10^{-5}M, 5 \times 10^{-5}M$ and $10^{-4}M$. If we pick the association constant $J = 15000$, and compare the different measure of uncertainty parameter δ in Eq. 4.5, then the results are shown in Figure 4.7.

Here we found the peak of the dimer absorbtivtiy, which is around $565(um)$, is at the longer wavelength than the peak of the monomer absorbtivtiy, which is around $530(um)$. Note that the self association may potentially occur by stacking to form H aggregrates or end-to-end bonding to form J aggregates. From previous studies [24, 77], we know that the spectra of J- (H-) aggregates to be shifted to longer (shorter) wavelengths with respect to the monomer. Hence, these results show $[AH_2^+]$ and $[AH_3^+]$ are J-aggregates because the peaks are shifted to the longer wavelength.

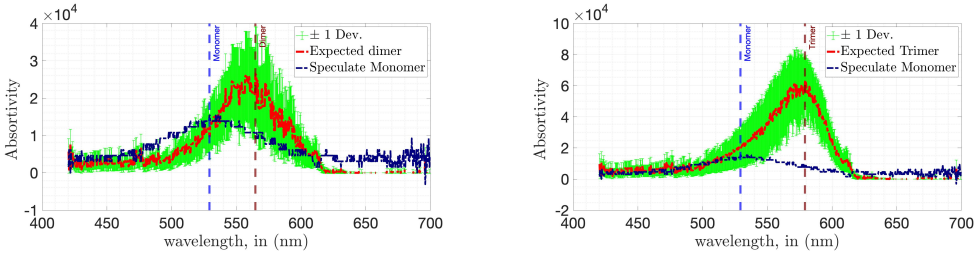

(a) $\delta = 0.1$, Dimer.

(b) $\delta = 0.1$, Trimer.

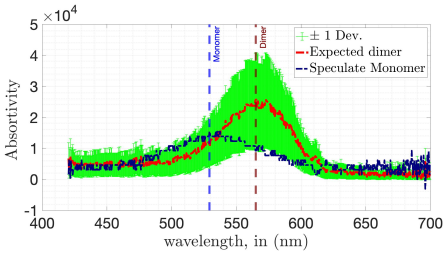

(c) $\delta = 0.3$, Dimer.

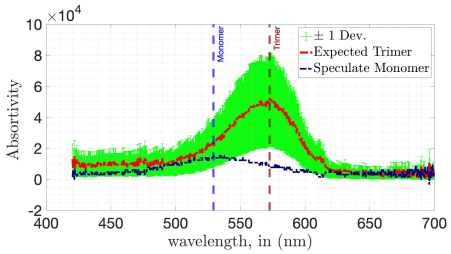

(d) $\delta = 0.3$, Trimer.

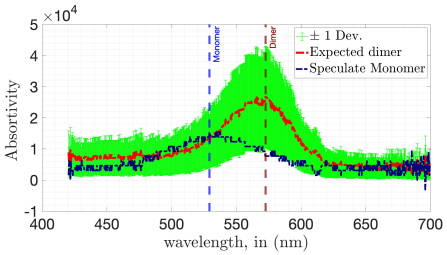

(e) $\delta = 0.5$, Dimer.

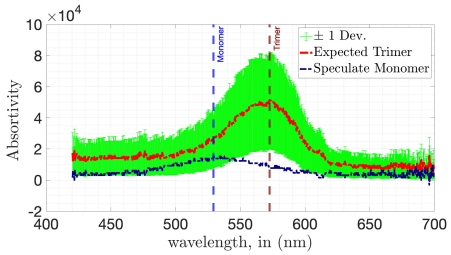

(f) $\delta = 0.5$, Trimer.

Figure 4.7: The absorptivities of dimer and trimer of AH^+ constructed by Bayesian inverse method. The red curves are the expected values for the dimer or trimer absorptivities (as labelled), the green intervals are the 68.26% confidence intervals, and the dark blue curve is the speculated monomer absorptivity using the absorbance of the concentration $6.5 \times 10^{-6} M$. The blue vertical line is the maximum absorptivity of monomer and the red vertical line is the maximum absorptivity of dimer or trimer (as labelled).

4.3 Gaussian functions

In the Subsection 4.2, we assume the spectra of all wavelengths are independent random variables. This is true, but the absorptivity over wavelengths should be continuous and bell-shaped. We propose another way to find absorptivities. We can assume that the absorptivity is a Gaussian function of wavelength with expected value μ, variance σ, and amplitude amp. Similarly using the Bayesian inverse method to find the confidence intervals of these μ, σ, and amp, we can figure out the expected peaks of $n-$mers absorptivity is moving to the right or left. This will give us evidence to show the self associations are J- or H-aggregates.

We will apply the Bayesian inverse method similarly here. But in this subsection, we are considering the parameters

$$\mathbf{m} = (\mu_i, \sigma_i, amp_i),$$

where μ_i, σ_i, and amp_i represent the expected value, variance, and amplitude, respectively, of $i$mer absorptivity if we regard the absorptivity as a Gaussian function of the wavelength λ. Our goal is to find a posterior probability density $\sigma(\mathbf{m}|\mathbf{d})$ for the given data $\mathbf{d} = \{(Abs_k(\lambda), T_k) : 1 \leq k \leq N\}$. By the Eq. 4.3, we need to set up the likelihood $\rho_D(\mathbf{d}|\mathbf{m})$ and the prior $\rho_M(\mathbf{m})$. We will treat the data in a similar way as we do in the Subsection 4.2.1, which is regarding the absorbance of the lowest concentration as the monomer absorptivity. Then we know the variance σ_1 and amplitude amp_1 of the monomer. To find the prior $\rho_M(\mathbf{m})$, we assume the expected value μ_i uniformly distributed on the interval $[500, 600]$, which is the peak wavelength in nanometers, the variance σ_i uniformly distributed on the interval $[\sigma_1 - 10, \sigma_1 + 10]$, and the amplitude amp_i uniformly distributed on the interval $[i \times amp_1 - 10^4, i \times amp_1 + 10^4]$. For each parameter $\mathbf{m} = (\mu_i, \sigma_i, amp_i)$, we can propose absorptivities $s_j(\lambda)$ of $j$mers

$$s_j(\lambda) = amp_j \times \exp\left(-\frac{(\lambda - \mu_j)^2}{2\sigma_j^2}\right). \tag{4.13}$$

By Eq. 4.1, we have the predicted absorbance $a(\mathbf{m})$. Then the probability density is the same as Eq. 4.5, and the likelihood $\rho_D(\mathbf{d}|\mathbf{m})$ is in Eq. 4.6.

4.3.1 *In silico* data

We again use the *in silico* noisy data in Subsection 4.2.2, for which the association constant is 2.5×10^4, to test our method is working or not. The lowest concentration in the data set is $5 \times 10^{-6}M$, chosen so that the anthocyanins are essentially all in monomer form. Therefore, the measured absorbance would give the monomer absorptivity. We find a Gaussian function that fits these data as follows: For the value of λ, say $\lambda_{1,\max}$, that gives the maximum absorptivity, $s_{1,\max}$, we find the function of the form $s_j(\lambda) = s_{1,\max} \exp\left(-\frac{(\lambda-\lambda_{1,\max})^2}{2\sigma_1^2}\right)$ that best fits the data. We take this function to be the monomer absorptivity. See Figure 4.8.

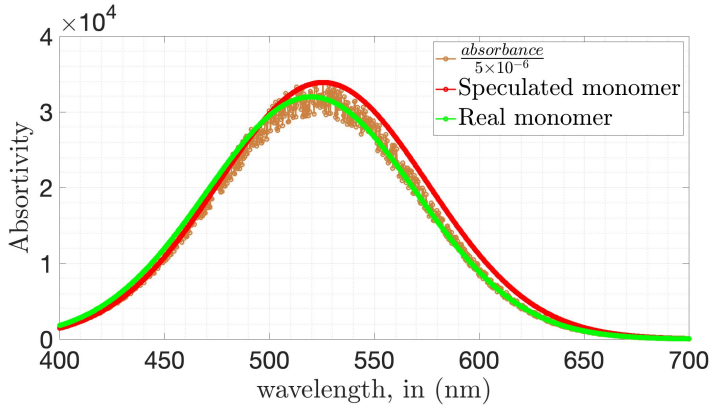

Figure 4.8: The absorbance of 5×10^{-6}M divided by its concentration, the speculated monomer absorptivity in Gaussian function, and the real monomer absorptivity.

Here, we take the uncertainty parameter $\delta = 10^{-2}$, applying the Bayesian inverse method to the *in silico* data of the eight concentrations from $1 \times 10^{-5}M$ to $8 \times 10^{-5}M$. We compare the dimer absorptivity when choosing different association constants J and concentrations of data, shown in Figure 4.9 to Figure 4.14. The green curves are probability distributions of the peak wavelength of the dimer absorptivity. The blue vertical line is the expected value, the red vertical lines represent ± 1 standard deviations from the expected value, and the black vertical line is the ground truth

(actual dimer). The brown interval is the 90% confidence interval. We found that we might have a smaller confidence interval if we take more data. However, when we used some higher concentrations to construct the dimer absorptivity, we might have some results not consistent with the fact because there should have more trimer that cannot be ignored. Hence, we will suggest using the concentrations from $1 \times 10^{-5}M$ to $4 \times 10^{-5}M$ is better to construct the dimer absorptivity. In order to have a smaller confidence interval, we can use larger association constant J. In our *in silico* data, the association constant $J = 25000$. We can have satisfactory results by applying $J = 25000$, see Figure 4.9, but we will have a better outcome for $J = 75000$, see Figure 4.11. For these data, $\lambda_{1,\max} = 526$. If this value is outside of the 90% confidence interval, then we can say with confidence that dimerization has produced a shift to larger wavelengths. Recall that anthocyanin association may potentially occur by stacking (to form H associates) or end-to-end bonding (to form J associates). One expects the spectra of $H-$ (J) associates to be shifted to shorter (longer) wavelengths with respect to the monomer. [24], [77].

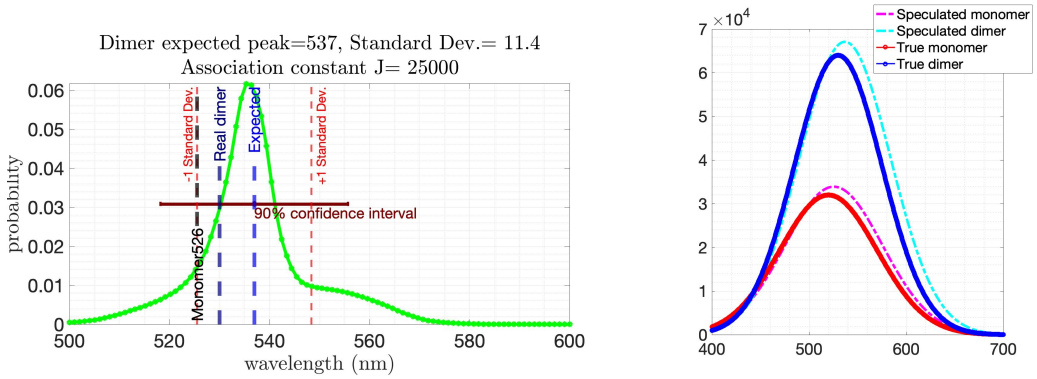

(a) The probability distribution of $\lambda_{2,\max}$, computed using the Bayesian method.

(b) True and Speculated monomer and dimer curves.

Figure 4.9: The dimer absorptivity when $J = 25000$ using 4 data of the concentrations from $1 \times 10^{-5}M$ to $4 \times 10^{-5}M$. The 90% confidence interval includes both the true dimer and $\lambda_{1,\max}$.

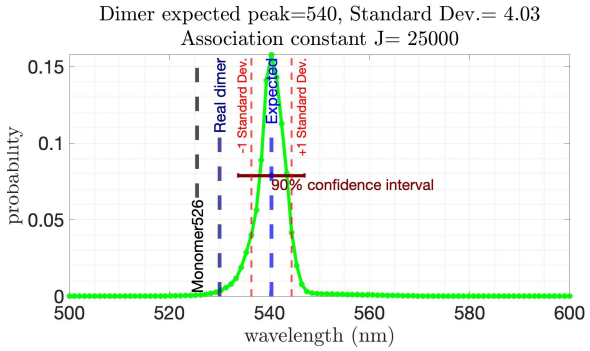

(a) The probability distribution of $\lambda_{2,\max}$, computed using the Bayesian method.

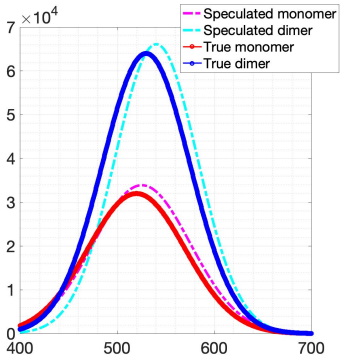

(b) Real and Speculated monomer and dimer curves.

Figure 4.10: The dimer absorptivity when $J = 25000$ using 8 data of the concentrations from $1 \times 10^{-5}M$ to $8 \times 10^{-5}M$. The 90% confidence interval does not cover the true dimer, neither $\lambda_{1,\max}$.

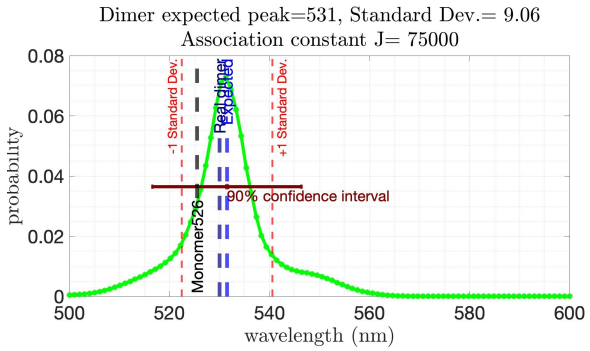

(a) The probability distribution of $\lambda_{2,\max}$, computed using the Bayesian method.

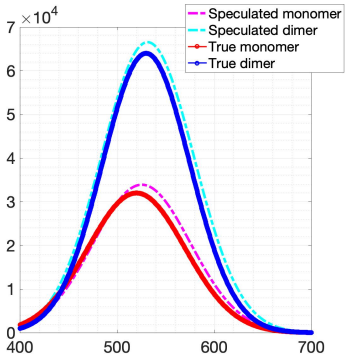

(b) True and Speculated monomer and dimer curves.

Figure 4.11: The dimer absorptivity when $J = 75000$ using 4 data of the concentrations from $1 \times 10^{-5}M$ to $4 \times 10^{-5}M$. The 90% confidence interval includes both the true dimer and $\lambda_{1,\max}$.

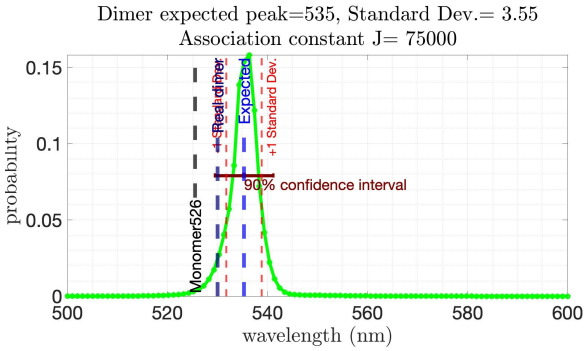

(a) The probability distribution of $\lambda_{2,\max}$, computed using the Bayesian method.

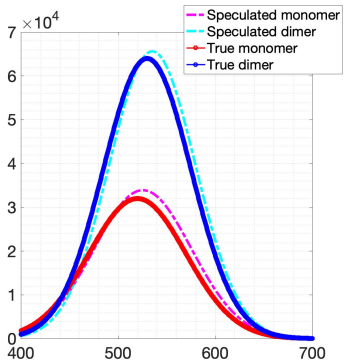

(b) True and Speculated monomer and dimer curves.

Figure 4.12: The dimer absorptivity when $J = 75000$ using 8 data of the concentrations from $1 \times 10^{-5}M$ to $8 \times 10^{-5}M$. The 90% confidence interval includes the true dimer, but not cover $\lambda_{1,\max}$. This means we can say with confidence that $\lambda_{1,\max} < \lambda_{2,\max}$.

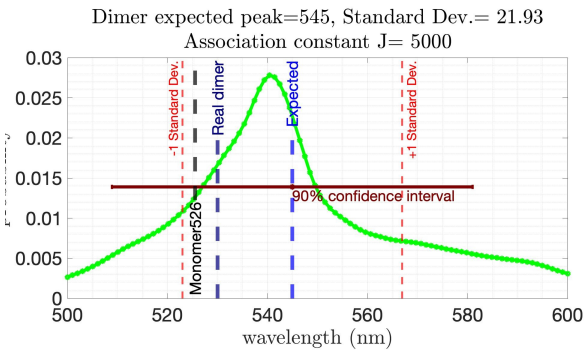

(a) The probability distribution of $\lambda_{2,\max}$, computed using the Bayesian method.

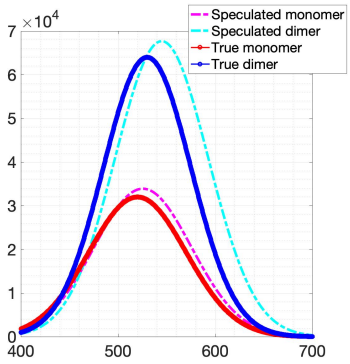

(b) True and Speculated monomer and dimer curves.

Figure 4.13: The dimer absorptivity when $J = 5000$ using 4 data of the concentrations from $1 \times 10^{-5}M$ to $4 \times 10^{-5}M$. The 90% confidence interval includes both the true dimer and $\lambda_{1,\max}$.

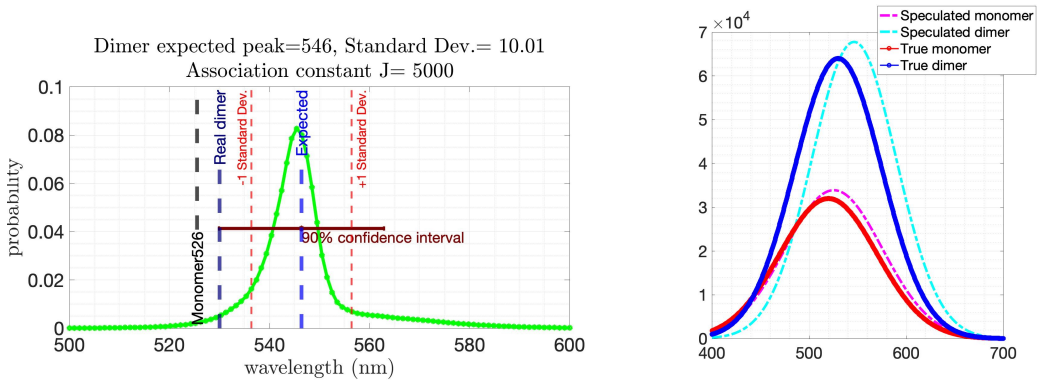

(a) The probability distribution of $\lambda_{2,\max}$, computed using the Bayesian method.

(b) True and Speculated monomer and dimer curves.

Figure 4.14: The dimer absorptivity when $J = 5000$ using 8 data of the concentrations from $1 \times 10^{-5}M$ to $8 \times 10^{-5}M$. The 90% confidence interval includes the true dimer, but not cover $\lambda_{1,\max}$. This means we can say with confidence that $\lambda_{1,\max} < \lambda_{2,\max}$.

4.3.2 Experimental data

In this subsection, we apply the Bayesian inverse method of Gaussian function to experimental data measured by Dr. Thompson. Dr. Thompson produced extracts of *Malva sylvestris var. mauritiana* dried flowers. The extracts were placed in $0.1M$ HCl solutions to keep them at approximately pH$= 1.008$. The data set, see Figure 4.1, consists of absorbance spectra of anthocyanin solutions at various concentrations, namely $5 \times 10^{-6}M, 1 \times 10^{-5}M, 2 \times 10^{-5}M, 2.994 \times 10^{-5}M, 3.927 \times 10^{-5}M, 4 \times 10^{-5}M, 4.32 \times 10^{-5}M, 4.8 \times 10^{-5}M, 5 \times 10^{-5}M, 5.4 \times 10^{-5}M$, and $6.17 \times 10^{-5}M$. Similarly, we use the best-fit Gaussian function of the data of the concentration $5 \times 10^{-6}M$ to be the monomer absorptivity, as shown in Figure 4.15.

Taking the uncertainty parameter $\delta = 10^{-2}$, we use the concentrations from $1 \times 10^{-5}M$ to $6 \times 10^{-5}M$ to find the dimer absorptivity. When we use different association constant J, we can have different length of the confidence interval. Here, we will compare the results with the linear method. The linear method is using

$$T = c_1 + 2 \times c_2$$

$$c_2 = Jc_1^2,$$

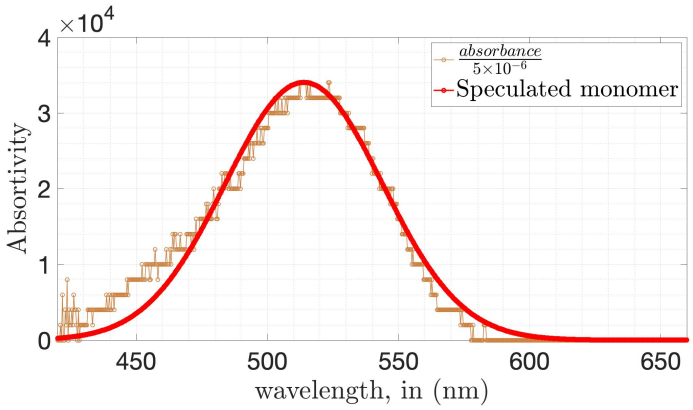

Figure 4.15: The absorbance of 5×10^{-6}M divided by its concentration, and the speculated monomer absorptivity as a Gaussian function.

where T is the total concentration, c_1 and c_2 represent the concentration of monomer and dimer, respectively. Solving $2Jc_1^2 + c_1 = T$ for c_1, we have

$$c_1 = \frac{-2 \pm \sqrt{1 + 8JT}}{4J}.$$

By Eq. 4.1, we have the dimer absorptivity s_2 when substituting the monomer absorptivity s_1 and concentration c_1. Hence, if we assume the monomer absorptivity s_1 equals the absorbance of the lowest concentration divided by its concentration, we can apply this linear method to find the dimer absorptivity s_2 by the other absorbance data of concentrations. We are applying the concentration of $2.994 \times 10^{-5}M$ to construct the dimer absorptivity s_2 by linear method.

Here we have several observations. First, the Bayesian method and the linear method are mostly consistent. But when the concentrations go up to $6 \times 10^{-5}M$, the higher concentrations include higher $j$mers such as trimer, the dimer curves will be affected and have some shift; see Figure 4.18b and Figure 4.24b. Secondly, if we restrict the concentrations to be less or equal to $5 \times 10^{-5}M$, then we can have the smaller standard deviation when we choose the larger association constant J. However, if we chose a different association constant, the expected peak might change as well, which means the results will be influenced by the association constant J. Also, we can see the probability distributions in Figure 4.16a - Figure 4.21a have multiple peaks, which is not consistent

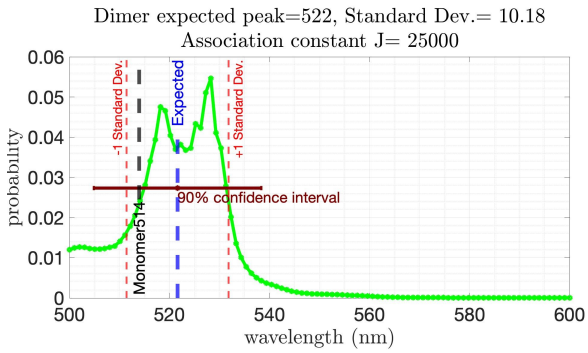

(a) The probability distribution of $\lambda_{2,\max}$, computed using the Bayesian method.

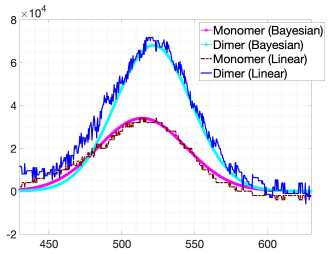

(b) Monomer and dimer curves computed from experimental data using Bayesian and linear methods.

Figure 4.16: Absorptivity of anthocyanin monomers and dimers from extracts of *Malva sylvestris var. mauritiana*, computed from absorbance curves of solutions at the 5 concentrations $C \times 10^{-5}M$ for $C = 1, 2, 2.994, 3.927, 4$. The association constant was assumed to be $J = 25000$.

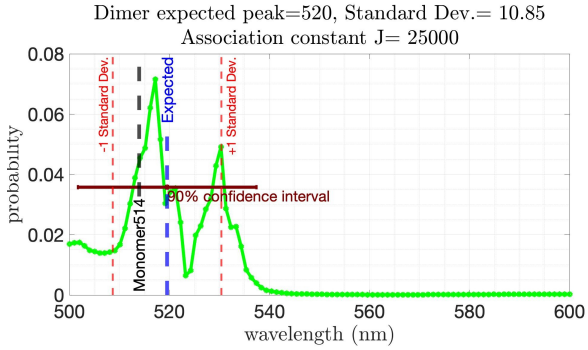

(a) The probability distribution of $\lambda_{2,\max}$, computed using the Bayesian method.

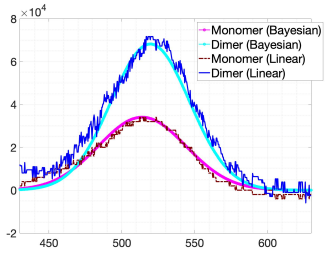

(b) Monomer and dimer curves computed from experimental data using Bayesian and linear methods.

Figure 4.17: Absorptivity of anthocyanin monomers and dimers from extracts of *Malva sylvestris var. mauritiana*, computed from absorbance curves of solutions at the 8 concentrations $C \times 10^{-5}M$ for $C = 1, 2, 2.994, 3.927, 4, 4.32, 4.8, 5$. The association constant was assumed to be $J = 25000$.

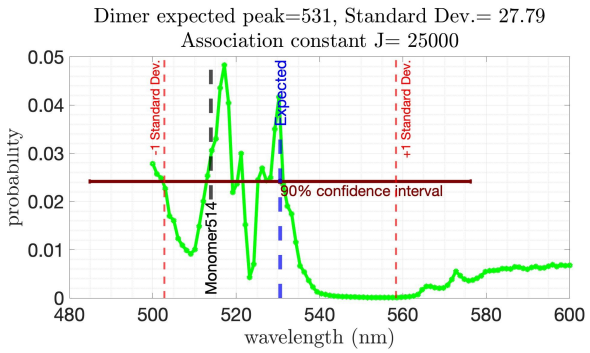

(a) The probability distribution of $\lambda_{2,\max}$, computed using the Bayesian method.

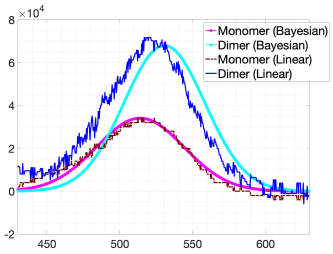

(b) Monomer and dimer curves computed from experimental data using Bayesian and linear methods.

Figure 4.18: Absorptivity of anthocyanin monomers and dimers from extracts of *Malva sylvestris var. mauritiana*, computed from absorbance curves of solutions at the 10 concentrations $C \times 10^{-5} M$ for $C = 1, 2, 2.994, 3.927, 4, 4.32, 4.8, 5, 5.4, 6.17$. The association constant was assumed to be $J = 25000$.

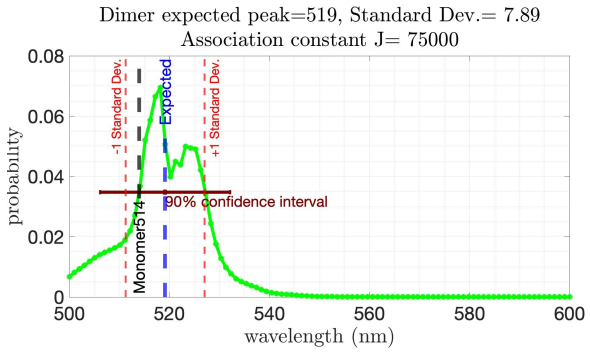

(a) The probability distribution of $\lambda_{2,\max}$, computed using the Bayesian method.

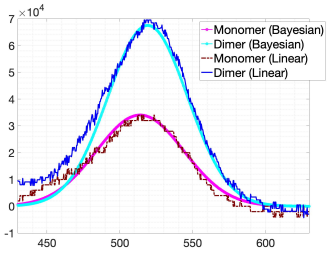

(b) Monomer and dimer curves computed from experimental data using Bayesian and linear methods.

Figure 4.19: Absorptivity of anthocyanin monomers and dimers from extracts of *Malva sylvestris var. mauritiana*, computed from absorbance curves of solutions at the 5 concentrations $C \times 10^{-5} M$ for $C = 1, 2, 2.994, 3.927, 4$. The association constant was assumed to be $J = 75000$.

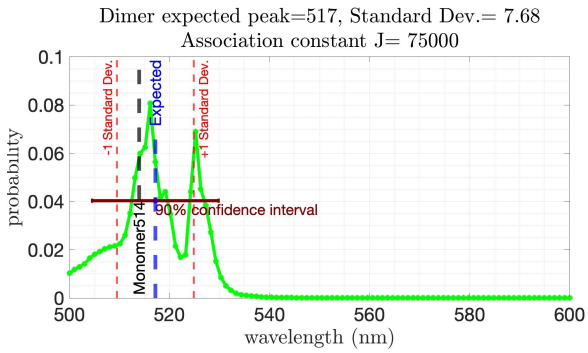

(a) The probability distribution of $\lambda_{2,\max}$, computed using the Bayesian method.

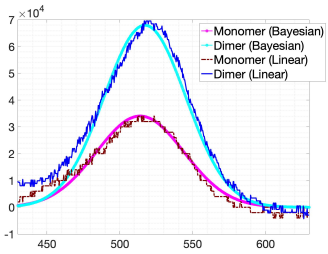

(b) Monomer and dimer curves computed from experimental data using Bayesian and linear methods.

Figure 4.20: Absorptivity of anthocyanin monomers and dimers from extracts of *Malva sylvestris var. mauritiana*, computed from absorbance curves of solutions at the 8 concentrations $C \times 10^{-5}M$ for $C = 1, 2, 2.994, 3.927, 4, 4.32, 4.8, 5$. The association constant was assumed to be $J = 75000$.

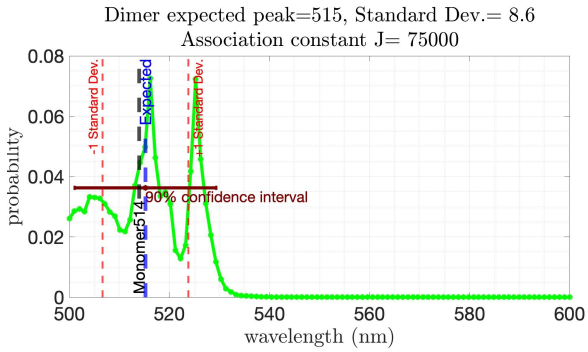

(a) The probability distribution of $\lambda_{2,\max}$, computed using the Bayesian method.

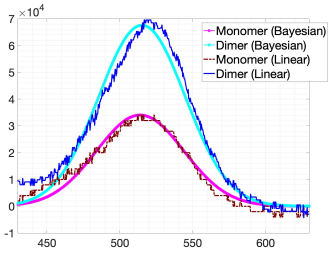

(b) Monomer and dimer curves computed from experimental data using Bayesian and linear methods.

Figure 4.21: Absorptivity of anthocyanin monomers and dimers from extracts of *Malva sylvestris var. mauritiana*, computed from absorbance curves of solutions at the 10 concentrations $C \times 10^{-5}M$ for $C = 1, 2, 2.994, 3.927, 4, 4.32, 4.8, 5, 5.4, 6.17$. The association constant was assumed to be $J = 75000$.

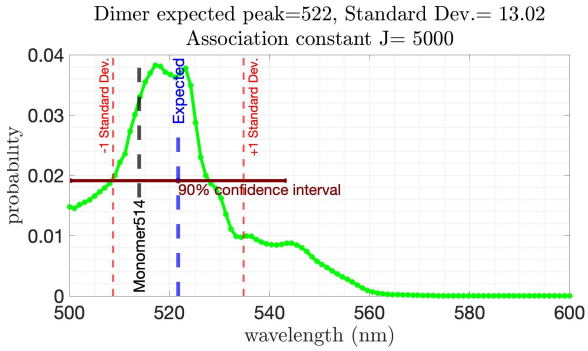

(a) The probability distribution of $\lambda_{2,\max}$, computed using the Bayesian method.

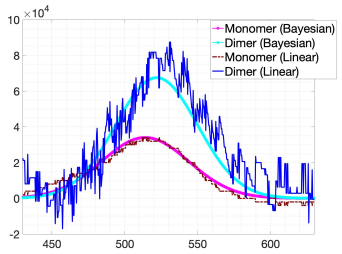

(b) Monomer and dimer curves computed from experimental data using Bayesian and linear methods.

Figure 4.22: Absorptivity of anthocyanin monomers and dimers from extracts of *Malva sylvestris var. mauritiana*, computed from absorbance curves of solutions at the 5 concentrations $C \times 10^{-5}M$ for $C = 1, 2, 2.994, 3.927, 4$. The association constant was assumed to be $J = 5000$.

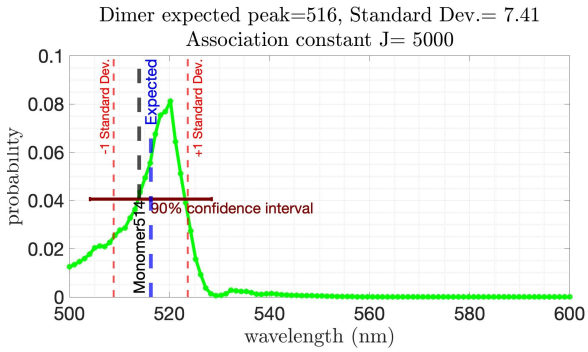

(a) The probability distribution of $\lambda_{2,\max}$, computed using the Bayesian method.

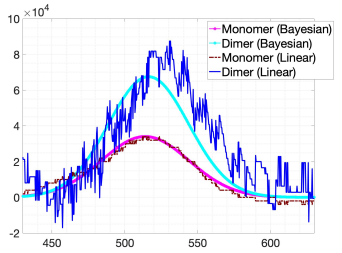

(b) Monomer and dimer curves computed from experimental data using Bayesian and linear methods.

Figure 4.23: Absorptivity of anthocyanin monomers and dimers from extracts of *Malva sylvestris var. mauritiana*, computed from absorbance curves of solutions at the 8 concentrations $C \times 10^{-5}M$ for $C = 1, 2, 2.994, 3.927, 4, 4.32, 4.8, 5$. The association constant was assumed to be $J = 5000$.

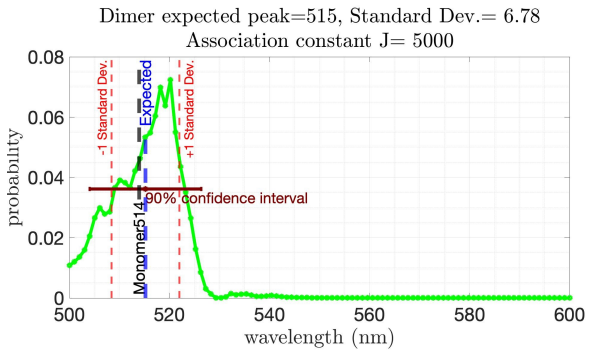

(a) The probability distribution of $\lambda_{2,\max}$, computed using the Bayesian method.

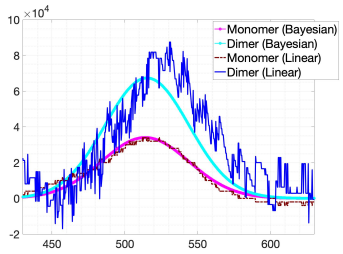

(b) Monomer and dimer curves computed from experimental data using Bayesian and linear methods.

Figure 4.24: Absorptivity of anthocyanin monomers and dimers from extracts of *Malva sylvestris var. mauritiana*, computed from absorbance curves of solutions at the 10 concentrations $C \times 10^{-5}M$ for $C = 1, 2, 2.994, 3.927, 4, 4.32, 4.8, 5, 5.4, 6.17$. The association constant was assumed to be $J = 5000$.

with *in silico* results such as those shown in Figure 4.9a- Figure 4.14a. We expect our probability distributions will have only one peak if we use the suitable data set.

Suggested experimental studies

Using the data of the concentration $5 \times 10^{-6}M$, we can have the speculated monomer absorptivity. In order to separate the $\lambda_{2,\max}$ from the $\lambda_{1,\max}$, we suggest to have 10 experiments at the concentrations from $1 \times 10^{-5}M$ to $3 \times 10^{-5}M$. These will be enough to have $\lambda_{1,\max}$ outside the 90% confidence interval of $\lambda_{2,\max}$ even though the real distance between $\lambda_{1,\max}$ and $\lambda_{2,\max}$ is as close as $5(nm)$. See Figure 4.25. We construct *in silico* absorptivities which the distance between $\lambda_{1,\max}$ and $\lambda_{2,\max}$ is $5(nm)$. When we use 10 data of the concentrations from $1 \times 10^{-5}M$ to $3 \times 10^{-5}M$, we can have $\lambda_{1,\max}$ outside the 90% confidence interval of $\lambda_{2,\max}$.

4.3.3 Conclusions and Further Work

In this section, we developed a Bayesian method of deconvoluting spectral data. Using absorbance spectra of anthocyanin solutions at various concentrations, together with a model for self association, we produce probability distributions for the peak absorbance wavelengths $\lambda_{\max}$ for monomers and dimers.

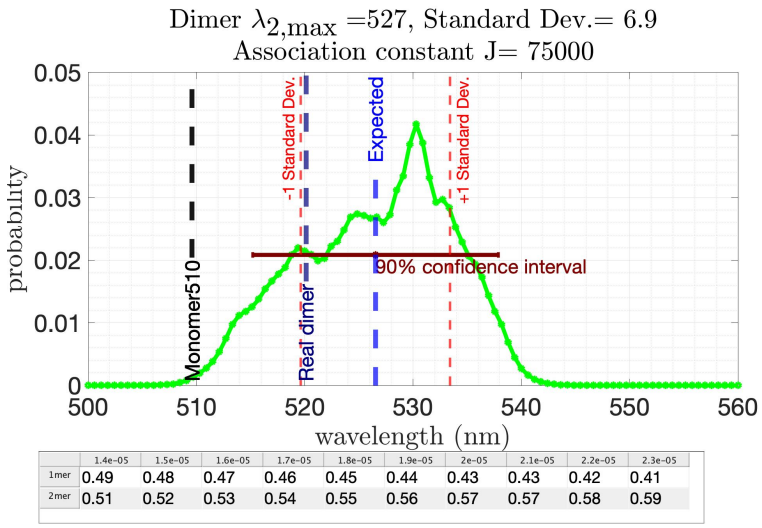

	1.4e-05	1.5e-05	1.6e-05	1.7e-05	1.8e-05	1.9e-05	2e-05	2.1e-05	2.2e-05	2.3e-05
1mer	0.49	0.48	0.47	0.46	0.45	0.44	0.43	0.43	0.42	0.41
2mer	0.51	0.52	0.53	0.54	0.55	0.56	0.57	0.57	0.58	0.59

Figure 4.25: The probability distribution of $\lambda_{2,\max}$ *In silico* data. Using 10 data of the concentrations from $1 \times 10^{-5}M$ to $3 \times 10^{-5}M$. The 90% confidence interval includes the real dimer, but not cover $\lambda_{1,\max}$. This means we can say with confidence that $\lambda_{1,\max} < \lambda_{2,\max}$.

Achieving a result in which the peak absorbance wavelengths $\lambda_{1,\max}$ for the monomer and $\lambda_{2,\max}$ for the dimer requires anthocyanin solutions that are of very low concentrations. We have analyzed preliminary results involving 5 absorbance spectra at low concentrations. This was not sufficient for the confidence interval corresponding to the $\lambda_{2,\max}$ probability distribution to be small enough for us to state with confidence that $\lambda_{2,\max} > \lambda_{1,\max}$. We have proposed that further measurements at low concentrations will allow for a smaller confidence interval. The Laboratory for Mathematics in the Sciences has acquired a new spectrometer that is sensitive even at low concentrations; this should allow for the proposed measurements to be made.

Bibliography

[1] D. W. Lee and K. S. Gould. Anthocyanins in leaves and other vegetative organs: an introduction. 2002.

[2] B. Alappat and J. Alappat. Anthocyanin pigments: Beyond aesthetics. *Molecules*, 25(23):5500, 2020.

[3] T. S. Feild, D. W. Lee, and N. M. Holbrook. Why leaves turn red in autumn. the role of anthocyanins in senescing leaves of red-osier dogwood. *Plant physiology*, 127(2):566–574, 2001.

[4] P. Ferreira da Silva, L. Paulo, A. Barbafina, F. Elisei, F. H. Quina, and A. L. Maçanita. Photoprotection and the photophysics of acylated anthocyanins. *Chemistry–A European Journal*, 18(12):3736–3744, 2012.

[5] X. T. Zheng, Z. C. Yu, J. W. Tang, M. L. Cai, Y. L. Chen, C. W. Yang, W.S. Chow, and C. L. Peng. The major photoprotective role of anthocyanins in leaves of arabidopsis thaliana under long-term high light treatment: antioxidant or light attenuator? *Photosynthesis Research*, pages 1–16, 2020.

[6] S. Lev-Yadun and K. S. Gould. Role of anthocyanins in plant defence. pages 22–28, 2008.

[7] E. Pojer, F. Mattivi, D. Johnson, and C. S. Stockley. The case for anthocyanin consumption to promote human health: a review. *Comprehensive Reviews in Food Science and Food Safety*, 12(5):483–508, 2013.

[8] H. E. Khoo, A. Azlan, S. T. Tang, and S. M. Lim. Anthocyanidins and anthocyanins: colored pigments as food, pharmaceutical ingredients, and the potential health benefits. *Food & nutrition research*, 61(1):1361779, 2017.

[9] B. S. Sivamaruthi, P. Kesika, K. Subasankari, and C. Chaiyasut. Beneficial effects of anthocyanins against diabetes mellitus associated consequences-a mini review. *Asian Pacific Journal of Tropical Biomedicine*, 8(10):471, 2018.

[10] A. C. Gonçalves, A. R. Nunes, A. Falcão, G. Alves, and L. R. Silva. Dietary effects of anthocyanins in human health: A comprehensive review. *Pharmaceuticals*, 14(7):690, 2021.

[11] K. Noi, K. Ikenaka, H. Mochizuki, Y. Goto, and H. Ogi. Disaggregation behavior of amyloid β fibrils by anthocyanins studied by total-internal-reflection-fluorescence microscopy coupled with a wireless quartz-crystal microbalance biosensor. *Analytical Chemistry*, 93(32):11176–11183, 2021.

[12] S. G. Lambert, R. E. Asenstorfer, N. M. Williamson, P. G. Iland, and G. P. Jones. Copigmentation between malvidin-3-glucoside and some wine constituents and its importance to colour expression in red wine. *Food Chemistry*, 125(1):106–115, 2011.

[13] I. Iglesias, G. Echeverria, and Y. Soria. Differences in fruit colour development, anthocyanin content, fruit quality and consumer acceptability of eight 'gala'apple strains. *Scientia Horticulturae*, 119(1):32–40, 2008.

[14] J. A. Stavang, S. Freitag, A. Foito, S. Verrall, O. M. Heide, D. Stewart, and A. Sønsteby. Raspberry fruit quality changes during ripening and storage as assessed by colour, sensory evaluation and chemical analyses. *Scientia Horticulturae*, 195:216–225, 2015.

[15] X. Zheng, C. Yue, K. Gallardo, V., J. Luby, and J. McFerson. What attributes are consumers looking for in sweet cherries? evidence from choice experiments. *Agricultural and Resource Economics Review*, 45(1):124–142, 2016.

[16] M. Grätzel. Dye-sensitized solar cells. *Journal of photochemistry and photobiology C: Photochemistry Reviews*, 4(2):145–153, 2003.

[17] F. Pina, J. Oliveira, and V. de Freitas. Anthocyanins and derivatives are more than flavylium cations. *Tetrahedron*, 71(20):3107–3114, 2015.

[18] Y. Leydet, R. Gavara, V. Petrov, A. M. Diniz, A. J. Parola, J. C. Lima, and F. Pina. The effect of self-aggregation on the determination of the kinetic and thermodynamic constants of the network of chemical reactions in 3-glucoside anthocyanins. *Phytochemistry*, 83:125–135, 2012.

[19] E. S. Sadlowski. Ph-dependent anthocyanin reactions in micellar and copigmented solutions. 1987.

[20] T. Hoshino, U. Matsumoto, and T. Goto. Self-association of some anthocyanins in neutral aqueous solution. *Phytochemistry*, 20(8):1971–1976, 1981.

[21] S. González-Manzano, C. Santos-Buelga, M. Duenas, J. C. Rivas-Gonzalo, and T. Escribano-Bailon. Colour implications of self-association processes of wine anthocyanins. *European Food Research and Technology*, 226(3):483–490, 2008.

[22] A. Padayachee, G. Netzel, M. Netzel, L. Day, D. Zabaras, D. Mikkelsen, and M. J. Gidley. Binding of polyphenols to plant cell wall analogues–part 1: Anthocyanins. *Food Chemistry*, 134(1):155–161, 2012.

[23] J. Mendoza, J. Oliveira, P. Araújo, N. Basílio, N. Teixeira, N. F. Brás, and V. de Freitas. The peculiarity of malvidin 3-o-(6-op-coumaroyl) glucoside aggregation. intra and intermolecular interactions. *Dyes and Pigments*, 180:108382, 2020.

[24] F. C. Spano. The spectral signatures of Frenkel polarons in H-and J-aggregates. *Accounts of chemical research*, 43(3):429–439, 2010.

[25] M. Yamagishi. How genes paint lily flowers: regulation of colouration and pigmentation patterning. *Scientia Horticulturae*, 163:27–36, 2013.

[26] C. C. Hsu, Y. Y. Chen, W. C. Tsai, W. H. Chen, and H. H. Chen. Three r2r3-myb transcription factors regulate distinct floral pigmentation patterning in phalaenopsis spp. *Plant Physiology*, 168(1):175–191, 2015.

[27] R. Medel, C. Botto-Mahan, and M. Kalin-Arroyo. Pollinator-mediated selection on the nectar guide phenotype in the andean monkey flower, mimulus luteus. *Ecology*, 84(7):1721–1732, 2003.

[28] Z. X. Ren, D. Z. Li, P. Bernhardt, and H. Wang. Flowers of cypripedium fargesii (orchidaceae) fool flat-footed flies (platypezidae) by faking fungus-infected foliage. *Proceedings of the National Academy of Sciences*, 108(18):7478–7480, 2011.

[29] M. L. de Jager, E. Willis-Jones, S. Critchley, and B. J. Glover. The impact of floral spot and ring markings on pollinator foraging dynamics. *Evolutionary ecology*, 31(2):193–204, 2017.

[30] O. Skaliter, Y. Kitsberg, E. Sharon, E. Shklarman, E. Shor, T. Masci, A. Vainstein, et al. Spatial patterning of scent in petunia corolla is discriminated by bees and involves the abcg1 transporter. *The Plant Journal*, 2021.

[31] B. Ding, E. L. Patterson, S. V.Holalu, J. Li, G. A. Johnson, L. E. Stanley, and Y. W. Yuan. Two MYB proteins in a self-organizing activator-inhibitor system produce spotted pigmentation patterns. *Current Biology*, 30(5):802–814, 2020.

[32] N. Ercolani, R. Indik, A. C. Newell, and T. Passot. The geometry of the phase diffusion equation. *J. Nonlinear Science*, 10:223–274, 2000.

[33] P. F. Moreira, L. Giestas, C. Yihwa, C. Vautier-Giongo, F. H. Quina, A. L. Maçanita, and J. C. Lima. Ground-and excited-state proton transfer in anthocyanins: From weak acids to superphotoacids. *The Journal of Physical Chemistry A*, 107(21):4203–4210, 2003.

[34] T. Hoshino. Self-association of flavylium cations of anthocyanidin 3, 5-diglucosides studied by circular dichroism and 1h nmr. *Phytochemistry*, 31(2):647–653, 1992.

[35] K. Murakami. Thermodynamic and kinetic aspects of self-association of dyes in aqueous solution. *Dyes and Pigments*, 53(1):31–43, 2002.

[36] A. M. Turing. The chemical basis of morphogenesis. *Bulletin of mathematical biology*, 52(1):153–197, 1990.

[37] D. A. Young. A local activator-inhibitor model of vertebrate skin patterns. *Mathematical Biosciences*, 72(1):51–58, 1984.

[38] R. Hoyle. *Pattern Formation: An Introduction to Methods*. Cambridge UP, 2006.

[39] Y. Song, R. Yang, and G. Sun. Pattern dynamics in a Gierer–Meinhardt model with a saturating term. *Applied Mathematical Modelling*, 46:476–491, 2017.

[40] R. A. Veitia. A sigmoidal transcriptional response: cooperativity, synergy and dosage effects. *Biological Reviews*, 78(1):149–170, 2003.

[41] A. Gierer and H. Meinhardt. A theory of biological pattern formation. *Kybernetik*, 12(1):30–39, 1972.

[42] H. Meinhardt. Turing's theory of morphogenesis of 1952 and the subsequent discovery of the crucial role of local self-enhancement and long-range inhibition. *Interface Focus*, 2(4):407–416, 2012.

[43] H. Meinhardt and A. Gierer. Pattern formation by local self-activation and lateral inhibition. *Bioessays*, 22(8):753–760, 2000.

[44] S. M. Cox and P. C. Matthews. Exponential time differencing for stiff systems. *Journal of Computational Physics*, 176(2):430–455, 2002.

[45] R. V. Craster and R. Sassi. Report no. 99. Technical report, Universitá degli Studi di Milano, 2006.

[46] Q. Zheng, Z. Wang, J. Shen, and H. M. A. Iqbal. Turing bifurcation and pattern formation of stochastic reaction-diffusion system. *Advances in Mathematical Physics*, 2017, 2017.

[47] P. D. Weidman M. I. Rabinovich, A. B. Ezersky. *The Dynamics of Patterns*. World Scientific, 2000.

[48] M. Cross and H. Greenside. *Pattern Formation and Dynamics in Nonequilibrium Systems*. Cambridge UP, 2009.

[49] Q. Ouyang, G. H. Gunaratne, and H. L. Swinney. Rhombic patterns: Broken hexagonal symmetry. *Chaos: An Interdisciplinary Journal of Nonlinear Science*, 3(4):707–711, 1993.

[50] A. V. Getling. *Rayleigh-Bénard convection: structures and dynamics*, volume 11. World Scientific, 1998.

[51] R. M. Bradley and P.D. Shipman. Spontaneous pattern formation induced by ion bombardment of binary compounds. *Phys. Rev. Lett.*, 105(14):145501, 2010.

[52] R. M. Bradley and P.D. Shipman. A surface layer of altered composition can play a key role in nanoscale pattern formation induced by ion bombardment. *Appl. Surf. Sci.*, 258(9):4161–4170, 2012.

[53] P.D. Shipman and R. M. Bradley. Theory of nanoscale pattern formation induced by normal-incidence ion bombardment of binary compounds. *Phys. Rev. B*, 84(8):085420, 2011.

[54] C. Gollwitzer, I. Rehberg, and R. Richter. Via hexagons to squares in ferrofluids: experiments on hysteretic surface transformations under variation of the normal magnetic field. *Journal of Physics: Condensed Matter*, 18(38):S2643, 2006.

[55] D. Walgraef. *Spatio-Temporal Pattern Formation*. Springer, 1997.

[56] Y. Sun, H. Li, and J. R. Huang. Arabidopsis tt19 functions as a carrier to transport anthocyanin from the cytosol to tonoplasts. *Molecular Plant*, 5(2):387–400, 2012.

[57] R. F. Kratz. *Biology for dummies*. John Wiley & Sons, 2017.

[58] H. Kim, A. Yun, S. Yoon, C. Lee, J. Park, and J. Kim. Pattern formation in reaction–diffusion systems on evolving surfaces. *Computers & Mathematics with Applications*, 80(9):2019–2028, 2020.

[59] L. Gu, P. Gong, and H. Wang. Hopf bifurcation and turing instability analysis for the gierer–meinhardt model of the depletion type. *Discrete Dynamics in Nature and Society*, 2020, 2020.

[60] H. A. van Doren, E. Smits, J. M. Pestman, J. B. Engberts, and R. M. Kellogg. Mesogenic sugars. from aldoses to liquid crystals and surfactants. *Chemical Society Reviews*, 29(3):183–199, 2000.

[61] V. R. Horowitz, L. A. Janowitz, A. L. Modic, P. A. Heiney, and P. J. Collings. Aggregation behavior and chromonic liquid crystal properties of an anionic monoazo dye. *Physical Review E*, 72(4):041710, 2005.

[62] Z. S. Davidson, Y. Huang, A. Gross, A. Martinez, T. Still, C. Zhou, and A. G. Yodh. Deposition and drying dynamics of liquid crystal droplets. *Nature Communications*, 8(1):1–7, 2017.

[63] T. D. Potter, M. Walker, and M. R. Wilson. Self-assembly and mesophase formation in a non-ionic chromonic liquid crystal: Insights from bottom-up and top-down coarse-grained simulation models. *Soft Matter*, 16(41):9488–9498, 2020.

[64] E. J. De Souza, L. Gao, T. J. McCarthy, E. Arzt, and A. J. Crosby. Effect of contact angle hysteresis on the measurement of capillary forces. *Langmuir*, 24(4):1391–1396, 2008.

[65] H. Ren, S. Xu, and S. T. Wu. Effects of gravity on the shape of liquid droplets. *Optics Communications*, 283(17):3255–3258, 2010.

[66] S. J. Kang, V. Vandadi, J. D. Felske, and H. Masoud. Alternative mechanism for coffee-ring deposition based on active role of free surface. *Physical Review E*, 94(6):063104, 2016.

[67] A. Kushner, V. Lychagin, and V. Rubtsov. *Contact Geometry and Nonlinear Differential Equations*. Cambridge UP, 2006.

[68] C. Delaunay. Sur la surface de révolution dont la courbure moyenne est constante. *J. Math. pures et appl. Sér*, 1:309–320, 1841.

[69] J. Eells. The surfaces of Delaunay. *The Mathematical Intelligencer*, 9:53–57, 1987.

[70] M. Hadzhilazova, I. M. Mladenov, and J. Oprea. Unduloids and their geometry. *Archivum Mathematicum*, 043:417–429, 2007.

[71] B. A. Shipman, P. D. Shipman, and D. Packard. Generalized Weierstrass–Enneper representations of Euclidean, spacelike, and timelike surfaces: a unified Lie-algebraic formulation. *Journal of Geometry*, 108(2):545–563, 2017.

[72] U. Abresch. Constant mean curvature tori in terms of elliptic functions. *Journal für die reine und angewandte Mathematik (Crelles Journal)*, 374:169–192, 1987.

[73] R. Walter. Explicit examples to the H-problem of Heinz Hopf. *Geometriae Dedicata*, 25:187–213, 1987.

[74] A. I. Bobenko and U. Eitner. Bonnet surfaces and Painlevé equations. *Journal fuer die reine und angewandte Mathematik (J. reine angew. Math.)*, 499:47–79, 1998.

[75] A. I. Bobenko and U. Eitner. *Bonnet surfaces and Painlevé equations*. Walter de Gruyter GmbH and Co. KG Berlin, Germany, 1998.

[76] M. Allmaras, W. Bangerth, J. M. Linhart, J. Polanco, F. Wang, K. Wang, and S. Zedler. Estimating parameters in physical models through Bayesian inversion: A complete example. *SIAM Review*, 55(1):149–167, 2013.

[77] F. C. Spano and C. Silva. H-and J-aggregate behavior in polymeric semiconductors. *Annual Review of Physical Chemistry*, 65:477–500, 2014.